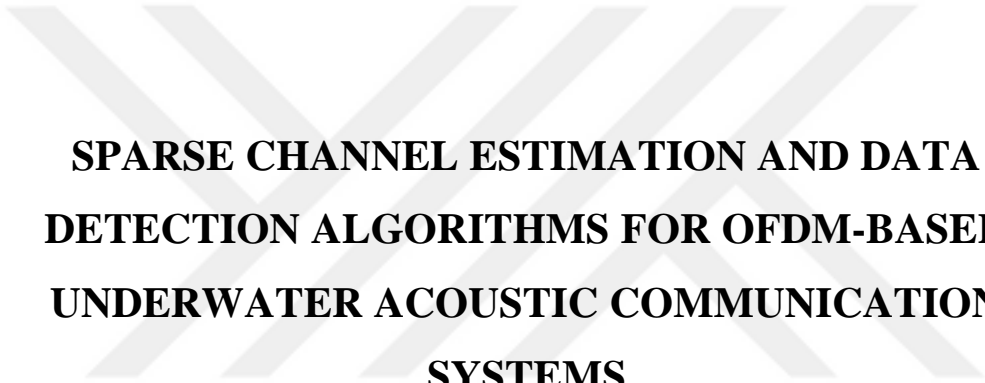


KADİR HAS UNIVERSITY  
GRADUATE SCHOOL OF SCIENCE AND ENGINEERING  
PROGRAM OF PhD IN ELECTRONICS ENGINEERING



**SPARSE CHANNEL ESTIMATION AND DATA  
DETECTION ALGORITHMS FOR OFDM-BASED  
UNDERWATER ACOUSTIC COMMUNICATION  
SYSTEMS**

Mhd Tahssin ALTABBAA

DOCTOR of PHILOSOPHY THESIS

İSTANBUL, November 2018

Mhd Tahsin ALTABBAA

Ph.D. Thesis

2018





**SPARSE CHANNEL ESTIMATION AND DATA  
DETECTION ALGORITHMS FOR OFDM-BASED  
UNDERWATER ACOUSTIC COMMUNICATION  
SYSTEMS**

Mhd Tahssin ALTABBAA

DOCTOR of PHILOSOPHY THESIS

Submitted to the Graduate School of Science and Engineering of Kadir Has University  
in partial fulfillment of the requirements for the degree of Doctorate's in the Program of  
Electronics Engineering

İSTANBUL, November, 2018

DECLARATION OF RESEARCH ETHICS /  
METHODS OF DISSEMINATION

I, Mhd Tahssin ALTABBAA, hereby declare that;

- this Doctorate's Thesis is my own original work and that due references have been appropriately provided on all supporting literature and resources;
- this Doctorate's Thesis contains no material that has been submitted or accepted for a degree or diploma in any other educational institution;
- I have followed "Kadir Has University Academic Ethics Principles" prepared in accordance with the "The Council of Higher Education's Ethical Conduct Principles"

In addition, I understand that any false claim in respect of this work will result in disciplinary action in accordance with University regulations.

Furthermore, both printed and electronic copies of my work will be kept in Kadir Has Information Center under the following condition as indicated below:

- The full content of my thesis/project will be accessible from everywhere by all means.

Mhd Tahssin ALTABBAA



---

9/11/2018

KADIR HAS UNIVERSITY  
GRADUATE SCHOOL OF SCIENCE AND ENGINEERING

**ACCEPTANCE AND APPROVAL**

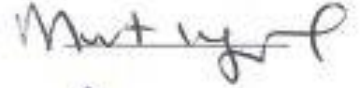
This work entitled **SPARSE CHANNEL ESTIMATION AND DATA DETECTION ALGORITHMS FOR OFDM-BASED UNDERWATER ACOUSTIC COMMUNICATION SYSTEMS** prepared by **Mhd Tahssin ALTABBAA** has been judged to be successful at the defense exam held on **09/11/2018** and accepted by our jury as **DOCTORATE'S THESIS**.

APPROVED BY:

(Prof. Dr. Erdal Panayırıcı) (Advisor) (Kadir Has University)



(Prof. Dr. Murat Uysal) (Özyeğin University)



(Prof. Dr. Ayşe Hümevra Bilge) (Kadir Has University)



(Assoc. Prof. Ertuğrul Başar) (Koç University)



(Asst. Prof. Selçuk Öğrenci) (Kadir Has University)



I certify that the above signatures belong to the faculty members named above.

(Assoc. Prof. Dr. Ebru Demet AKDOĞAN)

Dean of Graduate School of Science and Engineering

DATE OF APPROVAL: (9/11/2018)

## TABLE OF CONTENTS

<b>TABLE OF CONTENTS</b> .....	<b>7</b>
<b>ABSTRACT</b> .....	<b>i</b>
<b>ÖZET</b> .....	<b>iii</b>
<b>ACKNOWLEDGMENTS</b> .....	<b>v</b>
<b>LIST OF TABLES</b> .....	<b>vi</b>
<b>LIST OF FIGURES</b> .....	<b>vii</b>
<b>LIST OF ABBREVIATIONS</b> .....	<b>ix</b>
<b>1. INTRODUCTION</b> .....	<b>1</b>
1.1 Motivation .....	1
1.2 State-of-the-art on Channel Estimation Algorithms.....	1
1.3 Contribution of This Work .....	5
<b>2. STATE-OF-THE-ART ON UNDERWATER ACOUSTIC COMMUNICATIONS</b> .....	<b>7</b>
2.1 History of Underwater Acoustical Communications .....	7
2.2 Why Acoustic Signals .....	7
2.3 Characteristics of Underwater Acoustic Channel.....	8
2.3.1 Sound Velocity .....	9
2.3.2 Propagation Loss .....	9
2.3.2.1 Absorptive Loss .....	10
2.3.2.2 Scattering Loss .....	11
2.3.3 Ambient Noise and Interference .....	12
2.3.4 Large Doppler Shift.....	14
2.3.5 Long propagation Delay .....	15
2.3.6 Multipath Propagation and Channel Models.....	15
2.4 Bellhop Acoustic Toolbox.....	18
2.4.1 Overview .....	18
2.4.2 Environmental Profile .....	19
2.4.3 Sound speed profile .....	20

<b>3. SPARSE CHANNEL ESTIMATION AND DATA DETECTION FOR OFDM-BASED UNDERWATER ACOUSTIC SYSTEMS IN RICIAN FADING .....</b>	<b>21</b>
3.1 Introduction .....	21
3.2 System and Channel Model.....	22
3.3 Sparse Multipath Channel Estimation .....	29
3.3.1 Preprocessing .....	29
3.3.2 Path Delays and Doppler Spread Estimation .....	30
3.3.3 Path Gains Estimation $h\ell$ .....	31
3.3.4 ML Estimation of the Prior Unknown Mean and Variance $\mu\ell, s\ell\ell L - 1$ .....	34
3.4 Equalization and data Detection .....	37
3.5 Computation Complexity .....	38
3.6 Computer Simulations with BELLHOP Simulated Channels in Sapanca Lake ...	40
3.7 OMP-MAP Estimation .....	48
3.7.1 OMP-MAP Algorithm.....	49
3.7.2 Simulation Results for UWA Channel undergoing <i>Rician</i> Fading with different non-uniform Doppler rates .....	51
3.7.3 Simulation Results for UWA Channel undergoing <i>log-normal</i> and <i>Nakagami-m</i> Fading with different non-uniform Doppler rates .....	56
3.7.4 Conclusion.....	60
<b>4. SPARSE CHANNEL ESTIMATION FOR SPACE-TIME BLOCK CODED OFDM-BASED UNDERWATER ACOUSTIC CHANNELS .....</b>	<b>61</b>
4.1 Introduction .....	61
4.2 Alamouti's Transmit Diversity Scheme For OFDM Systems.....	63
4.3 Representation of The Discrete UWA Channel .....	64
4.4 EM-Based Map Sparse Channel Estimation .....	66
4.4.1 initialization.....	68
4.4.2 Computation of $\Gamma\mu q$ for QPSK Signalling .....	70
4.4.3 Final Sparse Channel Estimation .....	70
4.5 Simulation Results.....	72
4.6 Conclusion .....	76
<b>5. CONCLUSIONS .....</b>	<b>77</b>







SPARSE CHANNEL ESTIMATION AND DATA DETECTION ALGORITHMS  
FOR OFDM-BASED UNDERWATER ACOUSTIC COMMUNICATION SYSTEMS

**ABSTRACT**

Communication over acoustic signals in underwater results into a multi-scale multi-lag channels, which occurs due to the multipath propagation. Hence, a robust channel estimation technique has to be present at the receiver, and the solutions of the terrestrial-based systems are not applicable. In this work, using path-based channel model that characterizes underwater channels by a delay, a Doppler shift, and an attenuation factors, three new pilot assisted, time domain-based channel estimation algorithms are proposed for single-input single-output communication-based and diversity communication-based underwater acoustic systems. The multicarrier transmission technique assumed is OFDM. In addition, depending on the base stations deployment in underwater, the sparse underwater channels undergo Rician or Rayleigh fading, where channels in this work are generated using Bellhop software. In the first two proposed approach, the overall sparse channel tap delays and constant Doppler shifts are estimated using Matching Pursuit and Orthogonal Matching Pursuit algorithms, where the sparse complex channel path gain vector is estimated by maximum *a posteriori* probability (MAP) technique, and the prior densities of the channel gains follow Rician distribution with unknown mean and variance vectors, where Maximum Likelihood is proposed for their estimation. The first approach considers a colored noise and uniform Doppler spread, and the second approach considers a non-uniform Doppler shifts with white noise. The third proposed approach considers transmitter diversity with Alamouti's coding, where the channel estimator iteratively estimates the complex channel parameters of each subcarrier using the expectation maximization method, which in turn converges to a true maximum *a posteriori* probability estimation of the unknown channel, where Karhunen-Loeve expansion and ESPRIT algorithm are assumed for complexity reduction and delay estimation, respectively. Finally, in

**order to assess the performance of the proposed algorithms, the computer simulations show the behavior in terms of mean square error and symbol error rate.**

**Keywords:** Channel estimation, detection, equalization, underwater acoustic communication, Alamouti coding, space-time coding, expectation maximization algorithm, maximum a posteriori channel estimation.



# DFBÇ TABANLI SUALTI AKUSTİK HABERLEŞME SİSTEMLERİ İÇİN SEYREK KANAL KESTİRİMİ VE VERİ TESPİT ALGORİTMALARI

## ÖZET

Sualtıdaki akustik sinyallerle haberleşme çokyollu yayılımdan dolayı çok ölçekli çok gecikmeli kanallara yol açmaktadır. Bu nedenle, kara tabanlı çözümler uygulanamamakta ve alıcı tarafında kuvvetli kanal kestirim teknikleri sunulmalıdır. Bu çalışmada, tek girişli tek çıkışlı haberleşme tabanlı ve çeşitli haberleşme tabanlı sualtı akustik sistemleri için sualtı kanallarını gecikme, Doppler kayması ve sönmüleme unsuru ile karakterize eden yol tabanlı kanal modeli kullanılarak iki yeni kılavuz yardımcılı, zaman bölgesi tabanlı kanal kestirim algoritmaları önerilmiştir. Çok-taşıyıcılı verici tekniği olarak dikey frekans bölmeli çoklama (DFBÇ) kabul edilmiştir. Ek olarak, baz istasyonlarının konuşlanmalarına bağlı olarak, seyrek sualtı kanalları Rician veya Rayleigh sönmülemesine uğramaktadır ve her ikisi de bu çalışmada göz önünde bulundurulmuştur ve Bellhop yazılımı bunların üretimi için kullanılmıştır. İlk önerilen yaklaşımda, seyrek karmaşık kanal yol kazanç vektörünün maksimum sonsal olasılık (MSO) tekniğiyle kestirildiği durumda, kanal kazancının öncelikli yoğunluğunun bilinmeyen ortalama gradiyent ve varyans vektörlerine sahip Rician dağılımı takip ettiği ve bunların kestirimi için enbüyük olabilirlik (EO) tekniğinin önerildiği durumda genel seyrek kanal çıkma gecikmeleri ve sabit Doppler kaymaları Matching Pursuit (MP) algoritması kullanılarak kestirilmiştir. İlk yaklaşıma bir genişletme yapılmış, algoritmada düzensiz Doppler kayması değerlendirilmiş ve Orthogonal Matching Pursuit (OMP) kullanılmıştır. İkinci önerilen yaklaşımda ise Alamouti kodlamasıyla verici çeşitliliği değerlendirilmiş, kanal kestirici tekrarlı olarak her bir alt taşıyıcının karmaşık kanal parametrelerini beklenti maksimizasyonu (BM) metoduyla kestirmekte olup, bilinmeyen kanalın kestirimi doğru maksimum sonsal olasılık (MSO) kestirimine yakınsamış, ve karmaşıklık azaltmak ve gecikme hesabı için sırasıyla Karhunen-Loeve genişletmesi

ve ESPRIT algoritması kabul edilmiştir. Son olarak, önerilmiş algoritmanın performansını değerlendirmek için bilgisayar benzetimleriyle sistem davranışı ortalama karesel hata (OKH) ve işaret hata oranı (İHO) cinsinden gösterilmiştir.

**Anahtar Sözcükler:** Kanal kestirimi, belirleme, eşitleme, sualtı akustik haberleşme, Alamouti kodlama, uzay-zaman kodlama, beklenti maksimizasyonu algoritması, maksimum sonsal olasılık kestirimi



## ACKNOWLEDGMENTS

Praises and thankfulness to Allah, the most merciful and most compassionate for the great bounties bestowed upon me and granting me the strength to seek knowledge. A PhD thesis is a singularly authored document, but not one that is written in isolation. I would like to start with expressing my sincere gratitude to my thesis advisor Prof. Dr. Erdal PANAYIRCI for his beneficial advices, incessant encouragement, enduring patience, and constant support. I am indebted to Prof. PANAYIRCI for providing me with clear explanations and always giving me his time. It was a great honor for me to serve as a teaching and research assistant during my doctorate studies at Kadir Has University. However, I would like to show my appreciation to the members of the school of science and engineering faculty, notably, my admiration for Assoc. Prof. Serhat ERKÜÇÜK and Assoc. Prof. Metin ŞENGÜL for their encouragements along my PhD studies. In addition, I would like to thank Asst. Prof. Atilla ÖZMEN and Asst. Prof. Selçuk ÖĞRENCİ for their kindness and friendliness when I was attending their courses as an assistant in the lab. I would like to thank Asst. Prof. Bahattin KARAKAYA from Istanbul University, for his guidance and help in setting up Bellhop software. I also would like to show my appreciation to my colleagues at Kadir Has University and say “good luck to all of you. Working with you guys was an advantageous for me and full of fun”. Last but not the least, I would like to show my appreciation to my family, my mother, my sisters and their lovely families.

This work would not have been possible without support from the Suasis as a sub-contract of the Turkish Scientific and Research Council (TUBITAK) under Grant 1140029, and in part by the U.S. National Science Foundation under Grant CCF-1420575, and in part by KAUST under grant No. OSR-2016-CRG 5-2958-02.

## LIST OF TABLES

Table 2.1 Comparison of acoustic, EM and optical waves in underwater medium.....	8
Table 3.1 Computational complexity details .....	39
Table 3.2 Channel and simulation parameters for Sapanca Lake .....	44





## LIST OF FIGURES

Figure 2.1 Illustration of the overall AQUO methodology.....	13
Figure 2.2 Short-range propagation. ....	16
Figure 2.3 Long-range propagation.....	16
Figure 3.1 Block diagram of the MP-MAP channel estimation and equalization algorithm. ....	38
Figure 3.2 Source and destination stations in Sapanca Lake .....	40
Figure 3.3 Ray tracing for a range of 5km .....	41
Figure 3.4 Sound speed profile for Sapanca Lake .....	42
Figure 3.5 CIR for a range of 5km. (a) Original CIR with 607 paths; (b) Clustered paths with 79 clusters; (c) $L = 3$ , delay spread = 28.5383 ms (normalized); (d) $L = 5$ , delay spread = 28.5383 ms (normalized).....	43
Figure 3.6 MSE vs. SNR performance comparisons of the MP-MAP and MP algorithms for different constellations: $q = 8, b_{max} = 10 - 3, \Delta p = 4$ . ....	45
Figure 3.7 SER vs. SNR performance comparisons of the MP-MAP and MP algorithms for different constellations: $q = 8, b_{max} = 10 - 3, \Delta p = 4$ . ....	45
Figure 3.8 MSE vs. SNR performance of the MP-MAP algorithm for different resolution factors: $b_{max} = 10 - 3, \Delta p = 4$ , 16QAM signaling.....	46
Figure 3.9 SER vs. SNR performance of the MP-MAP algorithm for different resolution factors: $b_{max} = 10 - 3, \Delta p = 4$ , 16QAM signaling.....	46
Figure 3.10 MSE vs. SNR performance of the MP-MAP algorithm for different Doppler rates: $q = 8, \Delta p = 4$ , 16QAM signaling. ....	47
Figure 3.11 SER vs. SNR performance of the MP-MAP algorithm for different Doppler rates: $q = 8, \Delta p = 4$ , 16QAM signaling.....	47
Figure 3.12 MSE vs. SNR performance of the MP-MAP algorithm for different pilot spacings: $q = 16, b_{max} = 10 - 3$ , 16QAM signaling.....	48
Figure 3.13 SER vs. SNR performance of the MP-MAP algorithm for different pilot spacings: $q = 16, b_{max} = 10 - 3$ , 16QAM signaling.....	48
Figure 3.14 Block diagram of the OMP-MAP channel estimation and equalization algorithm .....	49
Figure 3.15 MSE vs. SNR performance comparisons of the OMP-MAP and OMP algorithms for different constellations: $q = 4, b_{max} = 10 - 4, \Delta p = 4$ . ....	51
Figure 3.16 SER vs. SNR performance comparisons of the OMP-MAP and OMP algorithms for different constellations: $q = 4, b_{max} = 10 - 4, \Delta p = 4$ . ....	52
Figure 3.17 MSE vs. SNR performances of the OMP-MAP and OMP algorithms for different resolution factors: $b_{max} = 10 - 3, \Delta p = 4$ , 16QAM signaling.....	53
Figure 3.18 SER vs. SNR performances of the OMP-MAP and OMP algorithms for different resolution factors: $b_{max} = 10 - 3, \Delta p = 4$ , 16QAM signaling.....	53
Figure 3.19 MSE vs. Doppler rate performances of the OMP-MAP and OMP algorithms for different Doppler rates: $q = 8, \Delta p = 4$ , 16QAM signaling. ....	54
Figure 3.20 SER vs. Doppler rate performances of the OMP-MAP and OMP algorithms for different Doppler rates: $q = 8, \Delta p = 4$ , 16QAM signaling. ....	54
Figure 3.21 SER vs. SNR performance of the OMP-MAP algorithm for different pilot spacings: $q = 4, b_{max} = 10 - 4$ , 16QAM signaling. ....	55
Figure 3.22 MSE vs. SNR performances of the OMP-MAP, OMP and FISTA algorithms with QPSK signaling, $q = 4, b_{max} = 10 - 4, \Delta p = 4$ . ....	56

Figure 3.23 SER vs. SNR performances of the OMP-MAP, OMP and FISTA algorithms with QPSK signaling, $\rho = 4$ , $b_{max} = 10^{-4}$ , $\Delta p = 4$ . .....	56
Figure 3.24 MSE vs. SNR comparisons of the OMP-MAP and OMP algorithms for different fading models with QPSK signaling, $\rho = 4$ , $b_{max} = 10^{-4}$ , $\Delta p = 4$ (random case channel). .....	59
Figure 3.25 SER vs. SNR comparisons of the OMP-MAP and OMP algorithms for different fading models with QPSK signaling, $\rho = 4$ , $b_{max} = 10^{-4}$ , $\Delta p = 4$ (random case channel). .....	59
Figure 4.1 MSE vs. SNR performance of the MAP-EM-ESPRIT algorithm for different residual Doppler rates $b = [10^{-3}, 5 \times 10^{-3}, 10^{-3}]$ with $\Delta sc = 4$ . .....	73
Figure 4.2 SER vs. SNR performance of the MAP-EM-ESPRIT algorithm for different residual Doppler rates $b = [10^{-3}, 5 \times 10^{-3}, 10^{-3}]$ with $\Delta sc = 4$ . .....	74
Figure 4.3 MSE vs. SNR performance of the MAP-EM-ESPRIT algorithm for different pilot spacings $\Delta sc = [2, 4, 8]$ , with $b = 10^{-3}$ Hz. .....	75
Figure 4.4 SER vs. SNR performance of the MAP-EM-ESPRIT algorithm for different pilot spacings $\Delta sc = [2, 4, 8]$ , with $b = 10^{-3}$ Hz. .....	75

## LIST OF ABBREVIATIONS

<b>Acronym</b>	<b>Definition</b>
AOA	Angle of Arrival
A/D	Analog-to-Digital
BER	Bit Error Rate
BP	Basic Pursuit
CE	Channel Estimation
CFO	Carrier Frequency Offset
CIR	Channel Impulse Response
CP	Cyclic Prefix
CSI	Channel State Information
CAs	Complex Additions
CMs	Complex Multiplications
DFT	Direct Fourier Transform
EM	Electromagnetic
ESPRIT	Estimation of Signal Parameters via Rotational Invariance Techniques
FFT	Fast Fourier Transform
FISTA	Fast Iterative Shrinkage-Thresholding Algorithm
ICI	Intercarrier Interference
ISI	Intersymbol Interference
IDFT	Inverse Direct Fourier Transform
IFFT	Inverse Fast Fourier Transform
ISI	Intersymbol Interference
LMMSE	Linear Minimum Mean Square Error
LMS	Least-Mean-Squares
LR	Linear Regression
LS	Least-Squares
LOS	Line of Sight
MAP	Maximum a posteriori
MIMO	Multiple Input Multiple Output
MISO	Multiple Input Single Output
ML	Maximum Likelihood
MP	Matching Pursuit
MSE	Mean Square Error

OFDM	Orthogonal Frequency Division Multiplexing
OMP	Othrogonal Matching Pursuit
PDF	Probability Density Function
PSK	Phase-Shift Keying
QAM	Quadrature Amplitude Modulation
QPSK	Quadrature Phase Shift-Keying
RF	Radiofrequency
RLS	Recursive Least-Squares
SAGE	Space Alternating Generalized Expectation-maximization
SER	Symbol Error Rate
SFBC	Space-Frequency Block Coded
SISO	Single Input Single Output
SNR	Signal to Noise Ratio
SSP	Sound Speed Profile
SPM	Statistical Prediction Model
SVD	Singular Value Decomposition
UASP	Underwater Acoustic Signal processing
UHF	Ultra High Frequency
UWAC	Underwater Acoustic Communications
Virtex	Virtual Timeseries EXperiment

# 1. INTRODUCTION

## 1.1 Motivation

The surface of the earth planet is covered by more than two thirds of water including oceans, seas, rivers and lakes, where the need of having a robust communication system in the underwater environment is essential. Various applications for several domains that operate in aquatic environments require a wireless communication link for reporting and data exchange. Research laboratories and governments tend to develop this type of wireless communication in order to meet different applications such as submarine communication, seismic (tsunami) detectors, offshore oil field exploration and monitoring, intrusion detection for tactical surveillance (port and border security), maritime archaeology, data collection, environmental (pollution) monitoring and various of military applications that even wireless sensor networks found their way to such environment (Liu et al., 2008) (Chen et al., 2014.) (Zhang, et al., 2014) (Bernard and Meinig, 2011) (Mandalapa et al., 2016). The channel estimator design at the receiver side is a challenging problem in underwater due to the impairments that the signals face in such medium, which the overall system performance depends on it. The performance of an acoustical communication system in underwater depends on estimating different parameters regarding the communication channel, where the characteristics of the channel in this medium affect the channel impulse response.

## 1.2 State-of-the-art on Channel Estimation Algorithms

Different approaches are well-studied for a robust channel estimation. Space-time coding and multi-input multi-output (MIMO) configurations as well as orthogonal frequency division multiplexing (OFDM)-based communication systems, which were originally introduced in the context of terrestrial radiofrequency (RF) wireless communication, have been successfully applied to underwater communications in recent studies (Pelekanakis

and Baggeroer, 2011) (Li, et al., 2009). These techniques seem to be primary candidates for next generation UWA systems, due to their high information capacity and robustness to large multipath spreads (Tu, et al., 2011) (Emre et al., 2008) and bring significant improvements in both throughput rate and error rate performance. On the other hand, when the deployment of multi transmit/receive elements is not possible due to space or power limitations and pathloss becomes a performance limiting factor, relay-assisted (cooperative) communication has also been applied to UWA systems to take advantage of diversity benefits. These works have been mostly focused on capacity and power allocation (Choudhuri and Mitra, 2009) for UWA relay channels with intersymbol interference (ISI), distributed channel coding and space time cooperative schemes for UWA channels (Vajapeyam et al., 2008) (Jalil and Ghrayeb, 2014), and on channel estimation and equalization for amplify-and-forward cooperative relay based OFDM systems in UWA channels (Panayirci et al., 2016). Notably, in (Panayirci et al., 2016), Rayleigh fading channels between source, relay and destination, an efficient algorithm is developed based on the space-alternating generalized expectation-maximization (SAGE) technique for the latter purpose.

The fundamental performance bounds of such systems are determined by the inherent characteristics of the underwater channel and by reliable channel state information (CSI) available at the destination, to enable high transmission speeds and high link reliability. However, almost all the existing works assume perfect channel estimation, which is a critical task in the receiver design, and is extremely challenging in the UWA communication context due to the large number of unknowns as a result of large delay and Doppler spread. A work on channel estimation of doubly selective UWA channels based on the use of a basis expansion model first, to reflect the time-varying nature of the channel (Qu and Yang, 2008) (Leus and Van Walree, 2008) through which some subspace algorithms, namely root-MUSIC and ESPRIT, can be applied for channel estimation (Van Trees, 2002) (Pesavento, et al., 2000).

Inspired from array processing, a subspace method can be applied to determine the distinct path arrivals, after which the complex path gains can be estimated based on pilot subcarriers. However, it has been shown that these techniques work well only for channels that have limited Doppler-spread. Also, the number of the unknowns that need to be estimated increases substantially depend on the time varying nature of the UWA channel,

imposing substantial demands on the channel estimation (Qu and Yang, 2008) (Leus and Van Walree, 2008). Channels with mild or more severe Doppler distortion require dedicated intercarrier interference (ICI) equalization (e.g., (Li, et al., 2008) and (Huang et al., 2011)) and channel estimation is typically accomplished using pilots only (Li et al., 2008), (Huang et al., 2011), (Stojanovic, 2008), or decision feedback instead or in addition to pilots (Li et al., 2009), (Radosevic et al., 2011).

The channel estimation algorithms described in the recent literature have been mainly based on exploiting the sparse nature of UWA channels (Li and Preisig, 2007), (Stojanovic, 2008). Given sufficiently wide transmission bandwidth, the impulse response of the underwater acoustic channel is often sparse as the multipath arrivals become resolvable (Stojanovic, 2009). Also, in the presence of large Doppler spread, channel estimation algorithms have been recently shown to be highly effective, based on experimental results for both single-carrier (Cotter and Rao, 2002) and multi-carrier (Berger et al., 2010), underwater transmissions. In these works, orthogonal matching pursuit (OMP) and other basis pursuit (BP) variants have been tested and based on the simulation and experimental studies, it was shown that BP has better performance than OMP in the UWA environment.

A channel estimation for relay-based UWA systems is investigated in (Panayirci et al., 2016). The authors considered a sparse CIR and a non-Gaussian channel gains in their channel model. The expectation-maximization (EM) along with the matching pursuit (MP) algorithms were employed for the Doppler shift and the delay estimation. In (Ma et al., 2017), the authors adopted superposition coding with OFDM for downlink communication in the presence of multiple stations (sensors).

Based on statistical representation of each underwater station's channel state information (CSI), a resource allocation mechanism is proposed that obtains the transmitting power of each subcarrier for each user. An adaptive channel estimator based on least squares (LS) and recursive least-squares (RLS) is proposed in (Shi and yang, 2016). The results show a promising bit error rate (BER) performance and the average mean square error (MSE) can be obtained better than the linear minimum mean square error (LMMSE) or the LS. The authors of (Kumar and Sarvgaya, 2016) investigated different modulation, channel estimation, and channel equalization techniques for OFDM-based and pilot-assisted UWA systems. They assumed in their simulations a channel that follows a

Rayleigh distribution. Their results show that QPSK, DPSK, and 16QAM are the most suitable modulation schemes for UWA applications. The authors of (Yu et al., 2015) proposed a low computational complexity channel estimation algorithm based on fast block-Fourier transform (FFT) and orthogonal matching pursuit (OMP) in the presence of large pilot spacing. In (Peng et al., 2015), the authors proposed an OMP-based algorithm for channel coefficients estimation with no prior CSI knowledge in the presence of doubly selective channel. Two different Doppler estimation techniques are discussed in (Ahmed, 2015) for pilot-assisted OFDM-based UWAC systems. The first technique consider a cross correlation operation performed on the observed signal with the local known OFDM symbol, then the peak location(s), after that, the authors compare each peak location with the corresponding known peak location, where the difference determines the Doppler scale. The other technique is very close to the first one; mainly, after determining the peak using the local signal, an auto correlation operation is performed on the successive data OFDM symbol to determine the peak location(s). The authors compare the peak location with the reference of the corresponding peak location, where the difference in peak location pairs defines the Doppler shift ( $\hat{\gamma}$ ). In both approaches, however, a sampling operation is performed in the time domain on the observed signal in order to compensate the dominant Doppler shift, i.e.  $\frac{t}{1+\hat{\gamma}}$ .

The noise generated in acoustic type of communication in underwater has also received efforts, due to the fact of its high power. In such environment, the main resource of noise is not only the activities of the ships, and other man-made sources, shrimps, rainfall, and wind contribute in noise generation. Authors of (Jenserud and Ivansson, 2015) proposed a study that shows a better channel impulse response modeling when out-of-plane scattering and reverberation are taken into account, whereas the authors of (Kuai et al., 2016) proposed an algorithm where the receiver can detect the impulsive noise positions using the signal amplitude in the time domain, and the impulsive noise and the Doppler shift estimation are based on the null subcarriers of the OFDM symbol.

In (Chen et al., 2017), the authors consider impulsive noise in the underwater region due to the generated by snapping shrimps and other sources noise sources, where an impulsive noise mitigation operation is carried out on the received signal. Basically, the authors consider the non-zero channel coefficients at the pilots, where the impulsive noise is detected by calculating the average power of the current OFDM block, then collects the



positions of possible impulsive noise into a vector that are greater than a predefined power threshold, then the algorithm subtracts the estimated impulsive noise from the received signals. Another channel estimation approach was discussed in (Liu, et al., 2016). The authors consider the non-zero paths in their channel estimation (CE) procedure, where an inverse direct Fourier transform (IDFT) operation is performed and then the algorithm selects the paths with high powers, then convert it back to the frequency domain through direct Fourier transform (DFT) operation, then the signal is equalized.

The reminder of this work is organized as follows. Chapter 2, investigates the state of the art of the underwater acoustic communications, the underwater channel characteristics, and an introduction to Bellhop acoustical toolbox. Chapter 3, discusses the proposed channel estimator along with the proposed channel and system models. In addition, chapter 3 proposes an extension to the proposed model with detailed formula derivations and simulation results with comparisons. Chapter 4, discusses the proposed channel estimation algorithm proposed for a multiple-input-single-output type of communication. Finally, chapter 5 contains concluding remarks.

### **1.3 Contribution of This Work**

In this work, a synthetic type of channel impulse response (CIR) generated using Bellhop MATLAB-wrapper acoustic toolbox is proposed for the channel estimation problem considering the characteristic of underwater region of Sapanca Lake in Turkey. However, the proposed channel estimators are computational friendly. In the first approach, a SISO type of communication is proposed with correlated colored Gaussian noise to be added to the received signal in order to simulate a real underwater environment, where the second approach assumes a MISO type of communication with white noise, which also fits in underwater environments. In addition, the first approach assumes Rician fading channel, whereas the second algorithm assumes Rayleigh fading.

The main difference of the work in chapter 3 and (Panayirci et al., 2016) is that, this work is concerned with a synthetic type of channel based on a real environment obtained from Sapanca Lake in Turkey using the BELLHOP-MATLAB acoustic toolbox (Porter, last accessed, 2018), whereas the work in (Panayirci et al., 2016) assumes an exponentially decaying type of channel. In addition, the channels proposed in chapter 3 assumes Rician fading, whereas the channels in (Panayirci et al., 2016) undergo Rayleigh fading.

Moreover, in this work of chapter 3, maximum a *posteriori* (MAP) is proposed for channel gains estimation with maximum likelihood (ML) for the prior densities estimation, whereas in (Panayirci et al., 2016) Expectation Maximization (EM) algorithm was employed. Finally, the work in (Panayirci et al., 2016) investigates a system model with cooperative-based system, while in this work in chapter 3 the system model deals with direct communication.

The main difference of the work in chapter 4 and (Cirpan, Panayirci, & Dogan, 2006) is that this work assumes space-time type of diversity, whereas the work in (Cirpan et al., 2006) assumes a space-frequency one. In addition, the work in chapter 4 uses a sparse underwater channel generated by BELLHOP-MATLAB acoustic toolbox for Sapanca Lake in Turkey, where the work in (Cirpan et al., 2006) uses an exponentially decaying channel. Finally, the work in chapter 4 is extended by using ESPRIT algorithm for sparse channel delay estimation and a comparison of it is shown with the work discussed in (Cirpan et al., 2006).

## **2. STATE-OF-THE-ART ON UNDERWATER ACOUSTIC COMMUNICATIONS**

In this chapter, the main characteristics of underwater acoustic communication will be discussed. The objective of this chapter is to provide an insightful knowledge on the challenges and impairments that acoustic signals face in underwater environment.

### **2.1 History of Underwater Acoustical Communications**

In 400 BC, Aristotle had noted that sound could be heard in underwater medium as well as in the air. In 15th century, Leonardo da Vinci observed the wireless communication can be made over acoustical signals in underwater environment, where his words were “If you cause your ship to stop, and place the head of a long tube in the water and place the outer extremity to your ear, you will hear sips at a great distance from you” (Vaccaro, 1998). Due to the development of electronic devices, the use of underwater acoustics has been made through hydrophones, where the latter converts the acoustic energy into electrical signal (and vice versa). Since then, several articles were made on underwater acoustic signal processing (UASP) considering solutions of multipath spread, rapid channel fluctuations, significant ambient noise, and channel estimation.

### **2.2 Why Acoustic Signals**

Many contributions regarding wireless communications in underwater environment are well studied to enhance the performance of the overall wireless-based communication system. In order to fulfill a wireless communication link in underwater environment; there exist three candidate type of signal waves (electromagnetic, optical, and acoustic) proposed to achieve this task, where the acoustic signals are found to be the most suitable. Electromagnetic (EM) waves have been deployed in wireless communication for over a

century achieving a superior performance in terrestrial wireless communications offering a robust wireless link with a decent speed of propagation that provides an insignificant delay for real-time applications. Unfortunately, the radio waves were found to experience high attenuation for underwater wireless communications because of the conductive nature of the underwater medium, where a higher transmission power has to be used in order to solve this problem (Zhou and Wang, 2014).

Lately, the trend of communication over visible light has received a lot of interest among researchers, and numerous number of well-written papers are proposed for communication over this type of signals. Regrettably, due to the nature underwater medium, the optical signals scatters, and the optical powers can be absorbed rapidly (Webster et al., 2017).

Fortunately, acoustic signals are found to be capable of achieving this type of wireless communication with minimal damage and considered as the best candidate for wireless communication in underwater environment. Research papers for this type of signals in underwater medium are increasing tremendously due to its unique characteristics such as temporal variations, abundance of transmission paths, and wideband property in nature (Bernard and Meinig, 2011). Table-2.1. summarizes the different characteristic of acoustic, EM, and optical waves in underwater medium (Zhou and Wang, 2014).

Table 2.1 Comparison of acoustic, EM and optical waves in underwater medium

	Acoustic	Electromagnetic	Optical
Nominal speed (m/s)	~ 1500	~ 33 333 333	~ 33 333 333
Power loss	relatively small	large	$\propto$ turbidity
Bandwidth	~ kHz	~ MHz	~ 10 - 150 MHz
Frequency band	~ kHz	~ MHz	~ $10^{14}$ - $10^{15}$ Hz
Antenna size	~ 0.1 m	~ 0.5 m	~ 0.1 m
Effective range	~ km	~ 10 m	~ 10 - 100 m

### 2.3 Characteristics of Underwater Acoustic Channel

Acoustical signals experience a different type of dilemmas other than those that can be found in terrestrial communication over EM or optical waves. In the next context, part of the characteristics that distinguish underwater acoustical communication will be

introduced, which make underwater acoustical channel one of the most challenging channels for wireless communication.

### 2.3.1 Sound Velocity

The propagation speed of the sound signals is extremely slow compared to the EM and optical waves. The average speed of acoustic signals in underwater medium is 1500 m/s (Wang and Wang, 2016). Acoustic signals propagate with different speeds in underwater environments. Basically, the acoustic signals propagate with different speeds that depend on the depth, the water temperature, and the water salinity (Porter, last accessed, 2018). However, a typical speed of sound in water near the ocean surface is about 1520 m/s, which is more than 4 times faster than the speed of sound in air (~ 343 m/s), but five orders of magnitude smaller than the speed of light. The water layers can be categorized into three main layers (Zhou and Wang, 2014)

- *Surface layer*: this layer is also referred to as *mixed layer*. The depth of this layer is within tens of meters away from the water surface, where the salinity and the temperature of the water in this layer tend to be homogenous (due to the effect wind) that leads to a constant sound velocity of the acoustic waves. This layer is also called *shallow water*.
- *Seasonal and permanent thermocline layers*: this layer is the second deeper layer than the surface layer, where the water temperature decreases in this layer as the depth increases, and the temperature varies from season to season.
- *Deep isothermal layer*: in this layer, the temperature is almost constant for all depths, where the water pressure plays role in determining the acoustic wave speed.

### 2.3.2 Propagation Loss

The strength of the received signal is quite related to the placement of base stations, in the underwater environment. Based on the surface (sea conditions) and the bottom topology of the underwater area, each channel gain can be assumed to have different distribution statistical characterization. For instance, when the receiver is in shallow water and close to the transmitter, diffuse random multipath contributions are negligible and the

channel tap gains can be assumed to obey the Rician distribution. On the other hand, with increasing distance between the transmitter and the receiver, the large sea dynamics prevent direct path contributions, and consequently, the diffuse multipaths dominate, resulting in the channel gains having Rayleigh distribution. Since the underwater communication topology is in a continuous change, the channel tap gains may also obey other type of distributions, such as log-normal and Nakagami-m distributions.

Acoustical waves experience two different energy loss factors while propagation in underwater medium. Mainly, the absorptive and the scattering (the bottom and the surface loss) loss due to the geometry of the underwater region. The scattering of sound coming from the sea surface and the scattering and the absorption of the sound waves from the sea floor can also contribute significantly into signal attenuation and dominant when the base stations are placed in shallow water.

Finally, the refraction and reflection of sound (which mainly depend on the sea conditions, sea floor type, isothermal layer depth, sudden and unexpected temperature changes in underwater etc.,) can create the so called phenomena *shadow zone* resulting in a significant attenuation of signal energy (Nguyen et al., 2009). Due to the scattering and the large fading of the acoustic signals, the channel impulse response is considered to be a time variant *sparse* channel, and only received taps with significant powers are considered.

### 2.3.2.1 Absorptive Loss

In general, underwater applications operate in low frequency, where the pH of the water in the underwater region plays an important role in the attenuation, that is, the higher the pH, the larger the attenuation, where an accurate attenuation computation is a must (Browning et al., 1988). In underwater medium, the energy of acoustic wave converts to heat. The frequency-dependent loss experienced by acoustic waves occurs due to the existence of the chemical substances (boric acid  $\alpha_1$ , magnesium sulphate  $\alpha_2$ , and viscosity of water  $\alpha_3$ ). Different contributions on underwater absorption were made for a better acoustic wave attenuation estimation. The frequency-dependent loss can be expressed as (Moll, et al., 2009):

$$\alpha = \alpha_1 + \alpha_2 + \alpha_3, \quad (2.1)$$

where

$$\alpha_1 = A_1 \frac{f_1 f^2}{f_1^2 + f^2} e^{(pH-8)/P_1}$$

- $f_1 = F_1 \left(\frac{S}{35}\right)^{S_1} e^{T/T_1},$

$$\alpha_2 = A_2 \left(1 + \frac{T}{\theta_2}\right) \left(\frac{S}{35}\right) \left(\frac{f_2 f^2}{f_2^2 + f^2}\right) e^{-z/z_2},$$

- $f_2 = F_2 e^{T/T_2},$

- $\alpha_3 = A_3 P_3 f^2,$

where  $A_3$  and  $P_3$  can be estimated as follows:

- $A_3 = 4.937 \cdot 10^{-4} - 2.59 \cdot 10^{-5} T + 9.11 \cdot 10^{-7} T^2 - 1.5 \cdot 10^{-8} T^3$  , for  $T \leq 20$  °C,

- $A_3 = 3.964 \cdot 10^{-4} - 1.146 \cdot 10^{-5} T + 1.45 \cdot 10^{-7} T^2 - 6.5 \cdot 10^{-10} T^3$ , for  $T > 20$  °C,

- $P_3 = 1 - 3.83 \cdot 10^{-2} z + 4.9 \cdot 10^{-4} z^2,$

where  $f$  is in kHz,  $pH$  in NBS, salinity ( $S$ ) in g/kg, temperature ( $T$ ) in Celsius, depth ( $z$ ) in km. The formula results in an absorption value measure in decibels per kilometer (dB/km). For simplicity, a simplified version of the attenuation formula can be used called *Thorpe* attenuation which can be expressed as (Zhou & Wang, 2014):

$$\alpha^{Thorpe}(f) = \frac{40 f^2}{4100 + f^2} + \frac{0.1 f^2}{1 + f^2} \quad (2.2)$$

where  $f$  is the carrier frequency in kHz and  $\alpha^{Thorpe}$  is in units of dB/m. For the case of an ultra-high frequency (UHF) deployment is assumed in underwater mediums (up to 10 GHz), Akhiezer and Landau-Rumer type of attenuation should be considered (Telichko, et al., 2015).

### 2.3.2.2 Scattering Loss

In underwater medium, the scattering loss of the sound waves increases as the acoustic wavelength decreases. Scattering in underwater is induced by the roughness of the water surface and sea bottom, whereas high interface roughness induces large spatial energy dispersion. The scattering occurred by the bottom mainly depends on the roughness of the geology of the sea bottom such as, sand ripples, and roughness of the rocks.

An important scattering parameter in the surface side is the environmental conditions of the sea, that is, in the presence of high wind, where the wind-generated waves increases the roughness of sea surface, and the higher the scattering order is experienced (Yuan et al., 2016).

### 2.3.3 Ambient Noise and Interference

In any communication system, signal-to-noise ratio (SNR) is very essential for ensuring a smooth and reliable carriage of the transmitted data. SNR, however, gives a comparison of the strength of the intended signal to that of the noise. In underwater acoustical communication, depending on the sea conditions, the acoustic channel can be considerably affected by the ambient noise generated by the diverse origins.

The ambient noise experienced in underwater environment is relatively high. Different natural sources of noise such as surface waves, rainfall, biological sources (marine mammal vocalizations, snapping shrimp) and other man-made sources (underwater machineries, ships and boats) affect the acoustic communication in underwater medium (Chitre et al., 2006) (Guimarães et al., 2014). For instance, in (Adzhani et al., 2016), the experiment shows a wind noise of 50 dB, where the experiment in (Prince et al., 2015), shows an aerial noise in the range of [46.8, 53] dB, where the rainfall (depending on the precipitation) can produce noise up to 50 dB, whereas noise spectrum level decreases with increasing frequency from about 140 dB at 1Hz to 30 dB at 100 KHz (Santoso et al., 2015). Consequently, modulation order in underwater coherent communication systems plays an important role in data detection at the receiver side. SNR can be given in the following formula:

$$SNR(d, f) = 10 \log_{10} (P_S) - T_l - 10 \log_{10} (P_N), \quad (2.3)$$

where  $P_S$  is the total signal power,  $T_l$  is the transmission lose,  $P_N$  is the total noise power, and the final result of SNR is then measured in *dB*. However, the transmission loss  $T_l$  presented in (2.3) is a function of the distance, ( $d$ ) and the attenuation factor  $\alpha(f)$  (discussed in subsection 2.3.2.1). It was stated in (Iqbal et al., 2013), that the total noise power ( $P_N$ ) can be divided into four main sources, mainly, noise generated by ships activities, noise generated by wind, noise generated by heat, and noise generated by turbulence. Consequently, the noise equation can be formulated as:



$$N(f) = N_s(f, S) + N_w(f, W) + N_h(f) + N_t(f), \quad (2.4)$$

where

$$N_s(f, S) = 40 + 20 (s - 0.5) + 26 \log_{10}(f) - 60 \log_{10}(f + 3),$$

$$N_w(f, W) = 50 + 7.5\sqrt{w} + 20 \log_{10}(f) - 40 \log_{10}(f + 0.4),$$

$$N_h(f) = -15 + 20 \log_{10}(f),$$

$$N_t(f) = 17 - 30 \log_{10}(f).$$

There exist huge efforts for acoustical noise estimation and measurements in underwater environments, i.e., QUONOPS and LIDO systems (André, et al., 2016). QUONOPS system is connected to several underwater sensors at different bathymetries, while temperature and salinity measurements process is carried on. In LIDO is responsible for automatic processing of an acoustic data from the observed signals. Basically, it measures the noise levels, then identifies the acoustic source that contributed to the measured acoustical noise. Finally, an online interface can be accessed for real-time monitoring.

On the other hand, the EU Ocean of Tomorrow program has started AQUO project to achieve quieter oceans by shipping noise footprint reduction. The methodology was to take into account all the key components and measurements of noise coming from ships as the noise source at the receivers, basically sensors. The procedure they pursued is presented in Fig. 2.1 (André, et al., 2016).

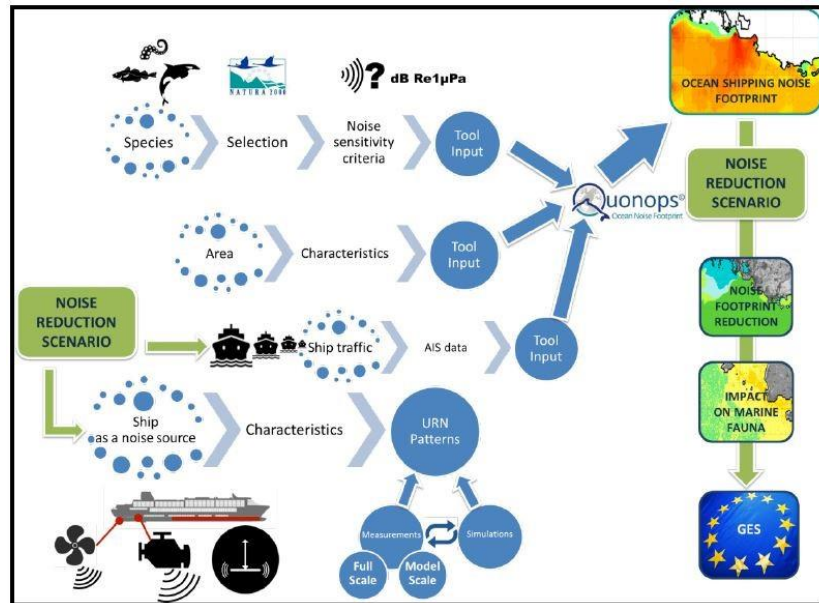


Figure 2.1 Illustration of the overall AQUO methodology.

However, the main two parts of their study regarding the man-made noise reduction are:

- A noise footprint assessment tool development was formed,
- A development of the radiated noise model of ships was developed, that consider a variety of commercial ships and their corresponding characteristics.

However, depending on the underwater area and sea conditions, the noise modelling for wireless *acoustical* communication in such environment has been growing. For instance, (Liling and Dupeng, 2017) came up with a solution for underwater noise stimulated by an airborne source. The study uses the propagator matrix and the wave number integration to establish an air and underwater acoustic field spatial distribution model stimulated by the moving source in the air.

### 2.3.4 Large Doppler Shift

Due to the nature of acoustic signals, a major change in the wavelength (frequency) of the sound wave that arises as a result of the medium instability (i.e., movement of the transmitter/receiver due to wind) (Beygi and Mitra, 2015). This kind of frequency change is referred to as Doppler shift or Doppler effect. Because the moving surface of the sea, the Doppler shifts have an unpredictable variant values. Consequently, underwater acoustic communications (UWACs) are fragile to Doppler shift, where the relatively low sound speed in underwater medium generates a large Doppler shift. For example, in the presence of an acoustic wireless communication with a carrier frequency centered at  $f_c = 20$  kHz, where the average velocity of the sound wave in underwater medium is approximately. 1500 m/s, thus the Doppler shift induced by the *moving sea surface* for a system placed in shallow water with a received line of sight (LOS) signal can be determined as (Ha et al., 2017):

$$f_{T_X S_n} = \frac{V_{S_n} \times f_c}{C_S} \cos(\theta_{S_n}) = \frac{1.5 \times 20,000}{1500} = 20 \text{ Hz},$$

where  $\theta_{S_n}$  is the angle between the surface-normal velocity  $V_{S_n}$  and the scatterer-transmitter axis,  $C_S$  is the speed of the acoustical signal. For the case when the received signal is a scattered component, the Doppler shift formula can be expressed as:

$$f_{S_n R_X} = (f_c + f_{T_X S_n}) \times \frac{V_{S_n}}{C_S - V_{S_n} \cos(\theta_{R_n})} \cos(\theta_{R_n}),$$

where  $\theta_{R_n}$  is the angle between the surface-normal velocity  $V_{S_n}$  and the scatterer-receiver axis, and the total Doppler shift generated by the *sea surface* can be expressed as:

$$f_{D,S_n} = f_{S_n R_X} + f_{T_X S_n}.$$

However, Doppler shift can also arise due to the movement of the receiver, and thus, can be given by this formula

$$f_{i,n} = \frac{f_c \times V_R}{C_S} \cos(\alpha_{i_n}) \cos(\pi - \alpha_V^R),$$

where  $f_{i,n}$  is the resulting Doppler shift of the  $n^{th}$  path  $\alpha_{i_n}$  is the angle of arrival (AOA), and  $i = 1, 2$  which denotes the signal is reflected from surface ( $i=1$ ) or bottom ( $i=2$ ), respectively.

### 2.3.5 Long propagation Delay

Multipath spread is a significant characteristic of the underwater acoustic communication channels affecting the channel impulse response at the receiver side, where the long propagation delay experienced in this region is due to the low sound speed. In addition, the reflection of the sound wave off the sea surface and sea floor as well as the refraction of sound such as bending rays of the propagation paths create many different propagation paths, and hence, the underwater channel is considered to be time-variant. Mainly, the nature of the underwater environment is responsible of creating the multipath channel, where the longer the communication range, the longer the delay experienced at the receiver side. The wave reflections from the surface and the bottom generate several arriving taps (sparse type of channel with large delay spread) can be observed at the receiver in applications that use transmitter/receiver placement in shallow water, whereas, the applications where transmitter/receiver are placed in deep water, the surface and bottom reflections can be neglected (Zhou and Wang, 2014)] (Nguyen et al.,2009) (Mason et al., 2008).

### 2.3.6 Multipath Propagation and Channel Models

Channel modelling provide an excellent tool for predicting the performance of underwater acoustic communication systems before their deployment, and, of course, they are very essential for system design.

One of the essential dilemmas in the underwater acoustical communication is the corruption of the data, due to multipath interference. Underwater acoustic communications suffer from the time variant type of channel. A particular underwater channel can be represented depending on the sea conditions, the range of communication, and the depth of the stations. At the receiver, the received signals can be direct, reflected, scattered from the surface and bottom, or refracted by variations in the acoustic velocity profile, which lead to multipath propagation. Thus, the received signals then suffer from severe and rapid amplitude fluctuations and fading. When the communication range is short, then the receiver will experience a direct path (steady component), and different random paths (diffused components) which can be as a result of boundary scattering. In the case of long communication range, the received signal is then a superposition of a number of time-delayed, randomly propagated components arriving via different paths (Falahati et al., 1991).

Figs 2.2 and 2.3 attempt to simulate the time-varying characteristics of underwater channels observed experimentally.

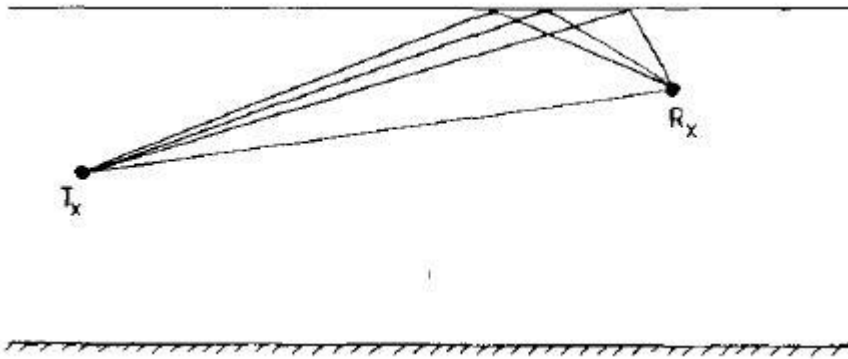


Figure 2.2 Short-range propagation.

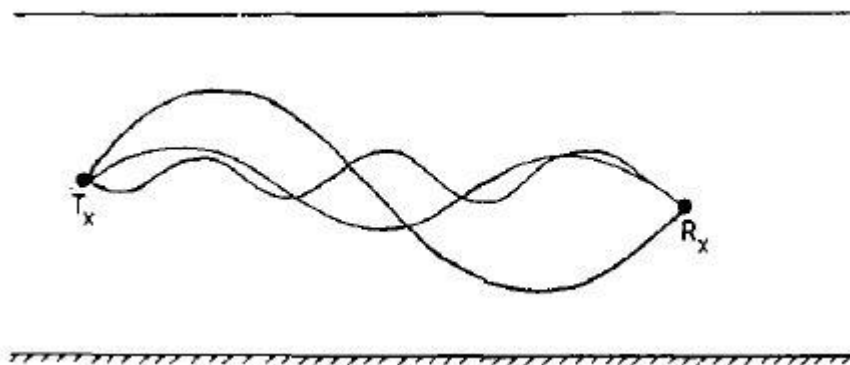


Figure 2.3 Long-range propagation

Multipath causes a receiving of a series of pluses at the receiver, that are originally a single impulse sent from the transmitter. In the case of a multiple echoes, the received data can overlap in time, thus, become degraded. This type of interference can be largely avoided by using asynchronous serial transmission. In this type of transmission, the transmitter sends of short signal, each followed by a much longer quiet period. However, a suitable arrangement of the transmitting and receiving transducers has to be made. However, all the signals are then received before the next burst is transmitted.

Successful channel models that can be found in the literature are based on statistics. Mainly, a statistical channel model encounter physical laws of acoustic propagation (frequency-dependent attenuation, bottom/surface reflections). In addition, these statistical channel models reflect the effects of inevitable random local displacements. Specifically, random displacements that involve distances on the order of a few wavelengths (small-scale effects), and those that involve many wavelengths (large-scale effects). The small-scale type of effects includes the scattering and the motion-induced Doppler shifting. The aforementioned effects are responsible for the fast variations of the instantaneous channel response. On the other hand, the large-scale type of effects describes the location uncertainty and the changing environmental conditions, and thus, affects the averaged power of the received signals. Since the transmission conditions in the underwater environment differ from the nominal ones due to the changes in system geometry and environmental conditions. Consequently, the necessity of having a *relatively* accurate channel model is a must. However, the channel model is responsible for allocating the appropriate resources (power, bandwidth) before system deployment, as well as to examine the pre-designed signals processing techniques on both the physical link layer and the higher network layers. Channels can be generated at labs. Using a *ocean wave basin*, a real underwater channel can be modeled. Moreover, an experimental type of channel is always preferred to study the behavior of channel estimators. Experimental channels take into consideration the exact depths of the underwater area, the sediments, the Doppler scales per path, real-time delays, and the exact type of sea bottom including the what exist at the bottom i.e., sand ripples roughness of the rocks. However, a technique for channel modeling known as *beam tracing* that consider underwater acoustic communications can be found in an *acoustical toolbox* known as *BELLHOP*, more about BELLHOP is discussed in the next section.

## 2.4 Bellhop Acoustic Toolbox

In this section, an overview about BELLHOP acoustical toolbox will be given. Note that, BELLHOP is an open source software, and it does not come in a standalone fashion, it comes wrapped in another compiler, i.e. MATLAB-wrapper BELLHOP.

### 2.4.1 Overview

Bellhop is a set of algorithms that trace the ray in underwater environment. It was originally written in *Fortran* language, later on, programmers prepared many versions of Bellhop written in different languages to support different operating systems (Porter, last accessed, 2018). BELLHOP uses ray theory to provide an accurate deterministic picture of the underwater channel.

In addition, Bellhop is capable of producing various useful outputs such as, ray coordinates, travel time and amplitude forming channel impulse response, eigenrays, and transmission loss. The ray trace, which shows the propagation paths of the acoustic signals for the given underwater region and communication specifications along the communication range. In addition, user can find the channel impulse response through requesting the time of arrival and amplitude of the arriving acoustic signals. In order to run Bellhop, the user inputs the sound speed profile associated with the specifications of the underwater region, and requests the desired output.

Bellhop considers sea surface heights with a single valued function of position and time, whereas in *Virterx* (Virtual Timeseries EXperiment), which is an update version of Bellhop, it approximates the motion of the environment itself by a sequence of snapshots with different heights instead of one snapshot as in Bellhop. In addition, *Virterx*, along with its advancements, has the ability to include the motion of the source, and/or the receiver in its calculation, with an unsteady sea surface motion, where the Doppler introduced by the unsteady sea surface motion is calculated by the eigenray data produced by Bellhop. *Virterx* was developed to simulate the effect of channel variation in a manner that is computationally more efficient than repeated application of the Bellhop beam tracing. This algorithm operates by tracing multiple interrelated beams to assess the cumulative effect on the signal of a given frequency. However, the complexity of *Virterx* may still have an issue. For instance, it takes around of 15 seconds for a two-transmitters

and six-receivers underwater communication system to simulate a channel using *Virtex*. In each second, *Virtex* requires around 30 channel realizations, which leads to a total of 5400 runs of BELLHOP, considering a Doppler distortion of the order of 0.015 KHz (Qarabaqi and Stojanovic , 2013).

#### **2.4.2 Environmental Profile**

The input file to Bellhop is called environmental profile. In this profile, the specifications of the underwater region along with the acoustical wireless communication link are imputed in the file manually along with the intended output. The wireless communication link information consists of the carrier frequency, the antenna aperture, the depth and the number of the transmitter/receiver, the number of beams to be sent considered per transmission, and the communication range. In addition, Bellhop offers a set of interpolation techniques (cubic spline interpolation, C-linear interpolation, N2-linear interpolation, and analytic interpolation) where user can specify the technique in order to find the sound speed and its derivatives along the ray.

Moreover, different acoustic pressure approximations are proposed by Bellhop to be inserted in the environmental profile (geometric beams, Cartesian beams, use ray-centered beams, Gaussian beam bundles). In addition, attenuation can be specified in different units (dB/m (kHz), Nepers/m, Q-factor, and dB/wavelength). However, Bellhop gives the ability for users to include the surface type and bottom shape as flat shaped or user can include them using an external file for a better ray tracing and arrival signal channel. One of the most important aspects of the communication over acoustic signals in underwater environment is the sound speed profile. This profile reflects the speed of the signal at different depths in the underwater region.

In other words, according to the transmitter/receiver depths, the signal propagates in the underwater region towards the bottom of the underwater region and the surface sides, where the speed of the sounds is not constant along the depths, consequently the channel impulse response is affected. Unfortunately, BELLHOP does not encounter the random channel variation (Qarabaqi and Stojanovic, 2013).

In order to cope with channel modeling, different studies were carried on modelling the UWA channel stochastically, e.g., (Qarabaqi and Stojanovic, 2009) (Ruiz-Vega, Clemente, Otero, & Paris, 2012). However, these studies were shaped based on the

analysis of an experimental type of an acoustic data, collected in a particular location. Depending on the system model of the study, the underwater channel was found to obey a Rician fading (Qarabaqi and Stojanovic, 2009), (Radošević et al., 2009) or Rayleigh fading (Socheleau et al., 2009), (Galvin and Coats, 1996), (Chitre M. , 2007).

In addition, fading of underwater channels was also detected to follow log-normal distribution (Qarabaqi and Stojanovic, 2011) (Tomasi et al., 2010), *K*-distribution (Yang and Yang, 2006) (Zhang et al., 2010), and a general class of Rician shadowed distribution (Ruiz-Vega et al., 2012).

### 2.4.3 Sound speed profile

In order to fulfill the task of Bellhop, the sound speed profile (SSP) consists mainly of the sound speeds at different depths. In the case of lack of information regarding the underwater region; users can estimate the sound speed profile through various formulas, such as Medwin formula as follows (Bahrami et al., 2016):

$$SSP(T, S, D) = 1449.2 + 4.6T - 0.055T^2 + 0.00029T^3 + (1.34 - 0.01T)(S - 35) + 0.016D. \quad (2.5)$$

The formula shows that the speed of acoustic signal in underwater medium grows when any of the parameters (T, S, D) increases. At a certain depth, depending on the water temperature, water salinity, and water depth, the formula accurately calculates the speed of the acoustic signal at that specific depth, and the resulting value is the sound speed that can be used along with the corresponding depth in the SSP of Bellhop's environmental profile.



### **3. SPARSE CHANNEL ESTIMATION AND DATA DETECTION FOR OFDM-BASED UNDERWATER ACOUSTIC SYSTEMS IN RICIAN FADING**

In the following sections and subsections, two new pilot assisted channel estimation techniques that employ OFDM transmission scheme in doubly-selective Rician UWA channels are proposed. The chapter fully discusses the first algorithm and presents its simulation results, then the second algorithm, which is an extension of the first one, is then presented with simulations.

#### **3.1 Introduction**

The main contribution in this work is twofold. First, the sparse structure of the UWA channel impulse response is exploited to improve the performance of the channel estimation algorithm, due to the reduced number of taps to be estimated. The resulting algorithm initially estimates the overall sparse channel tap delays and the Doppler shift by using a conventional matching pursuit (MP) algorithm (Cotter & Rao, 2002) (Zhang, Han, Huang, & Nramdt-Pearce, OFDM transmission over time-varying channel with self interference cancellation, 2014), assuming correlated ambient Gaussian noise affecting the system from source to destination. With the path delays and Doppler spread information, then a computationally efficient and low complexity novel channel estimation algorithm is proposed by combining MP and maximum *a posteriori* probability (MAP) estimation to estimate the complex channel path gains whose prior densities have Rician distributions with unknown means and variances. They are, in turn, estimated separately by the maximum likelihood (ML) technique. The likelihood function of those parameters is determined by properly averaging it over the Rician distributed complex channel gains.

This chapter is organized as follows. Section 3.2 presents the system and channel model for an OFDM-based underwater wireless communication system and describes the main parameters of the UWA channel and the ambient noise. Section 3.3 proposes the new sparse channel estimation algorithm. Section 3.4 describes the equalization and detection algorithms for the overall OFDM based UWA communications system. The computation complexity is presented in 3.5, and the computer simulations with BELLHOP simulated channels in Sapanca Lake are presented in 3.6. Section 3.7 presents the second proposed approach which extends the work to a non-uniform Doppler scale and use orthogonal matching pursuit (OMP) instead of MP in the case of white noise. All related equations and simulations of this extension can be found under subsection 3.7. Finally conclusions regarding the two approaches are presented in section 3.8.

### 3.2 System and Channel Model

The proposed UWA communication scenario is OFDM-based in which a single-antenna source node  $S$  transmits information to a single-antenna destination node  $D$ . The UWA channel between source and destination nodes is characterized by multipath propagation, typically with a few significant paths, resulting in a sparse multipath channel model (Mason, Berger, Zhou, & Willett, 2008). This type of channels can be represented by a parametric channel model, consisting of a limited number of distinct paths parameterized by the path delays and path gains. The parametric channel model effectively reduces the dimension of the signal estimation problem, and the corresponding channel estimation can achieve better performance than that of non-parametric channel model-based estimators.

The time-varying UWA channel impulse response (CIR) from source to destination ( $S \rightarrow D$ ) link is sparse and characterized by

$$h(t, \tau) = \sum_{\ell=0}^{L-1} A_{\ell}(t) \delta(\tau - \tau_{\ell}(t)) \quad (3.1)$$

where,  $L, A_{\ell}(t)$  and  $\tau_{\ell}(t)$  denote the number of non-zero paths, the real channel path amplitudes and the time-varying path delays, respectively. In this work, the path gains are assumed on each link to remain constant over one OFDM symbol transmission and vary independently from symbol to symbol. That is,  $A_{\ell}(t) = A_{\ell}, \ell = 0, 1, \dots, L - 1$ .

The continuously time-varying delays  $\tau_\ell(t)$  are caused by the motion of the transmitter/receiver as well as scattering of the moving sea surface or reflections due to sound speed variations (Mason, Berger, Zhou, & Willett, 2008). For the duration of an OFDM symbol, the time variations of the path delays can be approximated well by a Doppler rate as  $\tau_\ell(t) = \tau_\ell - \gamma t$  (Kuai, Sun, & Cheng, 2016) (Beygi & Mitra, 2015). The path delays,  $\tau_\ell$ , are assumed to be constant over an OFDM symbol duration and all paths have a similar Doppler scaling factor, that is  $\gamma_\ell \equiv \gamma$ . However, in general, the Doppler scaling factor can be different for each path (Mason, Berger, Zhou, & Willett, 2008). However, it was stated in (Li, et al., 2009) that as long as the dominant Doppler shift is caused by the direct transmitter/receiver motion, this assumption can be justified.

Taking these assumptions and approximations into account, the time-varying continuous-time multipath UWA channel impulse response model above is simplified to

$$h(t, \tau) = \sum_{\ell=0}^{L-1} A_\ell \delta(\tau - (\tau_\ell - \gamma t)). \quad (3.2)$$

The baseband equivalent channel impulse response of  $h(t, \tau)$  in (3.2) can be determined as:

$$h_b(t, \tau) = \sum_{\ell=0}^{L-1} h_\ell e^{j2\pi f_c \gamma t} \delta(\tau - (\tau_\ell - \gamma t)) \quad (3.3)$$

where  $h_\ell \triangleq A_\ell e^{-j2\pi f_c \gamma \tau_\ell}$ .

The model in (3.2) deals only with real channel path amplitudes,  $A_\ell$ , obtained from a ray tracing technique. However, there are many diffuse multipath components diffracted or scattered by the rough sea and bottom surface. Consequently, the multipath components will have random phases uniformly distributed over  $[0, 2\pi]$ , and by the central limit theorem. In addition, the channel coefficients (taps)  $h_\ell$ 's on the link are assumed to be complex Gaussian random variables with independent real and imaginary parts.

Based on the sea conditions, each channel gain  $|h_\ell|$  can be assumed to have a different distribution. When the receiver is in shallow water and close to the transmitter, diffuse random multipath contributions are negligible and the channel tap gains may be assumed to obey the Rician distribution. On the other hand, with increasing distance between transmitter and receiver, large sea dynamics prevent direct path contributions and mostly the diffuse multipaths dominate, resulting in the channel gains having Rayleigh

distribution. In this work, the channel path gains are a priori assumed to obey a Rician distribution where  $h_\ell$ 's are complex Gaussian random variables with independent real and imaginary parts with mean  $\mu_\ell$  and variance  $\sigma_\ell^2$ . In addition, the Doppler shift on each path is assumed constant, thus, no intercarrier interference (ICI) in the received signal is considered.

Let  $\Omega_\ell = E\{|h_\ell|^2\} = 2\mu_\ell^2 + 2\sigma_\ell^2$  denotes the power profile of the relevant Rician multipath channel, and  $\sum_{\ell=0}^{L-1} \Omega_\ell = 1$ . Moreover, the Rician  $\kappa$  - factor for the  $\ell^{th}$  tap is the ratio of the power in the mean component to the power in the diffuse component, i.e.  $\kappa_\ell = \mu_\ell^2 / \sigma_\ell^2$ , and each channel tap is given by

$$h_\ell = \sqrt{\frac{\kappa_\ell \Omega_\ell}{\kappa_\ell + 1}} \left( \frac{1+j}{\sqrt{2}} \right) + \sqrt{\frac{\Omega_\ell}{\kappa_\ell + 1}} \check{h}_\ell, \ell = 0, 1, \dots, L-1, \quad (3.4)$$

where  $\check{h}_\ell$  is a complex Gaussian random variable with zero mean and unit variance. However, by taking  $\kappa = 0$ , a Rayleigh distributed underwater acoustic channel model can be also taken into account.

The additive ambient Gaussian noise,  $v(t)$ , generated by underwater acoustic channels has several distinct physical origins each corresponding to particular frequency range (Barbeau, et al., 2015).

The power spectral density of the ambient noise is assumed to be in the 10 - 100 kHz band as a function of frequency in Hz as

$$S(f) = \frac{f_0 \sigma_0^2}{\pi(f^2 + f_0^2)}, \quad (3.5)$$

where  $\sigma_0^2$  is the noise variance, and  $f_0$  is chosen as a model parameter of the colored noise autocorrelation function ( $f_0 T_s = 0.01, 0.05, 0.05, 0.1, etc.$ ), where the autocorrelation function of the ambient noise can be obtained from (3.5) as

$$R_v(t, t') = \sigma_0^2 e^{-2\pi|t-t'|f_0 T_s}, \quad (3.6)$$

where  $T_s$  is the sampling period. In addition, an assumption that the CIR remains constant over a period of one block transmission and varies independently from block to block is considered.

At the source node, the OFDM based UWA system with  $N$  subcarriers employs actively  $K$  subcarriers to transmit data symbols and nothing is transmitted on the remaining  $N - K$  subcarriers. During any OFDM symbol, each active subcarrier is modulated by a data symbol  $d_m[k]$ , where  $m$  and  $k$  represent the OFDM symbol index and the subcarrier

index, respectively. After taking an  $N$ -point inverse fast Fourier transform (IFFT) of the data sequence and adding a cyclic prefix (CP) of duration  $T_{CP}$  before transmission, to avoid intersymbol interference (ISI), the basedband-equivalent, continuous time-domain transmitted signal can be expressed as

$$s(t) = \frac{1}{\sqrt{N}} \sum_{m=0}^{M-1} \sum_{k=-\frac{K}{2}}^{\frac{K}{2}-1} d_m[k] \exp\left(\frac{j2\pi k}{T} (t - mT_{SYM} - T_{CP})\right) \otimes gT(t), 0 \leq t \leq T_{SYM}, \quad (3.7)$$

where  $\otimes$  denotes linear convolution and  $gT(t)$  is the impulse response of the transmitter filter.  $T_{SYM} = T + T_{CP}$  is the total OFDM symbol duration and  $\Delta f = 1/T$  is the OFDM subcarrier spacing. Then, the received passband signal can be expressed as

$$\begin{aligned} \tilde{y}(t) &= \tilde{s}(t) \otimes h(t, \tau) + \tilde{v}(t) \\ &= \sqrt{2} \Re e \left\{ \left( \sum_{\ell=0}^{L-1} h_{\ell} e^{j2\pi f_c \gamma t} s((1 + \gamma)t - \tau_{\ell}) \right) e^{j2\pi f_c t} \right\} + \tilde{v}(t), \end{aligned} \quad (3.8)$$

where  $\Re e \{z\}$  denotes the real part of  $z$  and  $\tilde{v}(t) = \sqrt{2} \Re e \{v(t)e^{j2\pi f_c t}\}$  is the passband representation of the additive correlative Guassian ambient noise  $v(t)$ .

However, in typical UWA communication systems, the receiver directly samples the passband signal due to a relatively low carrier frequency (Berger, Zhou, Preisig, & Willett, 2010).

Consequently, resampling, passband-to-baseband downshifting as well as Doppler shift estimation, compensation and channel estimation are often performed in the digital domain.

As specified in (Berger, Zhou, Preisig, & Willett, 2010) (Mason, Berger, Zhou, & Willett, 2008), and (Qi, Wang, & Wu, 2011), to mitigate the frequency dependent Doppler effect in the received signal (3.8), the following three operations are carried out on the sampled received passband signal to obtain the final discrete frequency-domain samples.

- 1) The main Doppler scaling effect is removed through the resampling operation with a resampling factor  $(1 + \hat{\gamma})$  leading to the resampled signal  $\tilde{y}_{RS}(t) = \tilde{y}_{RS}(t/1 + \hat{\gamma})$ . From (3.8) it follows that

$$\tilde{y}_{RS}(t) = \Re \left\{ e^{j2\pi f_c t} e^{j2\pi f_c b t} \sum_{\ell=0}^{L-1} h_{\ell} s((1+b)t - \tau_{\ell}) \right\} + \tilde{v}_{RS}(t), \quad (3.9)$$

where  $b = \frac{\gamma - \hat{\gamma}}{1 + \hat{\gamma}}$ , and

$$\tilde{v}_{RS}(t) = \tilde{v} \left( \frac{t}{1 + \hat{\gamma}} \right). \quad (3.10)$$

The Doppler effect, is divided into a non-zero valued Doppler rate, caused by relative movement of the transmitter and the receiver, and a Doppler spread, centered around zero caused by different travel paths and receiver angle shift. As can be seen from (3.9), the non-zero mean of is removed by the resampling. Consequently, the new residual Doppler shift  $b$  on each path is spread around zero within  $[-v_{max}, +v_{max}]$  (Beygi & Mitra, 2015), after compensation by  $\hat{\gamma}$ ,  $v_{max}$  can be chosen based on the Doppler spread, with resolution  $\Delta v = 2v_{max}/N_v$ , where  $N_v$  is the number of grid points on the Doppler spectrum.

2) At the receiver, the baseband-equivalent received signal  $y_{RS}(t)$  is then obtained from (3.9) via a demodulation process yielding

$$y_{RS}(t) = e^{j2\pi v t} \sum_{\ell=0}^{L-1} h_{\ell} s((1+b)t - \tau_{\ell}) + v_{RS}(t), \quad (3.11)$$

where  $v \triangleq f_c b$ , represents the residual carrier frequency offset (CFO) and  $v_{RS}(t)$  is the baseband equivalent noise of the resampled  $\tilde{v}_{RS}(t)$  as in (3.10). Then a fine Doppler shift compensation is performed on  $y_{RS}(t)$  to obtain  $z_{RS}(t) = y_{RS}(t) e^{-j2\pi \hat{v} t}$ , where  $\hat{v}$  is a fine estimator of  $v$  (Berger, Zhou, Preisig, & Willett, 2010).

3) Finally after perfectly compensating the residual mean Doppler shift by its estimated value  $\hat{v}$ ,  $z_{RS}(t)$  is converted into the discrete-time signal by means of low pass filtering and analog-to-digital (A/D) conversion with sampling interval  $T_s$ .

Since the time varying-channel impulse response is assumed to be constant over the duration of one OFDM symbol and the number of channel paths, and the path delays do not change during an OFDM symbol, it is sufficient to consider channel estimation only symbol by symbol. Therefore, for notational simplicity the OFDM symbol index  $m$  in (3.7) is omitted.

Consequently, with the assumption that  $T_{CP}$  is greater than or equal to the maximum channel path delay, and  $K$  active subcarriers are within the flat region of the frequency response of transmit and receive filters, after the CP removal, the received baseband equivalent discrete-time signal at the sampling instants  $t = mT_{SYM} + nT_s + T_{CP}$ , with  $m = 0$ , can be expressed from (3.7) and (3.11) as follows:

$$z_{RS}[n] = \sum_{\ell=0}^{L-1} h_{\ell} \frac{1}{\sqrt{N}} \sum_{q=-\frac{K}{2}}^{\frac{K}{2}-1} d[q] \exp\left(\frac{j2\pi q}{N} ((1+b)n - \tau_{\ell})\right) + v_{RS}[n], \quad (3.12)$$

where  $N = T/T_s$  and  $\tilde{\tau}_{\ell} \triangleq \tau_{\ell}/T_s$  represents the  $\ell^{th}$  normalized path delay. Similarly,  $v_{RS}[n]$ ,  $n = 0, 1, \dots, N-1$ , is the baseband equivalent discrete-time ambient noise samples obtained through the sampling of  $\tilde{v}_{RS}[n]$ , in (3.9). From (3.5) it can be easily shown that the noise samples are complex-valued and correlated Gaussian distributed random variables with zero means. Hence, the autocorrelation function becomes,

$$R_{v_{RS}}[u] = R_v \left( \frac{u T_s}{1 + \hat{\gamma}} \right) e^{-j\omega_c t \frac{\hat{\gamma}}{1 + \hat{\gamma}} u T_s}. \quad (3.13)$$

An  $N$ -point fast Fourier transform (FFT) is applied to transform the sequence  $z_{RS}[n]$  into the frequency domain. Assuming that the  $K$  subcarriers by which data is transmitted are within the flat region of the transmitter and receiver filters of unity gains, the  $k^{th}$  subcarrier output of the FFT during one OFDM symbol can be represented as

$$\begin{aligned} Z_{RS}[k] &= \frac{1}{\sqrt{N}} \sum_{n=0}^{N-1} z_{RS}[n] \exp\left(-j \frac{2\pi n k}{N}\right) \\ &= \sum_{q=-\frac{K}{2}}^{\frac{K}{2}-1} d_q H[k, q] + V_{RS}[k], \end{aligned} \quad (3.14)$$

where

$$k = -\frac{K}{2}, -\frac{K}{2} + 1, \dots, \frac{K}{2} - 1$$

$$H[k, q] = \sum_{\ell=0}^{L-1} h_{\ell} \exp\left(-j \frac{2\pi q \tilde{\tau}_{\ell}}{N} F_{k,q}(b)\right), \quad (3.15)$$

$$F_{k,q}(b) = \frac{\sin(\Theta_{k,q})}{N \sin(\Theta_{k,q}/N)} \exp\left(-j \frac{N-1}{N} \Theta_{k,q}\right), \quad (3.16)$$

where  $\Theta_{k,q} = \pi(q(1+b) - k)$ . The frequency domain noise samples  $V_{RS}[k]$  in (3.14) are determined from  $V_{RS}[k] = \frac{1}{\sqrt{N}} \sum_{n=0}^N v_{RS}[n] \exp\left(-j \frac{2\pi nk}{N}\right)$ . Consequently, inserting (3.15) into (3.14) the vector form of (14) can be expressed as

$$\mathbf{Z}_{RS} = \mathbf{H} \mathbf{d} + \mathbf{V}_{RS}, \quad (3.17)$$

where

$$\begin{aligned} \mathbf{z}_{RS} &= \left[ Z_{RS} \left[ -\frac{K}{2} \right], Z_{RS} \left[ -\frac{K}{2} + 1 \right], \dots, Z_{RS} \left[ \frac{K}{2} - 1 \right] \right]^T \in \mathcal{C}^K, \\ \mathbf{d} &= \left[ d_{-\frac{K}{2}}, d_{-\frac{K}{2}+1}, \dots, d_{\frac{K}{2}-1} \right]^T \in \mathcal{C}^K, \\ \mathbf{v}_{RS} &= \left[ V_{RS} \left[ -\frac{K}{2} \right], V_{RS} \left[ -\frac{K}{2} + 1 \right], \dots, V_{RS} \left[ \frac{K}{2} - 1 \right] \right]^T \in \mathcal{C}^K, \end{aligned}$$

and the  $[k, q]^{th}$  element of  $\mathbf{H} \in \mathcal{C}^{K \times K}$  is determined from (3.15). It is obvious from (3.14) that the ambient noise vector in the frequency domain,  $\mathbf{V}_{RS}$ , is also a non-white Gaussian. Thus, without going further toward the channel estimation step, the observation model in (3.17) can be reduced to one with additive white Gaussian noise by the use of a noise-whitening filter, based on the singular value decomposition (SVD) of the covariance matrix of  $\mathbf{V}_{RS}$ , as  $\mathbf{R}_{V_{RS}} = \mathbf{U} \mathbf{Y} \mathbf{U}^\dagger$ , where  $\mathbf{U} \in \mathcal{C}^{K \times K}$  is a complex valued unitary transformation matrix,  $\mathbf{Y}$  is a  $K \times K$  diagonal matrix with positive real entries and  $(\cdot)^\dagger$  denotes the conjugate transpose. Therefore, the colored noise can be transformed into a white noise through the linear transformation  $\mathbf{W} = \mathbf{\Psi} \mathbf{V}_{RS}$  where  $\mathbf{\Psi} = \mathbf{Y}^{-1/2} \mathbf{U}^\dagger$  is the whitening matrix and  $\mathbf{W} = \left[ W \left[ -\frac{K}{2} \right], W \left[ -\frac{K}{2} + 1 \right], \dots, W \left[ \frac{K}{2} - 1 \right] \right]^T \in \mathcal{C}^K$  is a white Gaussian noise vector whose components have zero mean and unit variance. Multiplying (3.17) by  $\mathbf{\Psi}$  from the left the following final form of the observation model can be obtained as:

$$\mathbf{Z} = \mathbf{G} \mathbf{d} + \mathbf{W} \in \mathcal{C}^K, \quad (3.18)$$

where  $\mathbf{Z} = \mathbf{\Psi} \mathbf{Z}_{RS}$  and  $\mathbf{G} = \mathbf{\Psi} \mathbf{H} \in \mathcal{C}^{K \times K}$  is the convolution matrix generated from data symbols.



### 3.3 Sparse Multipath Channel Estimation

#### 3.3.1 Preprocessing

In this work, an estimation of a fast time-varying UWA channel, based on the observation model in (3.18) is taken into account. As explained earlier, the overall continuous time channel impulse response is represented by a parametric model in which each distinct path is characterized by a few significant complex-valued path amplitudes,  $\{h_\ell\}_{\ell=0}^{L-1}$ , the normalized path delays  $\{\tilde{\tau}_\ell \triangleq \tau_\ell/T_s\}_{\ell=0}^{L-1}$  and the Doppler spread  $b$ , resulting in a sparse multipath channel model.

In the following subsections, the algorithms are presented to estimate the sparse complex-valued channel gains, channel path delays and Doppler spread in a computationally efficient way. A Rician fading is assumed in which  $h_\ell$  has  $\kappa$ -factor  $\kappa_\ell$ , for  $\ell = 0, 1, \dots, L - 1$ . By taking  $\kappa_\ell = 0$ , a Rayleigh fading is also obtained as a special case.

From (3.18), the computation of the observation vector  $\mathbf{Z}$  at the pilot subcarriers,  $\{\mathcal{P} = \{p_1, p_2, \dots, p_P\} \in K\}$  of the OFDM symbol from which the least-squares (LS) estimates of the diagonal elements of the combined channel matrix  $\mathbf{G}$  can be obtained as:

$$\hat{G}[p_k, p_k] = \frac{Z[p_k]}{d_{p_k}} = G[p_k, p_k] + V[p_k], \quad (3.19)$$

where  $V[p_k] = \sum_{q \in \mathcal{P}, q \neq p} d_{p_k} G[p_k, q] + W[p_k]$ . By means of (3.15) and (3.16), (3.19) can be expressed as

$$\mathbf{Z}_P = \mathbf{A}_P \mathbf{h} + \mathbf{V}_P, \quad (3.20)$$

where  $\mathbf{Z}_P = [\hat{G}[p_1, p_1], \hat{G}[p_2, p_2], \dots, \hat{G}[p_P, p_P]]^T \in \mathbb{C}^P$ ,  $\mathbf{V}_P = [v(p_1), v(p_2), \dots, v(p_P)]^T \in \mathbb{C}^P$  and  $\mathbf{A}_P \in \mathbb{C}^{P \times L}$  matrix given by

$$\mathbf{A}_P = \begin{bmatrix} \xi_1(b) e^{-j2\pi p_1 \tilde{\tau}_0/N} & \dots & \xi_1(b) e^{-j2\pi p_1 \tilde{\tau}_{L-1}/N} \\ \vdots & \ddots & \vdots \\ \xi_1(b) e^{-j2\pi p_P \tilde{\tau}_0/N} & \dots & \xi_1(b) e^{-j2\pi p_P \tilde{\tau}_{L-1}/N} \end{bmatrix}, \quad (3.21)$$

where  $\xi_1(b) = \sum_{q=-\frac{K}{2}}^{\frac{K}{2}-1} \psi_{i+\frac{K}{2}+1, k+\frac{K}{2}+1} F_{k,i}(b)$ ,  $\psi_{m,n}$  is the  $(m, n)^{th}$  element of the matrix  $\Psi$  and  $F_{k,i}(b)$  is given by (3.16).

### 3.3.2 Path Delays and Doppler Spread Estimation

The sparse path delays and the Doppler shift are estimated by the conventional matching pursuit algorithm (Zhang et al., 2014) (Cotter and Rao, 2002). However, in practice, the sparsity assumption does not always hold and consequently may not represent a truly sparse channel impulse response in UWA communications due to the non-integer normalized path delays in the equivalent discrete time baseband representation of the channel. Therefore, such an estimated channel may differ substantially from the original channel. The A/D conversion at the input of the OFDM receiver is implemented first with an oversampling rate  $R_s^{(\varrho)} = \varrho/T_s$ ,  $\varrho = 1, 2, \dots$ , leading to a finer delay resolution matrix  $\mathbf{A}_P^{(\varrho)} \in \mathbb{C}^{P \times N_\tau N_v}$ , called *dictionary matrix*, obtained from the  $\mathbf{A}_P$  matrix in (3.21). Its columns correspond to the  $(\beta, \mathcal{T}_\ell)^{th}$  discrete multipath channel taps and Doppler rate positions, respectively, where  $\varrho$  is the oversampling factor, and  $1/T_s$  is the baseband Nyquist sampling rate. Consequently, the real-valued normalized path delays  $\tilde{\tau}_\ell$ ,  $\ell = 0, 1, \dots, L-1$  can be discretized as  $\mathcal{T}_\ell = \lfloor \varrho \tilde{\tau}_\ell \rfloor$  and take values from the set of the possible discrete path delays:

$$\mathcal{T}_\ell \in \{0, 1, 2, \dots, N_\tau - 1\}, \quad (3.22)$$

where  $N_\tau = \varrho L_{CP}$ ,  $L_{CP} = T_{CP}/T_s$  and  $T_{CP}$  is the duration of the CP. However,  $\varrho$  is usually chosen to be one in MP-based channel estimators. Similarly, the real-valued Doppler spread  $b$  can be discretized as  $\beta = \lfloor (b v_{\max}) / \Delta_v \rfloor$  and takes values from the set of the possible discrete Doppler rates:

$$\beta \in \{0, 1, 2, \dots, N_v - 1\}, \quad (3.23)$$

where  $N_v = (2 v_{\max}) / \Delta_v$ . Based on the associated discrete random channel tap positions  $\{\mathcal{T}_\ell\}_{\ell=0}^{L-1}$ , and Doppler rate  $\beta$ , the received signal in (3.20) can be rewritten as

$$\mathbf{z}_P = \sum_{\ell=0}^{L-1} \mathbf{a}_{r_\ell} h_\ell + \mathbf{V}_P, \quad (3.24)$$

where  $\mathbf{a}_{r_\ell}$  is the  $r_\ell^{th}$  column vector of the finer resolution matrix  $\mathbf{A}_P^{(\varrho)}$  whose columns correspond to the  $(\beta, \mathcal{T}_\ell)^{th}$  discrete multipath channel tap and Doppler rate positions, respectively. For a given  $r_\ell \Leftrightarrow (\beta, \mathcal{T}_\ell)$ , the  $k^{th}$  component of  $\mathbf{a}_{r_\ell}$  is determined from (3.21) as

$$\mathbf{a}_{r_\ell}[k] = A_P[k, \ell]|_{b=-v_{\max}+\beta\Delta_v, \tau_\ell=\mathcal{T}_\ell/Q}. \quad (3.25)$$

where  $\beta \in \{0, 1, 2, \dots, N_v - 1\}$  and  $\mathcal{T}_\ell \in \{0, 1, 2, \dots, N_\tau - 1\}$ . The total number of columns of  $\mathbf{A}_P^{(\ell)}$  is  $N_v N_\tau$  and they are labelled as  $r_\ell = 1, 2, \dots, N_v N_\tau$ . The conversion between  $r_\ell$  and  $(\beta, \mathcal{T}_\ell)$  can be easily obtained as:

$$r_\ell = \beta + N_v \mathcal{T}_\ell + 1,$$

$$\beta = r_\ell \bmod(N_v) - 1 \text{ and, } \mathcal{T}_\ell = \left\lfloor \frac{r_\ell}{N_v} \right\rfloor - 1.$$

As a first step in the MP algorithm, the column in the dictionary matrix,  $\mathbf{A}_P^{(\ell)} = [\mathbf{a}_0, \mathbf{a}_1, \dots, \mathbf{a}_{N_v N_\tau - 1}]$ , associated with the observation equation (3.24), that is best aligned with the residue vector  $\boldsymbol{\rho}_0 = \mathbf{Z}_P$  is found and denoted by  $\mathbf{a}_{r_1}$ . Then the projection of  $\boldsymbol{\rho}_0$  along this direction is removed from  $\boldsymbol{\rho}_0$  and the residual  $\boldsymbol{\rho}_1$  is obtained. The algorithm proceeds by sequentially choosing the column that is the best match until a termination criterion is met. At the  $\ell^{th}$  iteration, the index of the vector from  $\mathbf{A}_P^{(\ell)}$  most closely aligned with the residual vector  $\boldsymbol{\rho}_{\ell-1}$  is obtained as follows (Berger, Zhou, Preisig, & Willett, 2010):

$$r_\ell = \arg \max_j \frac{|\mathbf{a}_j^\dagger \boldsymbol{\rho}_{\ell-1}|^2}{\mathbf{a}_j^\dagger \mathbf{a}_j}, j = 1, 2, \dots, N_v N_\tau - 1, \quad (3.26)$$

$$j \notin \{r_1, r_2, \dots, r_{\ell-1}\},$$

and a coarse channel path amplitude estimate at  $r_\ell$  is

$$h_\ell = \frac{\mathbf{a}_{r_\ell}^\dagger \boldsymbol{\rho}_{\ell-1}}{\mathbf{a}_{r_\ell}^\dagger \mathbf{a}_{r_\ell}}, \quad (3.27)$$

from which the new residual vector is computed as  $\boldsymbol{\rho}_\ell = \boldsymbol{\rho}_{\ell-1} - h_\ell \mathbf{a}_{r_\ell}$ . The iteration is repeated until a specified number of channel taps,  $L$ , have been selected or the residual becomes sufficiently small, i.e.  $\|\boldsymbol{\rho}_\ell\| < \varepsilon$ .

### 3.3.3 Path Gains Estimation $\{h_\ell\}$

With the path delays and Doppler spread information, the channel path gains  $\{h_\ell\}_{\ell=0}^{L-1}$  can be estimated by the MAP technique in an optimal fashion. Using the reduced dimensional

observation model given by (3.24) to estimate the complex valued channel gains  $h_\ell$ . For notational simplicity, equation (3.24) can be re-written in the following form:

$$\mathbf{z} = \mathbf{y}\mathbf{h} + \mathbf{v}, \quad (3.28)$$

where  $\mathbf{z} \equiv \mathbf{z}_p$ ,  $\mathbf{y} \equiv [\mathbf{e}_0, \mathbf{e}_1, \dots, \mathbf{e}_{L-1}]$ ,  $\mathbf{e}_\ell \equiv \mathbf{a}_{r_\ell}$ ,  $\mathbf{h} = [h_0, h_1, \dots, h_{L-1}]^T$  and  $\mathbf{v} \equiv \mathbf{V}_p$ . Let the two notations  $s_\ell = \sigma_\ell^2$ ,  $\eta \equiv 1/\sigma_\ell^2$ , define the channel path gains are assumed to obey a Rician distribution in which  $h_\ell$ 's are complex Gaussian random variables with independent real and imaginary parts with mean  $\mu_\ell$  and the variance  $s_\ell$  and with Rician factor,  $\kappa_\ell = \mu_\ell^2/s_\ell$ , again assumed equal for each multipath channel. Consequently, the parametric form of the prior joint probability density function (pdf) of  $\mathbf{h}$  can expressed as

$$f(\mathbf{h}|\tilde{\boldsymbol{\mu}}, \tilde{\boldsymbol{s}}) = \prod_{\ell=0}^{L-1} \frac{1}{\pi \tilde{s}_\ell} \exp\left(-\frac{1}{\tilde{s}_\ell} |h_\ell - \tilde{\mu}_\ell|^2\right), \quad (3.29)$$

where  $\tilde{\mu}_\ell = \mu_\ell(1 + j)$ ,  $\tilde{s}_\ell = 2s_\ell$  and  $\tilde{\boldsymbol{\mu}} = [\tilde{\mu}_0, \tilde{\mu}_1, \dots, \tilde{\mu}_{L-1}]^T$ ,  $\tilde{\boldsymbol{s}} = [\tilde{s}_0, \tilde{s}_1, \dots, \tilde{s}_{L-1}]^T$  are vectors of  $2L$  parameters controlling the prior mean and variance of each channel coefficient  $h_\ell$ . For fixed values of the parameters governing the prior, the posterior density of the channel coefficients vector is complex Gaussian as follows:

$$p(\mathbf{h}|\tilde{\boldsymbol{\mu}}, \tilde{\boldsymbol{s}}) = CN(\boldsymbol{\mu}_h, \boldsymbol{\Sigma}_h), \quad (3.30)$$

with  $\boldsymbol{\mu}_h = \boldsymbol{\Sigma}_h(\eta \mathbf{y}^\dagger \mathbf{z} + \boldsymbol{\Gamma}^{-1} \tilde{\boldsymbol{\mu}})$  and  $\boldsymbol{\Sigma}_h = (\eta \mathbf{y}^\dagger \mathbf{y} + \boldsymbol{\Gamma}^{-1})^{-1}$ , where  $\boldsymbol{\Gamma} = \text{diag}(\tilde{\boldsymbol{s}})$ . Thus, from (3.30) the MAP estimator for  $\mathbf{h}$  is given by

$$\begin{aligned} \hat{\mathbf{h}}_{\text{MAP}} &= \arg \max_{\mathbf{h}} f(\mathbf{h}|\tilde{\boldsymbol{\mu}}, \tilde{\boldsymbol{s}})_{\boldsymbol{\mu}_h} \\ &= \left(\mathbf{y}^\dagger \mathbf{y} + \frac{1}{\eta} \boldsymbol{\Gamma}^{-1}\right)^{-1} \left(\mathbf{y}^\dagger \mathbf{z} + \frac{1}{\eta} \boldsymbol{\Gamma}^{-1} \tilde{\boldsymbol{\mu}}\right). \end{aligned} \quad (3.31)$$

The column vectors of  $\mathbf{y} \equiv A_p = [e_0, e_1, \dots, e_{L-1}]$  are approximately orthogonal. That is  $e_\ell^\dagger e_{\ell'} \approx 0$  for  $\ell \neq \ell'$  and  $\ell \neq \ell' \in \{0, 1, \dots, L-1\}$ . The column vector  $e_\ell$  of the matrix in (3.21) can be expressed as

$$e_\ell = [F_{p_1, p_1}(b_\ell) e^{-j2\pi p_1 \tilde{\tau}_\ell/N}, F_{p_2, p_2}(b_\ell) e^{-j2\pi p_2 \tilde{\tau}_\ell/N}, \dots, F_{p_P, p_P}(b_\ell) e^{-j2\pi p_P \tilde{\tau}_\ell/N}]^T$$

where

$$F_{p_k, p_k}(b_\ell) = \frac{\sin(\Theta_{p_k, p_k})}{N \sin\left(\frac{\Theta_{p_k, p_k}}{N}\right)} \exp\left(-j \frac{N-1}{N} \Theta_{p_k, p_k}\right) \times \exp(j2\pi(f_c b_\ell - \hat{v})T_{CP})$$

and  $\Theta_{p_k, p_k} = \pi(b_\ell p_k + (f_c b_\ell - \hat{v})T)$ .

It then follows from  $F_{p_k, p_k}(b_\ell)$  that

$$e_\ell^\dagger e_{\ell'} = \sum_{k=1}^P F_{p_k, p_k}(b_\ell) F_{p_k, p_k}^*(b_{\ell'}) \exp\left(-j \frac{2\pi p_k(\tilde{\tau}_\ell - \tilde{\tau}_{\ell'})}{N}\right).$$

Note that, the Doppler rates  $\{b_\ell\}$  are uniformly distributed within  $[-b_{max}, +b_{max}]$ , where  $b_{max} = v_{max}/c$ , being the maximum velocity standard deviation and  $c$  is the sound of speed. In practice, even in the presence of a severe Doppler spread,  $b_{max}$  is in the order of  $5 \times 10^{-4}$ . Hence,  $|b_\ell| \ll 1$  for  $\ell \in \{0, 1, \dots, L-1\}$ . On the other hand, assuming  $\hat{v}$ , the residual mean Doppler shift, is estimated almost perfectly, it follows that  $|f_c b_\ell - \hat{v}| \ll 1$ . Consequently, the term  $F_{p_k, p_k}(b_\ell) F_{p_k, p_k}^*(b_{\ell'})$  in  $e_\ell^\dagger e_{\ell'}$  can be replaced with unity that yields to an upper bound for the value of  $e_\ell^\dagger e_{\ell'}$ . Then  $e_\ell^\dagger e_{\ell'}$  takes the form

$$e_\ell^\dagger e_{\ell'} = \sum_{k=1}^P \exp\left(-j \frac{2\pi p_k(\tilde{\tau}_\ell - \tilde{\tau}_{\ell'})}{N}\right).$$

The real-valued, normalized path delays  $\tilde{\tau}_\ell$ 's in  $e_\ell^\dagger e_{\ell'}$  are estimated by the MP algorithm at equally spaced pilot positions  $p_1 = 0, p_2 = p_1 + \Delta, \dots, p_P = (P-1)\Delta$ , taking values from the set of possible discrete path delays,  $\{0, 1, \dots, L_{CP}\}$ , normalized to the sampling interval  $T_s$ . Hence for  $\ell \neq \ell'$ ,  $\tilde{\tau}_\ell - \tilde{\tau}_{\ell'} \approx m$ , where  $m \neq 0$  is an integer. Note also that  $P\Delta = N$ . Now substituting  $\tilde{\tau}_\ell - \tilde{\tau}_{\ell'} = m$  and  $p_k = (k-1)\Delta$  in  $e_\ell^\dagger e_{\ell'}$  and performing the resulting summation, for  $m \neq 0$ , the result can be shown as follows

$$\begin{aligned} e_\ell^\dagger e_{\ell'} &\approx \sum_{k=0}^{P-1} \exp\left(-j \frac{2\pi k m \Delta}{N}\right) \\ &= \frac{1 - e^{-j2\pi m P \Delta / N}}{1 - e^{-j2\pi m \Delta / N}} \\ &= \frac{1 - e^{-j2\pi m}}{1 - e^{-j2\pi m \Delta / N}} \end{aligned}$$

$$= 0.$$

Consequently,  $\mathbf{y}^\dagger \mathbf{y}$  is a banded matrix and can be approximated as  $\mathbf{y}^\dagger \mathbf{y} = \text{diag}(\|\mathbf{e}_0\|^2, \|\mathbf{e}_1\|^2, \dots, \|\mathbf{e}_{L-1}\|^2)$ , where  $\mathbf{e}_\ell$  is the  $\ell^{\text{th}}$  column vector of  $\mathbf{y}$ . Then, the matrix inversion in (3.31) can be computed easily as:

$$\left( \mathbf{y}^\dagger \mathbf{y} + \frac{\mathbf{1}}{\eta} \mathbf{\Gamma}^{-1} \right)^{-1} = \text{diag}(\lambda_0, \lambda_1, \dots, \lambda_{L-1}), \quad (3.32)$$

with  $\lambda_\ell = (\eta \|\mathbf{e}_\ell\|^2 + 1/\tilde{s}_\ell)^{-1}$ . However, for  $\ell = 0, 1, \dots, L-1$ , the unknown parameters  $\mu_\ell = \tilde{\mu}_\ell/(1+j)$  and  $s_\ell = \tilde{s}_\ell/2$ , representing the independent real and imaginary parts of the Rician distributed channel coefficients,  $h_\ell$ , can be estimated from (3.28) by marginalizing over  $\mathbf{h}$ , and then performing ML estimation. Details are given in the following subsection.

### 3.3.4 ML Estimation of the Prior Unknown Mean and Variance $\{\mu_\ell, s_\ell\}_\ell^{L-1}$

The reduced dimensional observation model given by (3.28) is used to obtain the ML estimates of the variance  $\mathbf{s} = [s_0, s_1, \dots, s_{L-1}]^T$  and the mean vector  $\boldsymbol{\mu} = [\mu_0, \mu_1, \dots, \mu_{L-1}]^T$  of  $\mathbf{h}$  as follows:

$$(\boldsymbol{\mu}_{\text{ML}}, \mathbf{S}_{\text{ML}}) = \arg \max_{\boldsymbol{\mu}, \mathbf{s}} \log p(\mathbf{z} | \boldsymbol{\mu}, \mathbf{s}), \quad (3.33)$$

In (3.33),  $p(\mathbf{z} | \boldsymbol{\mu}, \mathbf{s})$  can be evaluated by averaging it over  $\mathbf{h}$  as

$$p(\mathbf{z} | \boldsymbol{\mu}, \mathbf{s}) = \int_{\mathbf{h}} p(\mathbf{z} | \mathbf{h}) p(\mathbf{h} | \boldsymbol{\mu}, \mathbf{s}). \quad (3.34)$$

From (3.28) it follows that

$$p(\mathbf{z} | \mathbf{h}) \sim \exp\{-\eta \|\mathbf{z} - \mathbf{y}\mathbf{h}\|^2\}, \quad (3.35)$$

and  $p(\mathbf{h} | \boldsymbol{\mu}, \mathbf{s})$  is given by (3.29). Substituting (3.35) and (3.29) into (3.34) and defining  $\mathbf{y}_0 \equiv (\mathbf{1} + j) \mathbf{y}$ , the integral of (3.34) with respect to  $\mathbf{h}$  is computable and given by

$$p(\mathbf{z} | \mathbf{s}, \boldsymbol{\mu}) = \pi^{-P} \det(C_z^{-1}) \exp\{-(\mathbf{z} - \mathbf{y}_0 \boldsymbol{\mu})^\dagger C_z^{-1} (\mathbf{z} - \mathbf{y}_0 \boldsymbol{\mu})\}, \quad (3.36)$$

where  $C_z = \mathbf{y} \mathbf{A} \mathbf{y}^\dagger + (1/\eta) \mathbf{I}_P$  and  $\mathbf{A} = \text{diag}(2s_0, 2s_1, \dots, 2s_{L-1})$ . The loglikelihood of  $\boldsymbol{\mu}$  and  $\mathbf{s}$  can then be expressed as

$$\log p(\mathbf{z} | \boldsymbol{\mu}, \mathbf{s}) = (\mathbf{z} - \mathbf{y}_0 \boldsymbol{\mu})^\dagger C_z^{-1} (\mathbf{z} - \mathbf{y}_0 \boldsymbol{\mu}) + \log \det(C_z). \quad (3.37)$$

Then the ML estimate of  $\boldsymbol{\mu}$ . Can be found by minimizing (3.37). By taking the derivative of  $\log p(\mathbf{z}|\boldsymbol{\mu}, \mathbf{s})$  with respect to  $\boldsymbol{\mu}$  and setting the resulting gradient to zero, the following solution can be obtained:

$$\hat{\boldsymbol{\mu}}_{\text{ML}} = (\mathbf{y}_0^\dagger C_z^{-1} \mathbf{y}_0)^{-1} \mathcal{R}e\{\mathbf{y}_0^\dagger C_z^{-1} \mathbf{z}\}. \quad (3.38)$$

Using the matrix inversion lemma,  $C_z^{-1} \mathbf{z}$  can be expressed as

$$\begin{aligned} C_z^{-1} &= (\mathbf{y} \mathbf{A} \mathbf{y}^\dagger + (1/\eta) \mathbf{I}_P)^{-1} \\ &= \eta \mathbf{I}_P - \eta \mathbf{y} \left( \mathbf{y}^\dagger \mathbf{y} + \left(\frac{1}{\eta}\right) \mathbf{A} \right)^{-1} \mathbf{y}^\dagger. \end{aligned} \quad (3.39)$$

As mentioned earlier,  $\mathbf{y}^\dagger \mathbf{y}$  can be approximated as  $\mathbf{y}^\dagger \mathbf{y} = \text{diag}(\|\mathbf{e}_0\|^2, \|\mathbf{e}_1\|^2, \dots, \|\mathbf{e}_{L-1}\|^2)$ , where  $\mathbf{e}_\ell$  is the  $\ell^{\text{th}}$  column vector of  $\mathbf{y}$ . Then, (3.39) can be computed easily as:

$$C_z^{-1} = \eta \mathbf{I}_P - \eta \mathbf{y}^\dagger \boldsymbol{\Lambda} \mathbf{y}, \quad (3.40)$$

where  $\boldsymbol{\Lambda} = \text{diag}(\lambda_0, \lambda_1, \dots, \lambda_{L-1})$  with  $\lambda_\ell = (\|\mathbf{e}_\ell\|^2 + 1/(2\eta\tilde{s}_\ell))^{-1}$ .

On the right hand side of Eq. (3.38), the term  $(\mathbf{y}_0^\dagger C_z^{-1} \mathbf{y}_0)^{-1}$  can be expressed as follows

$$\begin{aligned} (\mathbf{y}_0^\dagger C_z^{-1} \mathbf{y}_0)^{-1} &= \left( (1+j)(1-j)(\mathbf{y}^\dagger C_z^{-1} \mathbf{y}) \right)^{-1} \\ &= \frac{1}{2} (\mathbf{y}^\dagger C_z^{-1} \mathbf{y})^{-1}. \end{aligned}$$

Substituting  $C_z^{-1} = (\mathbf{y} \mathbf{A} \mathbf{y}^\dagger + (1/\eta) \mathbf{I}_P)^{-1}$ , obtained in Eq. (3.39) and  $\mathbf{y}^\dagger \mathbf{y} = \text{diag}(\|\mathbf{e}_0\|^2, \|\mathbf{e}_1\|^2, \dots, \|\mathbf{e}_{L-1}\|^2)$ , into the above expression yields,

$$\begin{aligned} (\mathbf{y}_0^\dagger C_z^{-1} \mathbf{y}_0)^{-1} &= \frac{1}{2\eta} (\mathbf{y}^\dagger \mathbf{y} - \mathbf{y}^\dagger \mathbf{y} \mathbf{A} \mathbf{y}^\dagger \mathbf{y})^{-1} \\ &= \frac{1}{2\eta} (\text{diag}(\|\mathbf{e}_0\|^2, \|\mathbf{e}_1\|^2, \dots, \|\mathbf{e}_{L-1}\|^2) - \text{diag}(\|\mathbf{e}_0\|^4 \lambda_0, \|\mathbf{e}_1\|^4 \lambda_1, \dots, \|\mathbf{e}_{L-1}\|^4 \lambda_{L-1}))^{-1} \\ &= \frac{1}{2\eta} (\text{diag}((\|\mathbf{e}_0\|^2 - (1 - \lambda_0 \|\mathbf{e}_0\|^4))^{-1}, \dots, (\|\mathbf{e}_{L-1}\|^{L-1} - (1 - \lambda_{L-1} \|\mathbf{e}_{L-1}\|)^{-1})) \end{aligned}$$

On the other hand, the second term,  $\mathcal{R}e\{\mathbf{y}_0^\dagger C_z^{-1} \mathbf{z}\}$  in (3.38) can be expressed as

$$\begin{aligned} \mathcal{R}e\{\mathbf{y}_0^\dagger C_z^{-1} \mathbf{z}\} &= \eta \mathcal{R}e\{\mathbf{y}_0^\dagger (\mathbf{I}_P - \mathbf{y} \mathbf{A} \mathbf{y}^\dagger) \mathbf{z}\} \\ &= \eta \mathcal{R}e\{\mathbf{y}_0^\dagger \mathbf{I}_P - \mathbf{y}_0^\dagger \mathbf{y} \mathbf{A} \mathbf{y}^\dagger \mathbf{z}\} \\ &= \eta \mathcal{R}e\{\mathbf{y}_0^\dagger - \mathbf{y}^\dagger \mathbf{y} \mathbf{A} \mathbf{y}_0^\dagger \mathbf{z}\} \end{aligned}$$

$$\begin{aligned}
&= \eta \operatorname{Re}\{(\mathbf{I}_L - \mathbf{y}^\dagger \mathbf{y} \mathbf{A}) \mathbf{y}_0^\dagger \mathbf{z}\} \\
&= \eta \operatorname{diag}((1 - \|\mathbf{e}_0\|^2 \lambda_0), \dots, (1 - \|\mathbf{e}_{L-1}\|^2 \lambda_{L-1})) \operatorname{Re}\{\mathbf{y}_0^\dagger \mathbf{z}\}.
\end{aligned}$$

Note that in the last equation, the third equation from the above follows from the second equation due to the fact that  $\mathbf{y}_0 \triangleq (1 + j)\mathbf{y}$ . Inserting  $(\mathbf{y}_0^\dagger \mathbf{C}_z^{-1} \mathbf{y}_0)^{-1}$  and  $\operatorname{Re}\{\mathbf{y}_0^\dagger \mathbf{C}_z^{-1} \mathbf{z}\}$  in Eq (38), the final result can be expressed as

$$\hat{\boldsymbol{\mu}}_{\text{ML}} = \frac{1}{2} \operatorname{diag}(\|\mathbf{e}_0\|^{-2}, \|\mathbf{e}_1\|^{-2}, \dots, \|\mathbf{e}_{L-1}\|^{-2}) \operatorname{Re}\{\mathbf{y}_0^\dagger \mathbf{z}\}. \quad (3.41)$$

The ML variance estimate of  $\mathbf{s}$  is then found by maximizing the following objective function with respect to  $\mathbf{s}$ :

$$J(\hat{\boldsymbol{\mu}}_{\text{ML}}, \mathbf{s}) = \arg \max_{\mathbf{s}} \log p(\mathbf{z} | \hat{\boldsymbol{\mu}}_{\text{ML}}, \mathbf{s}). \quad (3.42)$$

Substituting (3.40) and (3.41) into (3.37), and discarding the terms independent of  $\mathbf{s}$ , (3.42) takes the form of,

$$J(\hat{\boldsymbol{\mu}}_{\text{ML}}, \mathbf{s}) = \sum_{\ell=0}^{L-1} \log \left( \|\mathbf{e}_\ell\|^2 s_\ell + \frac{1}{\eta} \right) - \eta \sum_{\ell=0}^{L-1} (|q_\ell|^2 \lambda_\ell - |\mathbf{t}|^2), \quad (3.43)$$

where  $\mathbf{t} \triangleq \mathbf{z} - \mathbf{y} \hat{\boldsymbol{\mu}}_{\text{ML}}$  and  $q_\ell$  is the  $\ell^{\text{th}}$  component of the vector  $\mathbf{q} = \mathbf{y}^\dagger \mathbf{t}$ .

Defining  $\mathbf{t} \triangleq \mathbf{z} - \mathbf{y}_0 \hat{\boldsymbol{\mu}}_{\text{ML}}$  and  $\mathbf{q} = \mathbf{y}_0^\dagger \mathbf{t}$ , Eq (3.37) can be expressed as

$$\log p(\mathbf{z} | \boldsymbol{\mu}, \mathbf{s}) = \mathbf{t}^\dagger \mathbf{C}_z^{-1} \mathbf{t} + \log \det(\mathbf{C}_z).$$

Substituting the expression of  $\mathbf{C}_z^{-1}$  given by Eq. (39) and  $\mathbf{C}_z = \mathbf{y} \mathbf{A} \mathbf{y}^\dagger + (1/\eta) \mathbf{I}_p$  into  $\log p(\mathbf{z} | \boldsymbol{\mu}, \mathbf{s})$ , consequently,

$$\begin{aligned}
\log p(\mathbf{z} | \boldsymbol{\mu}, \mathbf{s}) &= \eta \mathbf{t}^\dagger (\mathbf{I}_p - \mathbf{y} \mathbf{A} \mathbf{y}^\dagger) \mathbf{t} + \log \det(\mathbf{y} \mathbf{A} \mathbf{y}^\dagger + (1/\eta) \mathbf{I}_p). \\
&= \eta (\mathbf{t}^\dagger \mathbf{t} - \mathbf{q}^\dagger \mathbf{A} \mathbf{q}) + \log \det(\mathbf{y} \mathbf{A} \mathbf{y}^\dagger + (1/\eta) \mathbf{I}_p).
\end{aligned}$$

Using the matrix identity  $\det(\mathbf{y} \mathbf{A} \mathbf{y}^\dagger + (1/\eta) \mathbf{I}_p) = \eta^L$  and discarding the terms independent of  $\mathbf{s}$ ,  $\log p(\mathbf{z} | \boldsymbol{\mu}, \mathbf{s})$  can then be expressed as

$$\det \log p(\mathbf{z} | \boldsymbol{\mu}, \mathbf{s}) \approx \sum_{\ell=0}^{L-1} \log(2 \|\mathbf{e}_\ell\|^2 s_\ell + 1/\eta) - \eta \sum_{\ell=0}^{L-1} \log(|q_\ell|^2 \lambda_\ell - \|\mathbf{t}\|^2).$$

Taking derivative of  $\det \log p(\mathbf{z} | \boldsymbol{\mu}, \mathbf{s})$  with respect to  $s_\ell$ , equating it to zero and solving the resulting equation yields the ML estimation expressed as

$$\hat{\mathbf{s}}_{\text{ML}} = \max \left( \frac{|q_\ell|^2 \eta - \|\mathbf{e}_\ell\|^2}{2 \|\mathbf{e}_\ell\|^4 \eta} \right)^+, \quad (3.44)$$

where  $[x]^+ = \max(0, x)$ . Finally a normalization is performed on the optimal mean and variance estimates so as to satisfy the following:



$$\sum_{\ell=0}^{L-1} \widehat{\Omega}_{\ell}^{(nor)} = \sum_{\ell=0}^{L-1} (2\hat{\mu}_{\ell,ML}^{2(nor)} + 2\hat{s}_{\ell,ML}^{2(nor)}) = 1, \quad (3.45)$$

where for  $\ell = 0, 1, \dots, L-1$ ,  $\hat{\mu}_{\ell,ML}$ ,  $\hat{s}_{\ell,ML}$ , and  $\widehat{\Omega}_{\ell}^{(nor)}$  are normalized versions of  $\hat{\mu}_{\ell,ML}$ ,  $\hat{s}_{\ell,ML}$ , and  $\widehat{\Omega}_{\ell} = 2\hat{\mu}_{\ell,ML} + 2\hat{s}_{\ell,ML}$ , respectively. Also,  $\kappa_{\ell} = \hat{\mu}_{\ell,ML}^{2(nor)} / \hat{s}_{\ell,ML}^{2(nor)}$ , where  $\kappa_{\ell}$  is the Rician  $\kappa$ -factor for the  $\ell^{th}$  tap of the channel. The normalized  $\widehat{\Omega}_{\ell}^{(nor)}$  is determined by means of  $\hat{\mu}_{\ell,ML}^{(nor)}$  and  $\hat{s}_{\ell,ML}^{(nor)}$  as

$$\widehat{\Omega}_{\ell}^{(nor)} = \frac{\widehat{\Omega}_{\ell}}{\sum_{m=0}^{L-1} \widehat{\Omega}_m}, \quad \ell = 0, 1, \dots, L-1,$$

from which the required normalized ML estimates of mean and variance are obtained respectively as:

$$\hat{s}_{\ell,ML}^{(nor)} = \frac{\widehat{\Omega}_{\ell}^{(nor)}}{2(1+\kappa_{\ell})}, \quad (3.46)$$

$$\hat{\mu}_{\ell,ML}^{(nor)} = \sqrt{\frac{\kappa_{\ell} \widehat{\Omega}_{\ell}^{(nor)}}{2(1+\kappa_{\ell})}}, \quad (3.47)$$

### 3.4 Equalization and data Detection

The final equalization and data detection steps at the receiver based on the received signal model in (3.18) is discussed in this subsection. Supposing  $\mathbf{P}$  known data symbols (pilots) in each OFDM symbol are evenly inserted into the  $\mathbf{K}$  subcarriers. Let  $\mathcal{P} = \{p_1, p_2, \dots, p_P\}$  denote the set containing the pilot positions and  $d_P(q)$ ,  $q \in \mathcal{P}$  denote a pilot symbol  $\mathbf{d} = [d_0, d_1, \dots, d_{K-1}]^T$  (3.18) is a superposition of the pilot vector,  $\mathbf{d}_P$ , and the vector of the unknown data symbols,  $\mathbf{d}_D$ , as  $\mathbf{d} = \mathbf{d}_P + \mathbf{d}_D$ .

However, the vectors  $\mathbf{d}_P, \mathbf{d}_D \in C^K$  contain nonzero components only at the pilot positions  $p_i$ ,  $i = 1, 2, \dots$ , and at the data positions  $\bar{\mathcal{P}}$ , respectively. Consequently, (3.18) can be expressed as

$$\begin{aligned} \mathbf{Z}_P &\triangleq \mathbf{Z} - \mathbf{G} \mathbf{d}_P \\ &= \mathbf{G} \mathbf{d}_D + \mathbf{V}. \end{aligned} \quad (3.48)$$

Then, the equalized soft data symbols  $\tilde{\mathbf{d}}_D$  are recovered at the output of a linear minimum mean-square error (LMMSE) equalizer as

$$\tilde{\mathbf{d}}_D = \mathbf{G}^\dagger (\mathbf{G} \mathbf{G}^\dagger + \gamma^{-1} \mathbf{I}_K)^{-1} \mathbf{Z}_P, \quad (3.49)$$

where is the signal-to-noise ratio (SNR). The  $[k, q]^{th}$  element of  $\mathbf{G}$  is computed from (3.15), (3.16) and (3.18) by replacing the channel estimates  $\{h_\ell, (b, \tilde{\tau}_\ell)\}_\ell^{L-1}$ , obtained at the channel estimation stage. However, although the MMSE equalizer outperforms other linear equalizers, the matrix inversion in (3.49) requires  $O(K^3)$  flops which represents a significant burden when  $K$  is large. However, as already documented in (Berger, Zhou, Preisig, & Willett, 2010), the UWA channels produce nearly-banded channel matrices  $\mathbf{G}$  and this property can be exploited to reduce the complexity substantially by means of the factorization of Hermitian banded matrices (Rugini, Banelli, & Leus, 2005). Finally, the soft equalized data symbols are mapped onto M-ary quadrature amplitude modulation (QAM) or phase-shift keying (PSK) symbols by an ML detection technique. The final channel estimation, equalization and detection algorithm is summarized in Fig.3.1.

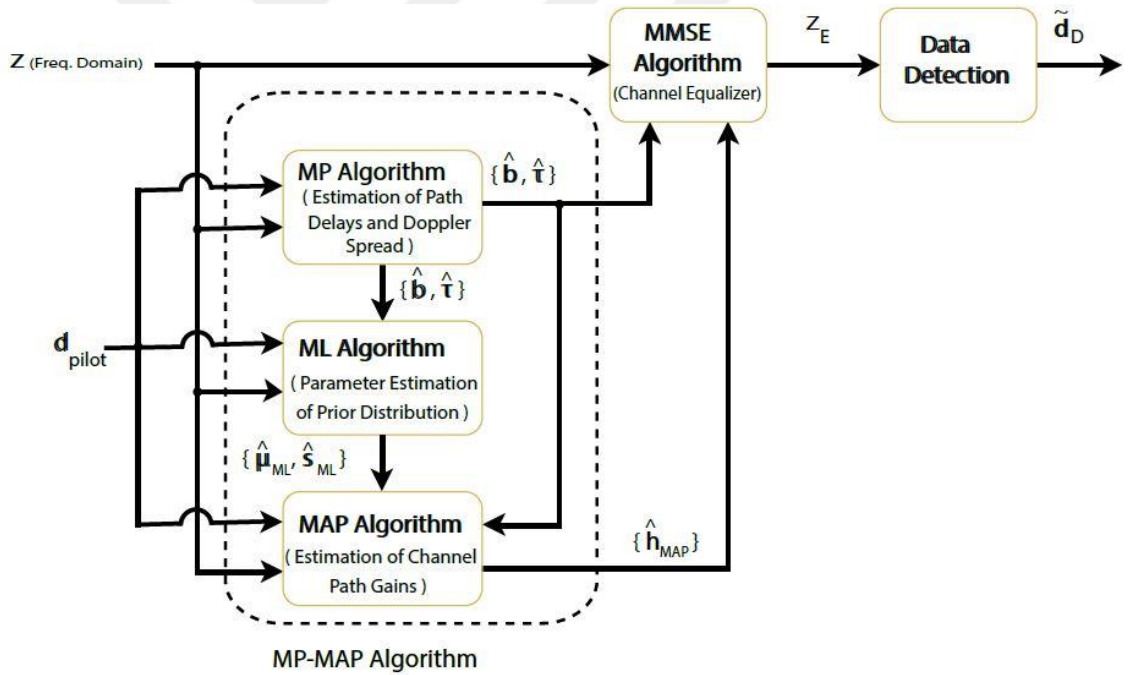


Figure 3.1 Block diagram of the MP-MAP channel estimation and equalization algorithm.

### 3.5 Computation Complexity

The computational complexity of the proposed algorithm is presented in Table-3.1. However, Doppler spread, path delays, and path amplitude estimates, in (3.26) and (3.27),

obtained by the MP algorithm require approximately  $(P+1)N_vN_\tau$  complex multiplications (CMs) and  $PLN_vN_\tau$  complex additions (CAs). Also, the computational complexity of the parameter estimates of the associated prior distribution of the channel gains,  $\hat{\mu}_{\ell,ML}$  and  $\hat{s}_{\ell,ML}$ , can be obtained as follows. In (3.41),  $\text{diag}(\|\mathbf{e}_0\|^{-2}, \|\mathbf{e}_1\|^{-2}, \dots, \|\mathbf{e}_{L-1}\|^{-2})$  requires  $N(L-1)$  CMs and  $(N-1)$  CAs. Similarly, computation of  $\Re\{\mathbf{y}_0^\dagger \mathbf{z}\}$  requires  $LN$  CMs and  $L(N-1)$  CAs. Consequently, total computations for  $\hat{\mu}_{\ell,ML}$  require  $3NL$  CMs. Similarly, the estimates of  $\hat{s}_{\ell,ML}$  in (3.44) require  $6L$  CM and  $L$  CA. On the other hand, to implement the MAP algorithm for estimation of the complex channel path gains in (3.31), it can be easily checked that it requires  $L(N+4)$  CMs and  $N(L+1)$  CAs.

Table 3.1 Computational complexity details

<b>Prior Distribution Parameters Estimation</b>			
<b>Eq. No</b>	<b>Variable</b>	<b>CMs</b>	<b>CAs</b>
(3.46)	$\hat{s}_{\ell,ML}$	$\approx 2L(N-1)$	$\approx 7L$
(3.47)	$\hat{\mu}_{\ell,ML}$	$\approx 2NL$	$\approx 2NL$
<b>MP-MAP Estimation Algorithm</b>			
(3.26), (3.27)	$r_\ell = (b, \tilde{\tau}_\ell)$	$\approx (P+1)N_vN_\tau$	$PLN_vN_\tau$
(3.31), (3.32)	$\hat{h}_{\ell,ML}$	$\approx NL + 4L$	$L$
<b>Equalization Algorithm</b>			
(3.49)	$\mathbf{G}^\dagger(\mathbf{G}\mathbf{G}^\dagger + \boldsymbol{\gamma}^{-1}\mathbf{I}_K)$	$\approx 3N^2(L + \Delta + 2)NL$	$\approx 2N^2(L + \Delta + 2) + N(L - 1)$

In computation of the equalizer output,  $\tilde{\mathbf{d}}_D$  in (3.49), the channel matrix  $\mathbf{G}$  and the Hermitian matrix  $\mathbf{G}^\dagger(\mathbf{G}\mathbf{G}^\dagger + \boldsymbol{\gamma}^{-1}\mathbf{I}_K)$  can be approximated as banded matrices whose total number of diagonal and sub-diagonals is  $\Delta$ . This property results in a substantial reduction of the computational complexity. Namely, the computation of  $\tilde{\mathbf{d}}_D$  requires approximately  $3N^2(L + \Delta + 2)NL$  CMs and  $2N^2(L + \Delta + 2) + N(L - 1)$  CAs. As a result, it follows from Table-3.1 that the total computational complexity per iteration of

the MP-MAP channel estimation and equalization algorithms is approximately  $2NL + 2L(N-1) + (P+1)LN_vN_\tau + NL + 4L + 3N^2(L + \Delta + 2) + NL$  CMs and  $2LN + 7L + PLN_vN_\tau + L + 2N^2(L + \Delta + 2) + N(L - 1)$  CAs. Consequently the complexity of the algorithm is on the order of  $O(NL)$  per OFDM subcarrier.

### 3.6 Computer Simulations with BELLHOP Simulated Channels in Sapanca Lake

In this subsection, the computer simulation results are presented to assess the performance of OFDMbased communication systems in UWA channels with the proposed channel estimation algorithm. The performance of the proposed algorithm is investigated over Sapanca Lake in Turkey, where the channels for the simulation part are generated by the BELLHOP-MATLAB wrapper acoustic toolbox (Kuai, Sun, & Cheng, 2016), which precisely reflects the characteristics of geographical location based on environmental factors such as sound speed profile and morphology of the lake bottom. Sapanca Lake is located at a latitude and longitude of 40.7163 and 30.2628, respectively. The lake has fresh water, and the dimensions of the lake are approximately 16-kilometres long, 5-kilometres wide, and the deepest point of the lake is about 53-metres (Fig 3.2).



Figure 3.2 Source and destination stations in Sapanca Lake

The source and destination are located 5 km apart from each other and the corresponding transmitter and receiver are placed at a depth of 50 meters.

Simulation parameters are summarized in Table-3.2. For the given environment, BELLHOP generates a variety of outputs such as the arrival time-series, the amplitudes and travel times associated with each echo. This yields the deterministic raw CIR which is then normalized and augmented by introducing Rician fading. Using the ray tracing

technique implemented by BELLHOP, Fig 3.2 shows the direct path and the reflected paths of the acoustic waves with significant power at the receiver (non-zero paths) between the source and destination, which enables us to compute the channel Rician factor.

However, as explained in (Llor & Malimbres, 2013), in detail, the Rician factor is calculated by applying a repetitive computation using BELLHOP for a set of varying environmental conditions (surface height, wave activity, small node displacements around nominal locations, etc.), an ensemble of transmission losses can be compiled for a given deployment information (water depth, salinity, operational frequency range) and later used to infer the statistical model parameters, including the fading distribution and the Rician  $\kappa$  – factor. While it is possible, in principle, to run a deterministic propagation model for a large number of different surface conditions, the underlying computational demands are high. Hence, the statistical prediction model (SPM) is adopted in (Llor & Malimbres, 2013), to facilitate the BELLHOP in the presence of channel fading for the Sapanca Lake simulations.

For the given SSP of Sapanca Lakes, the SMP is implemented by varying the parameters (wave height and wave lengths) related to the surface wave activity. Also, the stations are moved slowly in a random way at the source and receivers ends in vertical and horizontal

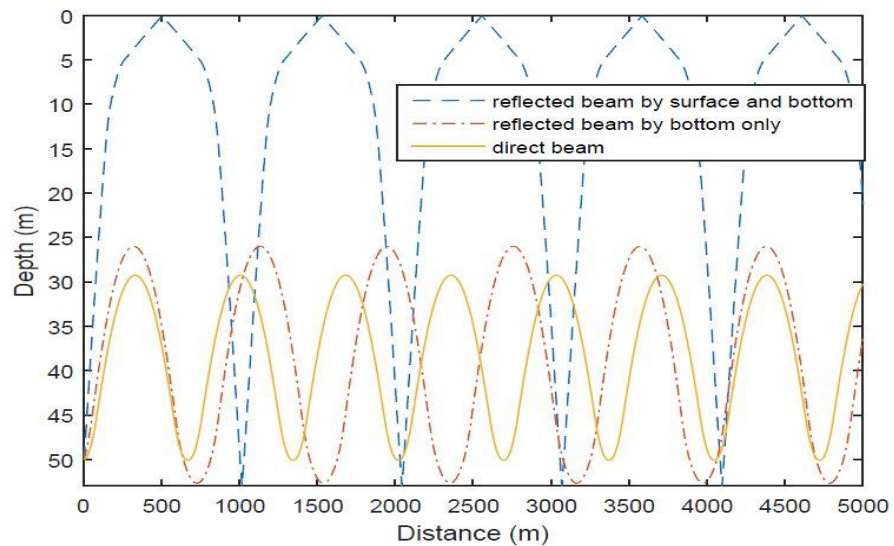


Figure 3.3 Ray tracing for a range of 5km

directions from their nominal positions. However, the surface wave height of Sapanca Lake was taken between 0.5 m -1 m (in steps 7.5 cm) and surface wave length between

25m-50m (in steps 1m). The probability density function estimated by the SMP was quite fitted in a Rician distribution with a Rician factor  $\kappa$  – factor  $\kappa_\rho \approx 10$ , for all channel paths, and consequently, used throughout the computer simulations. The proposed environmental profile, hypothesizes that the bottom type of Sapanca Lake is flat. However, a slight Doppler effect would arise due to the semi-steady state of the water motion in the lake. In order to get the sound speed for Sapanca Lake, Medwin’s formula (2.3) is used. The water temperature have been under measurement along the years (2000-2007) (Akcaakan, Koker, Gurevin, & Albay, 2014), where the average water temperature of Sapanca lake is around (16.0°), with salinity 0.5 ppt. Using these two values along the depths 0-53 m, an SSP is generated for the proposed Sapanca Lake. Fig 3.4 shows the sound speed profile of Sapanca Lake obtained by BELLHOP.

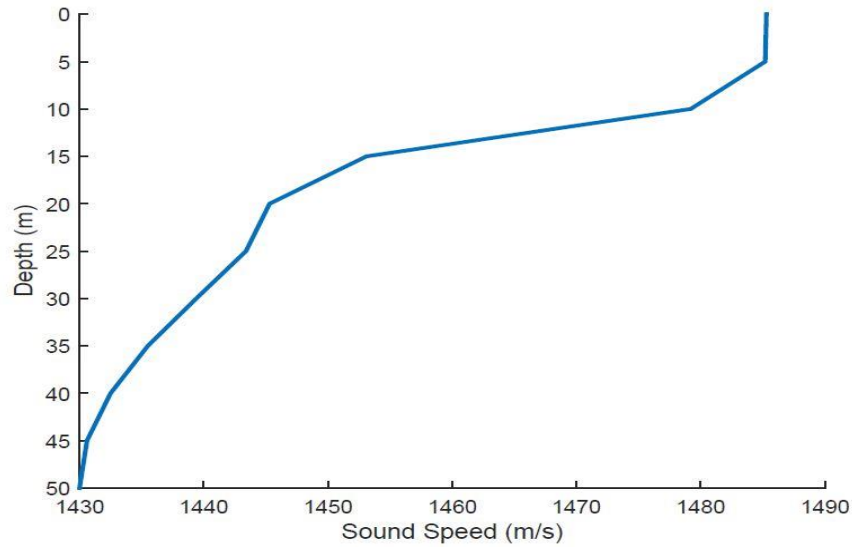


Figure 3.4 Sound speed profile for Sapanca Lake

Based on the carrier frequency,  $f_c$ , and the sound speed profile (Fig. 3.4), a raw deterministic sparse CIR is generated having a specific number of taps between the transmitter and the receiver. The initial CIR (called the “raw CIR by the BELLHOP) is obtained directly from BELLHOP software as shown in Fig. 3.5 (a), using the information as input, about the carrier frequency, SSP, the aperture of the transmit and receive antennas, their positions located in the lake and the communication range. The CIR, showing in Fig. 3.5 (b) with reduced number of effective taps,  $\mathcal{L}$ , is obtained after performing a clustering process on the taps in Fig. 3.5 (a) as follows. If the delay between two consecutive paths is smaller than  $1/BW$ , then the two paths are considered to be

merged into one path where the power of this path is determined by the summation of powers of the two corresponding paths. However, since the proposed communication range is 5 km and the average sound speed in the proposed underwater region is around 1.455km/s, the acoustical waves are expected to be received at the receiver with a delay about 3.43 s that can be seen in Fig. 3.5 (a) and Fig. 3.5 (b). In order to obtain the taps with only significant powers, a thresholding process is carried out on the CIR obtained in Fig. 3.5 (b), following the clustering process.

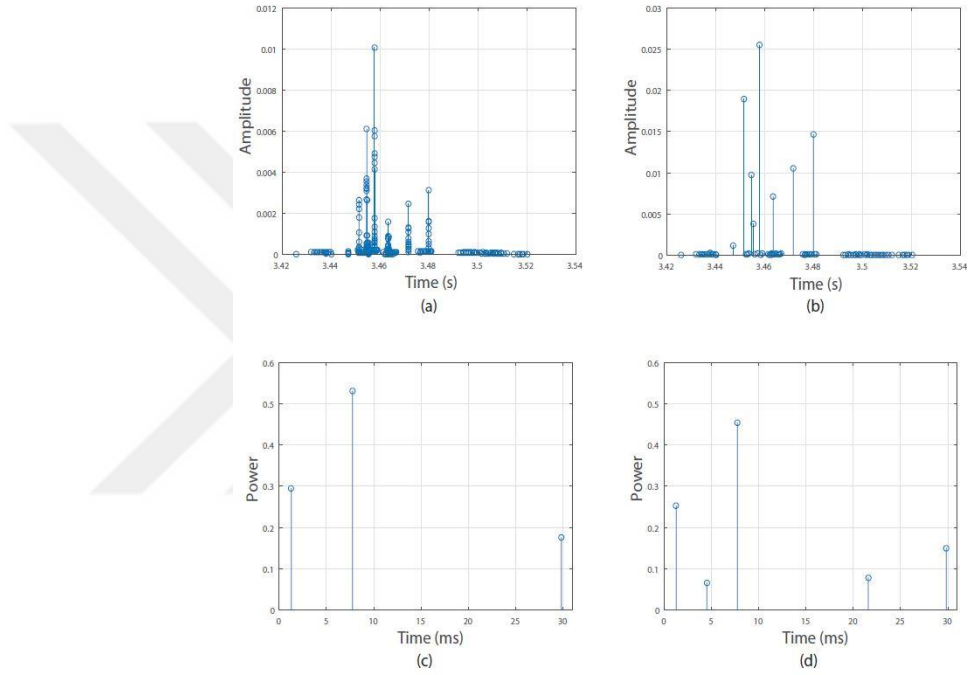


Figure 3.5 CIR for a range of 5km. (a) Original CIR with 607 paths; (b) Clustered paths with 79 clusters; (c)  $L = 3$ , delay spread = 28.5383 ms (normalized); (d)  $L = 5$ , delay spread = 28.5383 ms (normalized).

That is, only the channel taps gains that are greater than  $0.08 \sum_{l=0}^L |h_l|$ , and  $0.04 \sum_{l=0}^L |h_l|$ , are considered, as shown in Fig. 3.5 (c) and 5 (d), resulting in 3-paths and 5-paths sparse channel, respectively, with a delay spread of about 28 ms. The proposed simulations for the proposed algorithm include average mean square error and symbol error rate versus signal to noise ratio in the presence of (BPSK, QPSK, and 16QAM) signaling, different oversampling factor [2, 4, 8, 16], different residual Doppler shift [ $10^{-2}$ ,  $10^{-3}$ ,  $10^{-4}$ ,  $10^{-4}$ ], and different pilot spacing values [2, 4, 8] considering the proposed MP-MAP approach and comparing it to MP alone.

Considering a comb-type pilot structure with equally spaced pilot subcarriers and measure the performance of the system in terms of the frequency-domain mean square error (MSE) of the proposed channel estimator and the corresponding symbol error rate (SER). The sparse path delays and the Doppler shift are estimated by a conventional MP algorithm first. The estimates of the complex-valued channel gains are then obtained by the proposed MP-MAP algorithm.

Table 3.2 Channel and simulation parameters for Sapanca Lake

Variable	Value
Carrier frequency ( $f_c$ )	16 kHz
Channel bandwidth ( $BW$ )	4 kHz
Number of subcarriers ( $K$ )	512
OFDM symbol duration ( $T$ )	128 ms
Subcarrier spacing ( $\Delta f := 1/T$ )	7.81 Hz
Cyclic prefix duration ( $T_{CP}$ )	30 ms
Model parameter of the ambient noise ( $f_0 T_s$ )	0.05
Maximum Doppler rate ( $b_{max}$ )	$10^{-3}, 5 \times 10^{-4}, 10^{-4}$
Doppler spread resolution ( $\Delta_v$ )	$10^{-3}$ Hz
Channel Rician factor ( $\kappa_\ell$ )	10
Modulation formats	BPSK, QPSK, 16QAM
Pilot spacing ( $\Delta_p$ )	2, 4, 8
Oversampling factor ( $\varrho$ )	2, 4, 8, 16

In order to get statistically accurate results, the number of Monte Carlo runs is set as a function of signal-to-noise ratio values. the number of Monte Carlo runs increases according to  $rpt = step * (1:length(SNR\_dB))$ , so that, the more Monte Carlo runs,  $rpt$ , increases as SNR gets larger. The the step size parameter,  $step$ , is adjusted to 250, which was more than sufficient to obtain estimation errors up to  $10^{-5}$  with sufficient accuracy.

Figs. 3.6 and 3.7 show the MSE and SER performance curves of the MP and MP-MAP algorithm, corresponding to the UWA channel whose CIR is given by Fig. 3.5, for binary phase shift-keying (BPSK), quadrature phase shift-keying (QPSK) and 16-ary quadrature amplitude modulation (16QAM) signaling formats as a function of SNR in the presence of extreme Doppler spread. During simulations, the pilot spacing, Doppler spread and the resolution factor are chosen as  $\Delta_p = 8$ ;  $b_{max} = 10^{-3}$  and  $\varrho = 8$ , respectively. However,



$b_{max} = 10^{-3}$  represents a severe Doppler spread for UWA channels, corresponding to a maximum speed of  $v_{max} = cb_{max} = 1.5$  m/s for a speed of sound  $c = 1500$  m/s.

As seen from Figs. 3.6 and 3.7, the MP-MAP algorithm, having excellent channel estimation and symbol error rate performance, uniformly outperforms the MP estimator. For instance, within the 25-30 dB SNR region, the MSE and SER of the MP-MAP algorithm are about 10 dB and 4.5 dB better than those of the MP algorithm, respectively. This is mainly due to the fact that the MP-MAP algorithm makes use of the prior information of the Rician distributed channel gains very effectively.

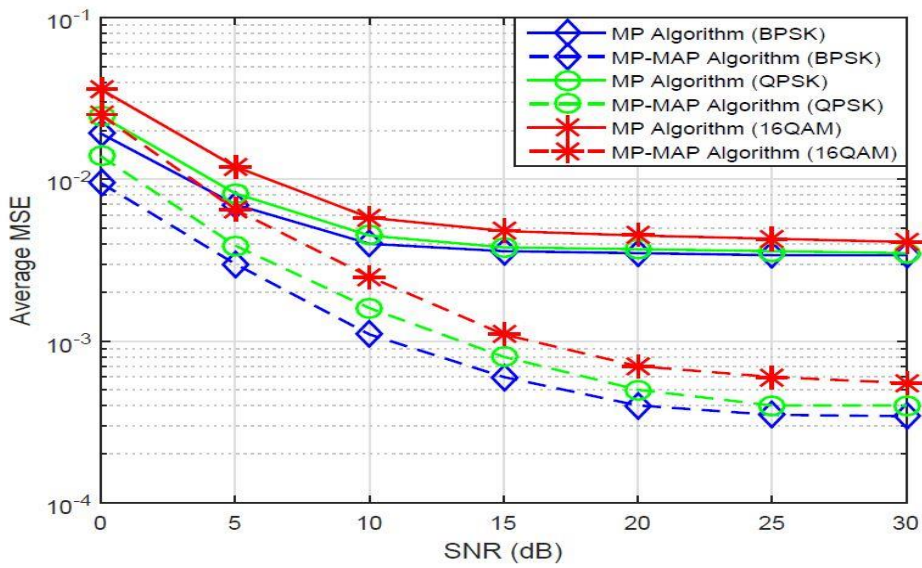


Figure 3.6 MSE vs. SNR performance comparisons of the MP-MAP and MP algorithms for different constellations:  $\rho = 8, b_{max} = 10^{-3}, \Delta_p = 4$ .

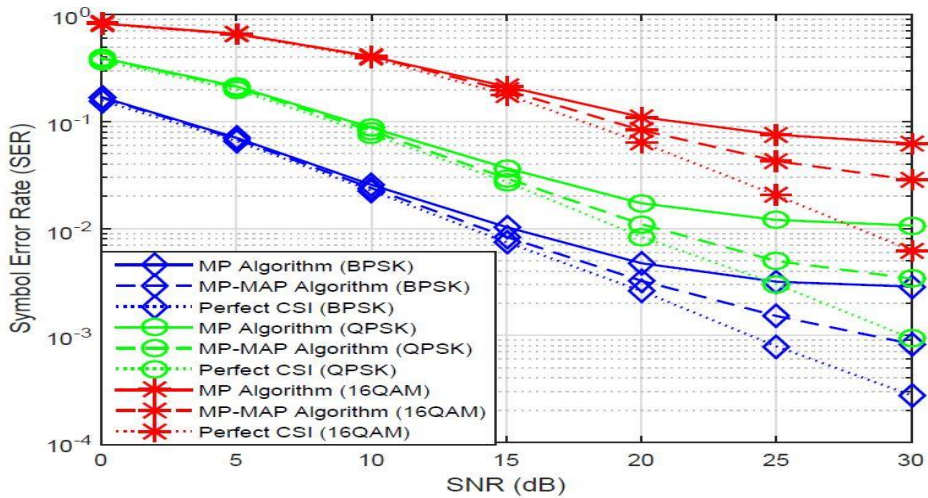


Figure 3.7 SER vs. SNR performance comparisons of the MP-MAP and MP algorithms for different constellations:  $\rho = 8, b_{max} = 10^{-3}, \Delta_p = 4$ .

In Figs. 3.8 and 3.9, the MSE and SER performances of the MP-MAP algorithm are shown as functions of SNR for different values of the oversampling factor,  $\rho = 2; 4; 8; 16$ , for maximum Doppler shift  $10^{-3}$ , oversampling factor  $\Delta_p = 4$  and 16QAM signaling. It can be seen from these figures that an oversampling factor of  $\rho = 8$  would be sufficient to obtain the best sparse channel estimation performance of the proposed MP-MAP algorithm. However, another investigation is performed on the proposed approach with respect to the effect of the Doppler spread on the MSE and SER performances of the system with oversampling factor  $\rho = 8$ , pilot spacing  $\Delta_p = 4$  and 16QAM signaling.

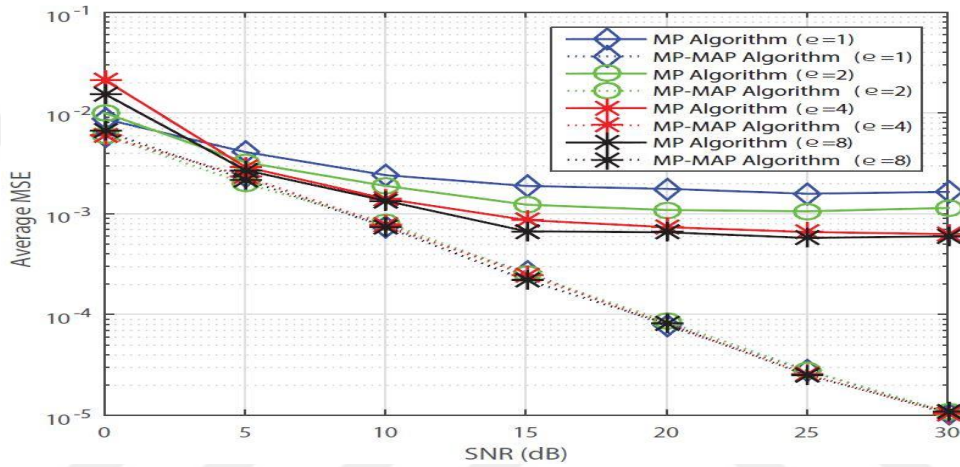


Figure 3.8 MSE vs. SNR performance of the MP-MAP algorithm for different resolution factors:  $b_{max} = 10^{-3}$ ,  $\Delta_p = 4$ , 16QAM signaling.

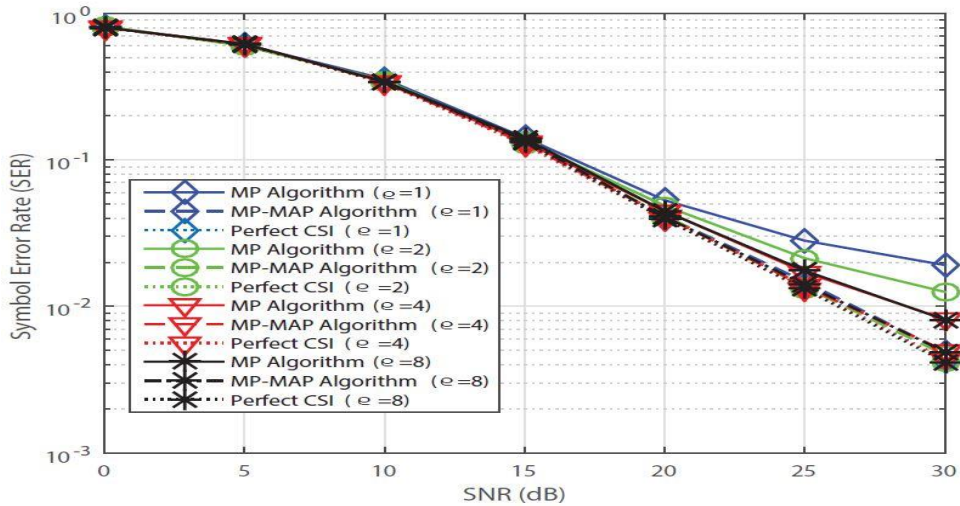


Figure 3.9 SER vs. SNR performance of the MP-MAP algorithm for different resolution factors:  $b_{max} = 10^{-3}$ ,  $\Delta_p = 4$ , 16QAM signaling.

Figs. 3.10 and 3.11 show that the proposed MP-MAP algorithm is quite robust to Doppler shifts up to  $b_{max} = 10^{-3}$  beyond which can be considered as severe Doppler effects.

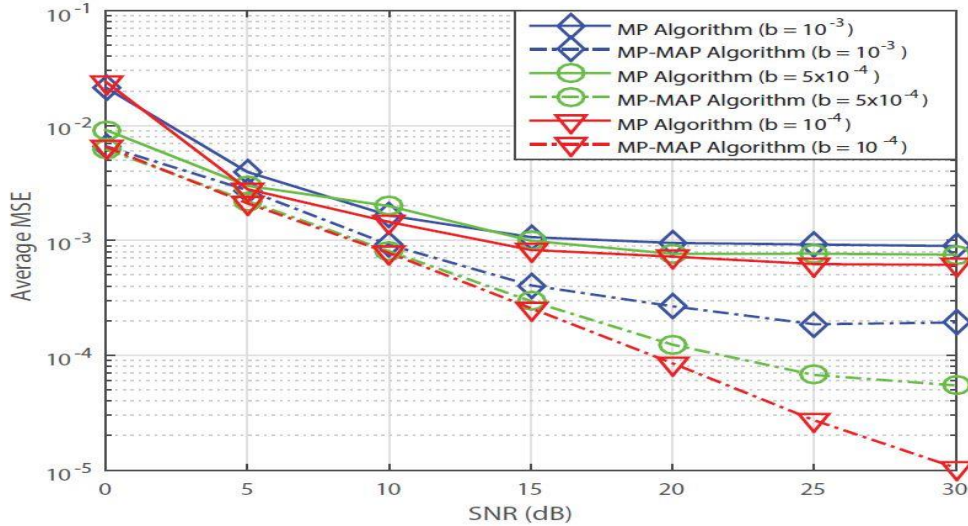


Figure 3.10 MSE vs. SNR performance of the MP-MAP algorithm for different Doppler rates:  $\rho = 8, \Delta_p = 4$ , 16QAM signaling.

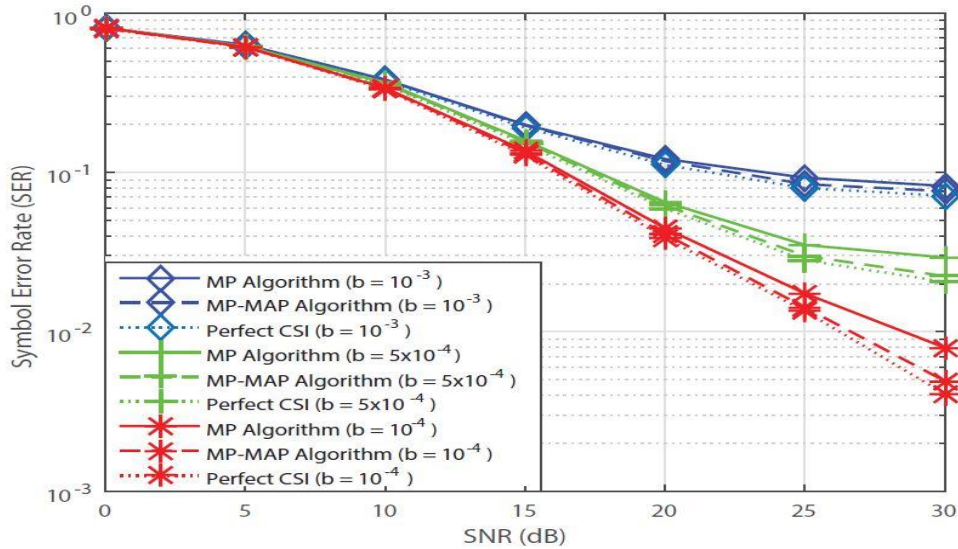


Figure 3.11 SER vs. SNR performance of the MP-MAP algorithm for different Doppler rates:  $\rho = 8, \Delta_p = 4$ , 16QAM signaling.

The effects of different pilot spacings ( $\Delta_p = 2, 4, 8$ ) on the MSE and SER performances are also investigated as functions of SNR in Figs 3.12 and 3.13. The parameters are chosen as  $\rho = 16$  and  $b_{max} = 10^{-3}$  with 16QAM signaling. It can be seen from these

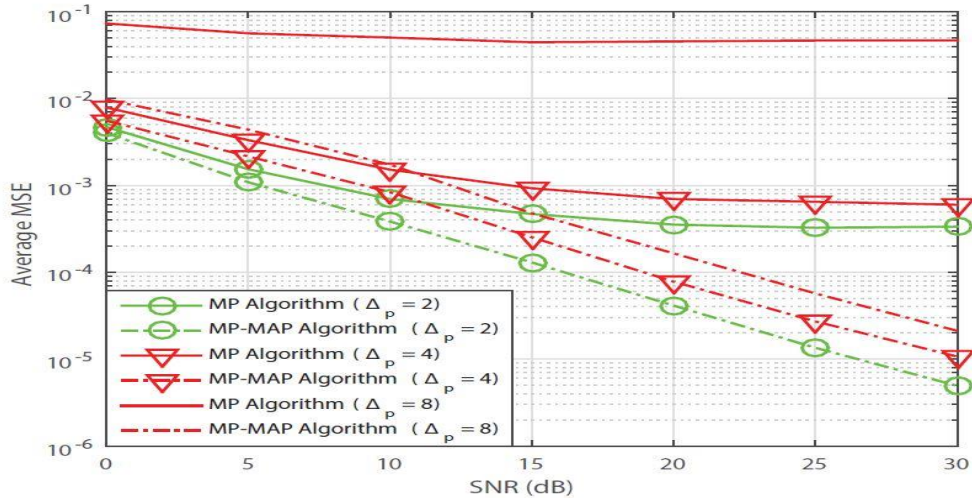


Figure 3.12 MSE vs. SNR performance of the MP-MAP algorithm for different pilot spacings:  $\rho = 16, b_{max} = 10^{-3}$ , 16QAM signaling.

curves that the channel estimation algorithm can tolerate a pilot spacing of  $\Delta_p=4$  sufficiently to handle the maximum Doppler rates around  $b_{max}=10^{-3}$ . The SER performance degrades rapidly as the pilot spacing increases beyond that. In addition, it can be seen in Fig. 3.13 that the proposed MP-MAP algorithm achieves almost the same in the SER for  $\Delta_p=2$  and  $\Delta_p=4$  for the given severe Doppler shift. Fig. 3.13 figure gives an important insight for the pilot design regarding system bandwidth usage and the complexity in the calculations in the oversampling matrix.

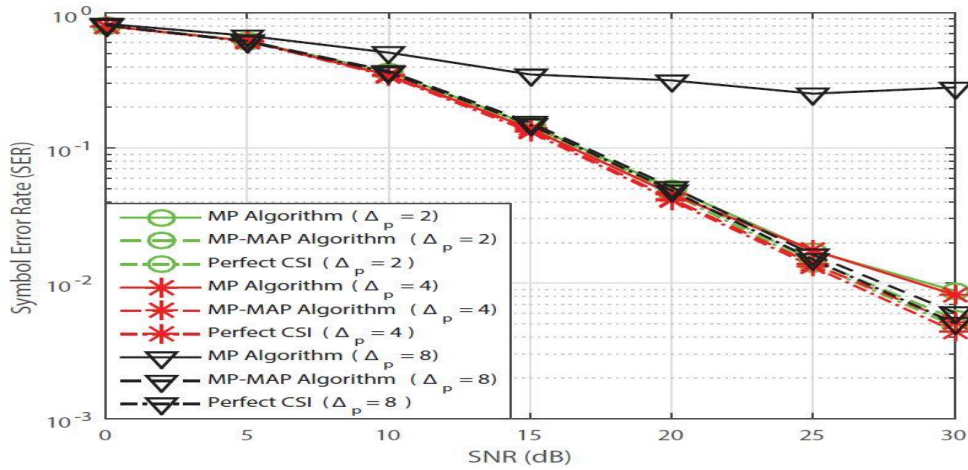


Figure 3.13 SER vs. SNR performance of the MP-MAP algorithm for different pilot spacings:  $\rho = 16, b_{max} = 10^{-3}$ , 16QAM signaling.

### 3.7 OMP-MAP Estimation

In this section, an extension of the proposed algorithm is performed. The aforementioned proposed approach considers matching pursuit algorithm for Doppler and delays

estimation and MAP probability estimate for path gains' estimation, where the channel multipaths were assumed to experience the same Doppler scale factor and hence there is no Doppler "spread" but just an uncompensated residual Doppler. In this section, considering white noise, another member of the matching pursuit family called orthogonal matching pursuit (OMP) is proposed for Doppler and delays estimation. In addition, in this section, the multipath channel is assumed to have different Doppler scaling factors (non-uniform Doppler shifts) exist in the Doppler-compensated received signal.

### 3.7.1 OMP-MAP Algorithm

The Doppler scaling factor  $b$ , in this section, is considered to be different for every path  $\ell \in \{0, 1, \dots, L - 1\}$ . Consequently, define,  $b_\ell$ , as the Doppler scaling factor of the  $\ell^{th}$  path. However, the MP-MAP formulas, in this section, are kept the same, except that OMP algorithm is used instead for Doppler and delay estimation, and hence, OMP-MAP is presented. The OMP algorithm can be found in (Yu et al., 2015), where the OMP-MAP algorithm is shown in Fig. 3.14.

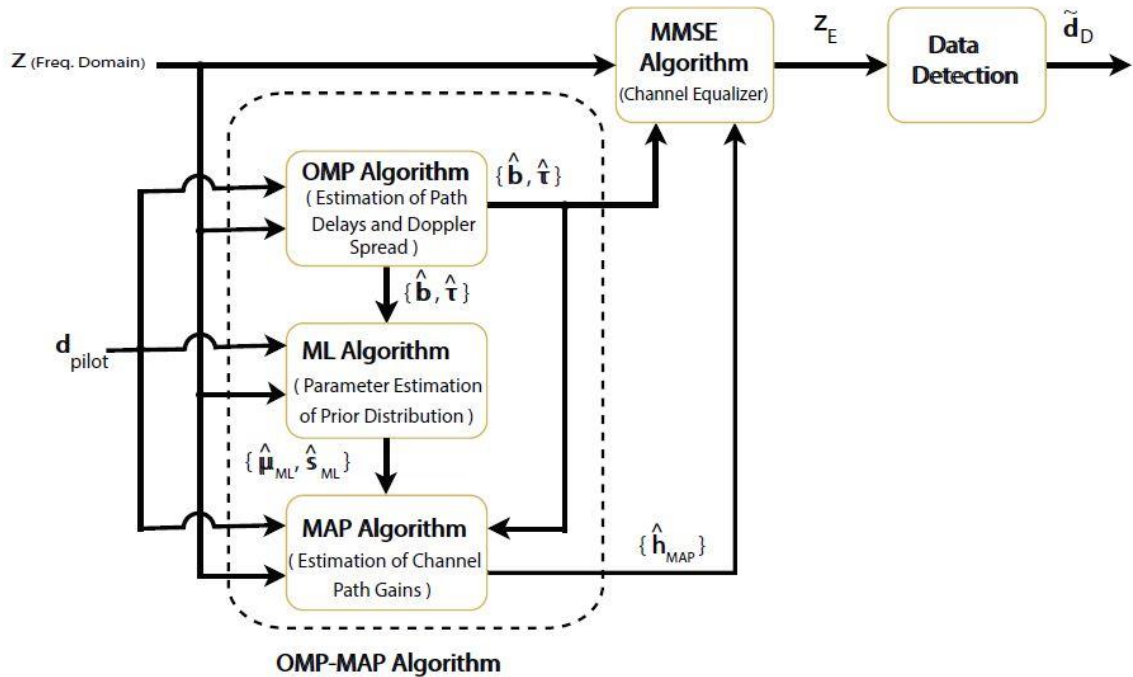


Figure 3.14 Block diagram of the OMP-MAP channel estimation and equalization algorithm

However, since the Doppler scale is considered to be different for each path, adjustments have to be carried out on part of the formulas presented earlier in this chapter, mainly in the system and channel model. Equations (3.2) and (3.3) which show the time-varying continuous-time multipath UWA channel impulse response in passband and baseband, respectively, are rewritten accordingly to meet the non-uniform Doppler scaling, as follows

$$h(t, \tau) = \sum_{\ell=0}^{L-1} A_{\ell} \delta(\tau - (\tau_{\ell} - b_{\ell}t)). \quad (3.2)$$

$$h_b(t, \tau) = \sum_{\ell=0}^{L-1} h_{\ell} e^{j2\pi f_c \gamma t} \delta(\tau - (\tau_{\ell} - b_{\ell}t)) \quad (3.3)$$

Equations (3.8), (3.9), (3.11), and (3.12) that represent the received passband signal followed by resampling operation, passband-to-baseband conversion, and Doppler compensation procedure, are respectively rewritten as follows,

$$\begin{aligned} \tilde{y}(t) &= \tilde{s}(t) \otimes h(t, \tau) + \tilde{v}(t) \\ &= \sqrt{2} \Re e \left\{ \left( \sum_{\ell=0}^{L-1} h_{\ell} e^{j2\pi f_c \gamma t} s((1 + b_{\ell})t - \tau_{\ell}) \right) e^{j2\pi f_c t} \right\} \\ &\quad + \tilde{v}(t), \end{aligned} \quad (3.8)$$

$$\begin{aligned} \tilde{y}_{RS}(t) &= \Re e \left\{ e^{j2\pi f_c t} e^{j2\pi f_c b_{\ell} t} \sum_{\ell=0}^{L-1} h_{\ell} s((1 + b_{\ell})t - \tau_{\ell}) \right\} \\ &\quad + \tilde{v}_{RS}(t), \end{aligned} \quad (3.9)$$

$$y_{RS}(t) = e^{j2\pi \nu t} \sum_{\ell=0}^{L-1} h_{\ell} s((1 + b_{\ell})t - \tau_{\ell}) + v_{RS}(t), \quad (3.11)$$

$$\begin{aligned} z_{RS}[n] &= \sum_{\ell=0}^{L-1} h_{\ell} \frac{1}{\sqrt{N}} \sum_{q=-\frac{K}{2}}^{\frac{K}{2}-1} d[q] \exp\left(\frac{j2\pi q}{N} ((1 + b_{\ell})n - \tau_{\ell})\right) \\ &\quad + v_{RS}[n], \end{aligned} \quad (3.12)$$

The formulas of  $H[k, q]$  and  $F_{k,q}(b)$  in (3.15) and (3.16) can be respectively given by

$$H[k, q] = \sum_{\ell=0}^{L-1} h_{\ell} \exp\left(-j \frac{2\pi q \tilde{\tau}_{\ell}}{N} F_{k,q}(b_{\ell})\right), \quad (3.15)$$

$$F_{k,q}(b_\ell) = \frac{\sin(\Theta_{k,q})}{N \sin(\Theta_{k,q}/N)} \exp\left(-j \frac{N-1}{N} \Theta_{k,q}\right), \quad (3.16)$$

where  $\Theta_{k,q} = \pi(q(1 + b_\ell) - k)$ .

Using the aforementioned equations in the sparse UWA channel generation and BELLHOP-MATLAB wrapper, OMP-MAP algorithm is then performed, where the simulation-related curves are provided in the next subsection.

### 3.7.2 Simulation Results for UWA Channel undergoing Rician Fading with different non-uniform Doppler rates

The communication parameters of the OFDM system used in this section are the same in table 3.2. The underwater parameters such as, the residual Doppler shift values ( $b_{max}$ ), signalling type, the value of the resolution factor ( $\varrho$ ), and the value of the pilot spacing ( $\Delta_p$ ) used are all provided in the discussions of the figures and their captions.

Figs. 3.15 and 3.16 show the MSE and SER performance curves of the OMP and OMP-MAP algorithms, corresponding to the UWA channel whose CIR is given by Fig. 3.5 with different Doppler scaling factors. Considering different constellation models, OMP-MAP is presented in binary phase shift-keying (BPSK), quadrature phase shift-keying (QPSK) and 16-ary quadrature amplitude modulation (16QAM) signaling formats as a function of SNR. During simulations, the pilot spacing, Doppler spread and the oversampling (resolution) factor were chosen as  $\Delta_p = 4$ ,  $b_{max} = 10^{-4}$  and  $\varrho = 4$ , respectively. As seen

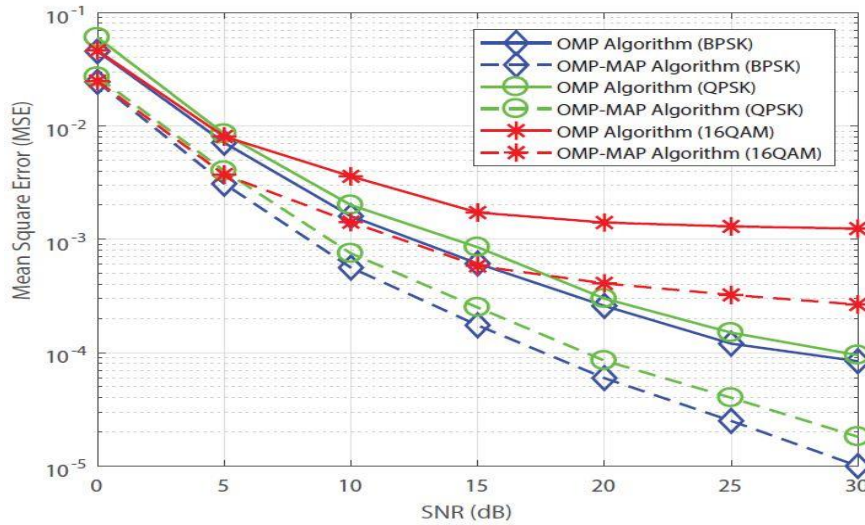


Figure 3.15 MSE vs. SNR performance comparisons of the OMP-MAP and OMP algorithms for different constellations:  $\varrho = 4$ ,  $b_{max} = 10^{-4}$ ,  $\Delta_p = 4$ .

from Figs. 3.15 and 3.16, the OMP-MAP algorithm, having excellent channel estimation and symbol error rate performance, uniformly outperforms the OMP estimator. For instance, within the 25-30 dB SNR region, the MSE and SER performances of the OMP-MAP algorithm are about 8-10 dB and 3-5 dB better than those of the OMP algorithm, respectively, depending on the modulation scheme employed. This is mainly due to the fact that the OMP-MAP algorithm makes use of the prior information of the Rician distributed channel gains very effectively.

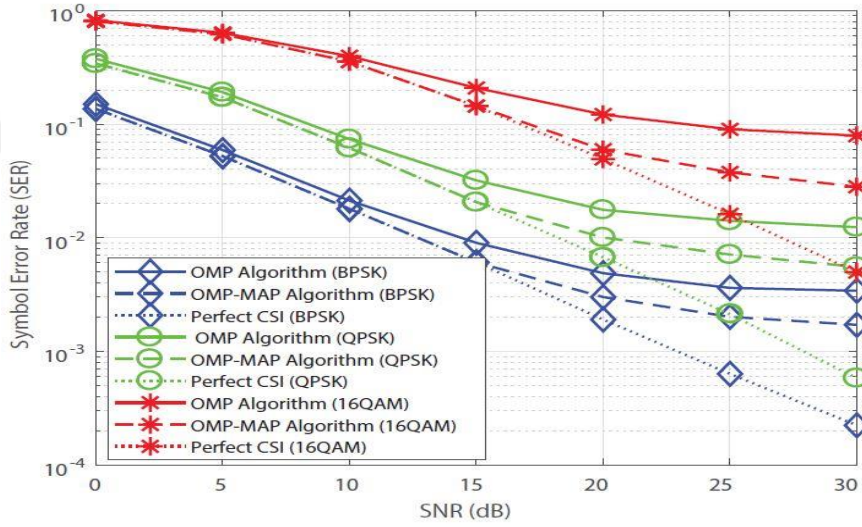


Figure 3.16 SER vs. SNR performance comparisons of the OMP-MAP and OMP algorithms for different constellations:  $\varrho = 4, b_{max} = 10^{-4}, \Delta_p = 4$ .

In Figs. 3.17 and 3.18, the MSE and SER performances of the OMP-MAP and OMP algorithms are shown as functions of SNR for different values of the oversampling factors,  $\varrho = [2, 4, 8]$ , in the presence of maximum Doppler shift of  $b_{max} = 10^{-4}$ , pilot spacing  $\Delta_p = 4$  and 16QAM signaling. It can be seen from these figures that an oversampling factor of  $\varrho = 4$  would be sufficient to obtain the best sparse channel estimation performance of the proposed OMP-MAP algorithm. In case of higher order oversampling factor, the enhancement in the average MSE and the SER would be negligible with a higher computation complexity.



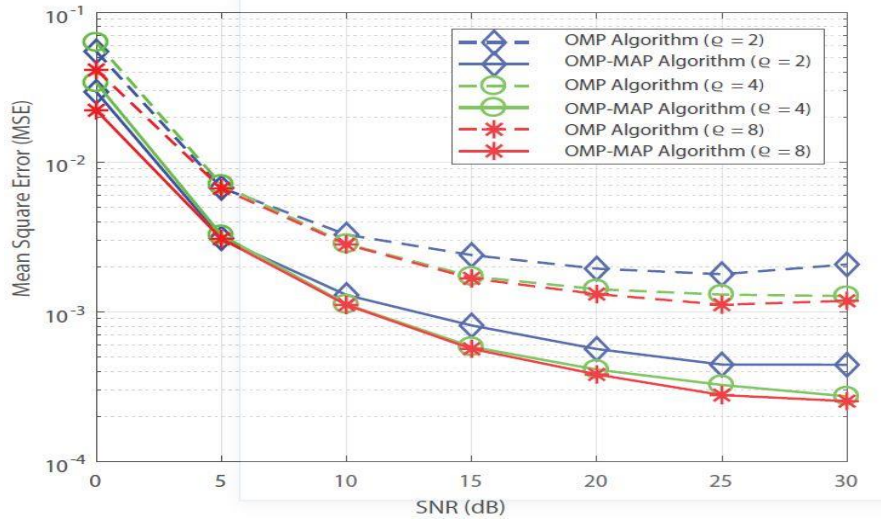


Figure 3.17 MSE vs. SNR performances of the OMP-MAP and OMP algorithms for different resolution factors:  $b_{max} = 10^{-3}$ ,  $\Delta_p = 4$ , 16QAM signaling.

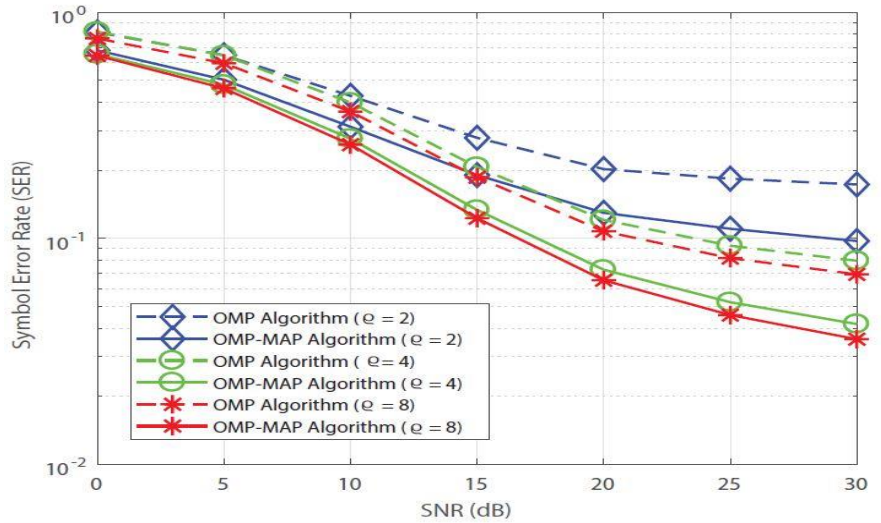


Figure 3.18 SER vs. SNR performances of the OMP-MAP and OMP algorithms for different resolution factors:  $b_{max} = 10^{-3}$ ,  $\Delta_p = 4$ , 16QAM signaling.

Moreover, Figs. 3.19 and 3.20 investigate the effect of the Doppler spread on the MSE and SER performances of the system with oversampling factor  $\rho = 4$ , pilot spacing  $\Delta_p = 4$  and 16QAM signaling. Figs. 3.19 and 3.20 show the average MSE vs. Doppler rate and SER vs. Doppler rate. It can be observed from these plots that the proposed OMP-MAP algorithm is quite robust to Doppler shifts up to  $b_{max} = 5 \times 10^{-3}$ , beyond of which can

be considered as severe Doppler effect, and that it has uniformly better performance than the OMP algorithm for  $b_{max}$  values varying between  $10^{-5}$ –  $10^{-3}$ .

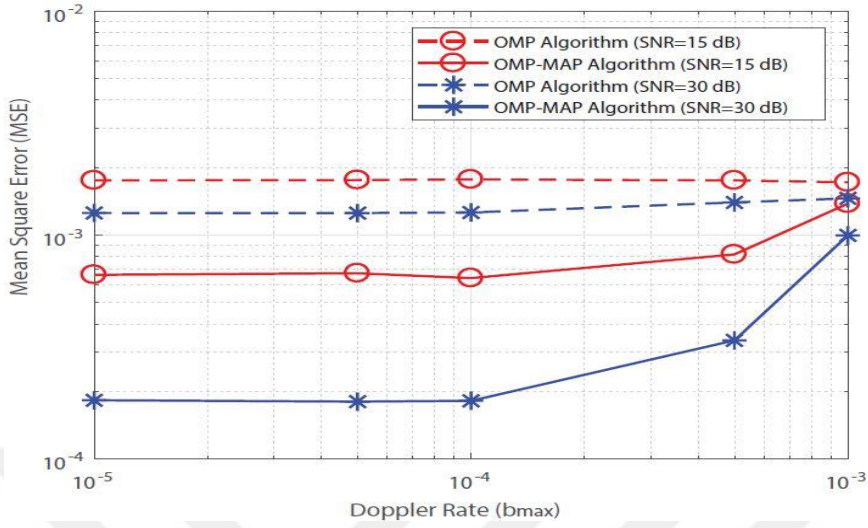


Figure 3.19 MSE vs. Doppler rate performances of the OMP-MAP and OMP algorithms for different Doppler rates:  $\varrho = 8, \Delta_p = 4$ , 16QAM signaling.

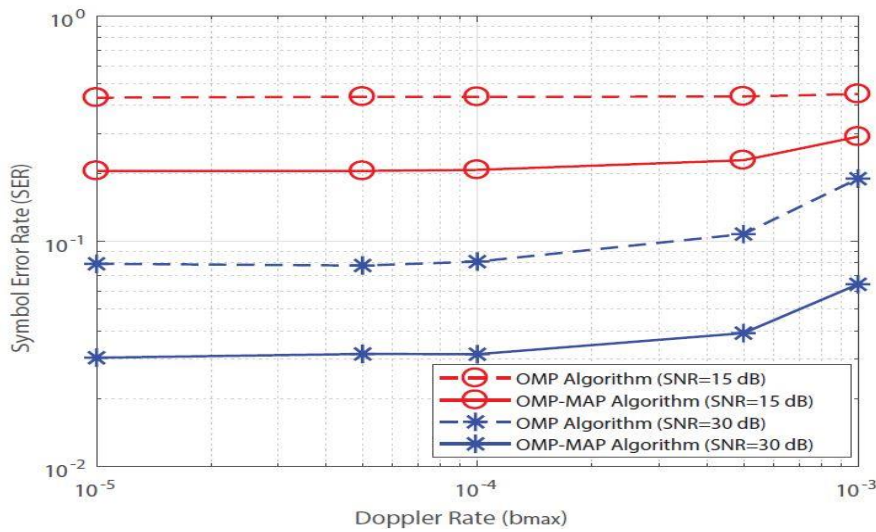


Figure 3.20 SER vs. Doppler rate performances of the OMP-MAP and OMP algorithms for different Doppler rates:  $\varrho = 8, \Delta_p = 4$ , 16QAM signaling.

In Fig. 21, the effects of different pilot spacings ( $\Delta_p = 2, 4, 8$ ) on the SER performance as a functions of SNR is investigated. The parameters are chosen as  $\varrho = 4$  and  $b_{max} = 10^{-4}$  with 16QAM signaling. It can be seen from these curves that the channel estimation algorithm can tolerate a pilot spacing of  $\Delta_p = 4$  sufficiently to handle Doppler spreads

around  $b_{max} = 10^{-4}$ . The SER performance degrades rapidly as the pilot spacing increases beyond that.

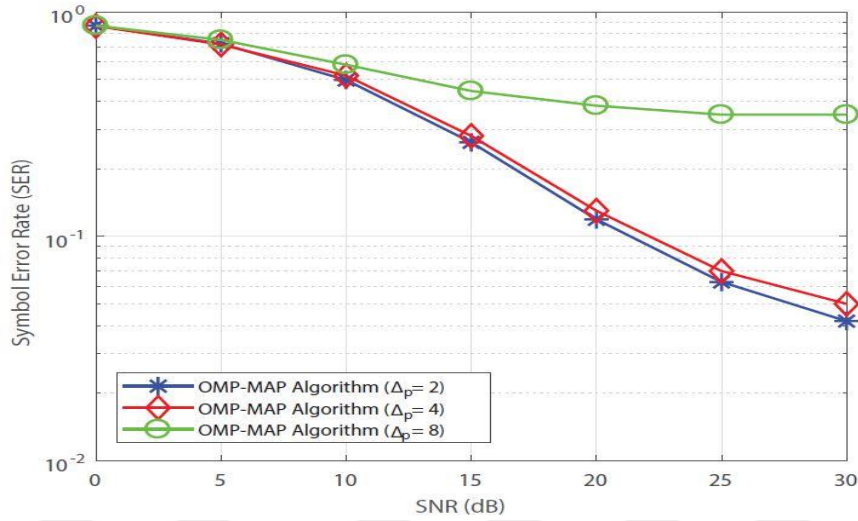


Figure 3.21 SER vs. SNR performance of the OMP-MAP algorithm for different pilot spacings:  $\rho = 4$ ,  $b_{max} = 10^{-4}$ , 16QAM signaling.

Finally, in Figs. 3.22 and 3.23, MSE & SER vs. SNR performance results are presented when residual Doppler scales  $b_\ell$  and paths delays  $\kappa_\ell$  are drawn from random distributions such as uniform  $U([-b_{max}, +b_{max}])$  and Poisson distribution respectively, for every trial run. The purpose here is to show that the results hold for a wide range of  $\tau_\ell$  and  $b_\ell$  and are not influenced by certain specific choices of  $\tau_\ell$  or  $b_\ell$  as in the present simulation set up. In the same figures, the performance results include the fast iterative shrinkage-thresholding algorithm (FISTA) that can be found in (Yuta et al., 2015), a fast version of the ISTA algorithm and a part of the basis pursuit (BP) family, and compare them with the proposed OMP-MAP algorithm. Note that, to operate the FISTA algorithm efficiently, the regularization parameter, the initial values for the channel coefficients, a parameter called learning rate as well as a suitable threshold value, to compute the shrinkage function, should be chosen very carefully. These parameters affect the convergence rate of the iterative algorithm, substantially. The figures below (Fig. 3.22 and Fig3.23) show the computer simulation results of MSE-vs-SNR and SER-vs-SNR curves corresponding to the OMP-MAP and FISTA algorithms. It can be shown in these plots that the OMP-MAP algorithm also outperforms the FISTA, although the gap between the proposed OMP-MAP and FISTA is narrower than that of the OMP algorithm, but at the expense of more involved and higher computational complexity to operate the FISTA algorithm.

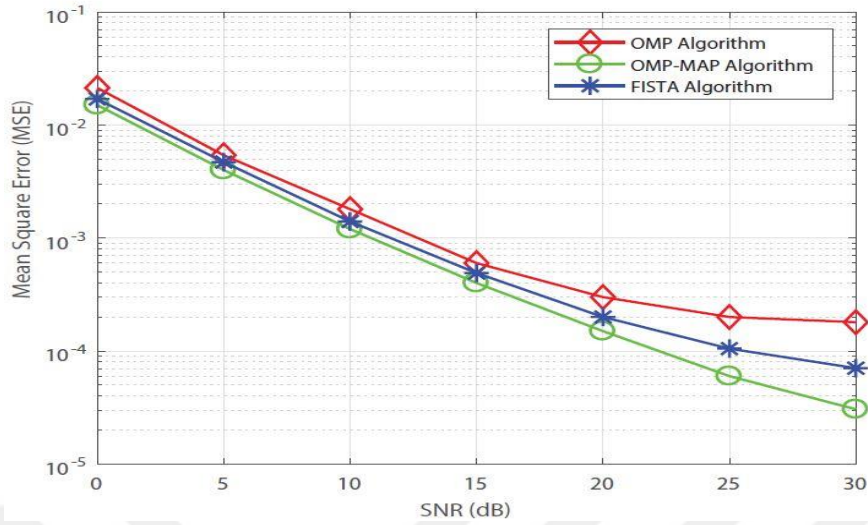


Figure 3.22 MSE vs. SNR performances of the OMP-MAP, OMP and FISTA algorithms with QPSK signaling,  $\rho = 4$ ,  $b_{max} = 10^{-4}$ ,  $\Delta_p = 4$ .

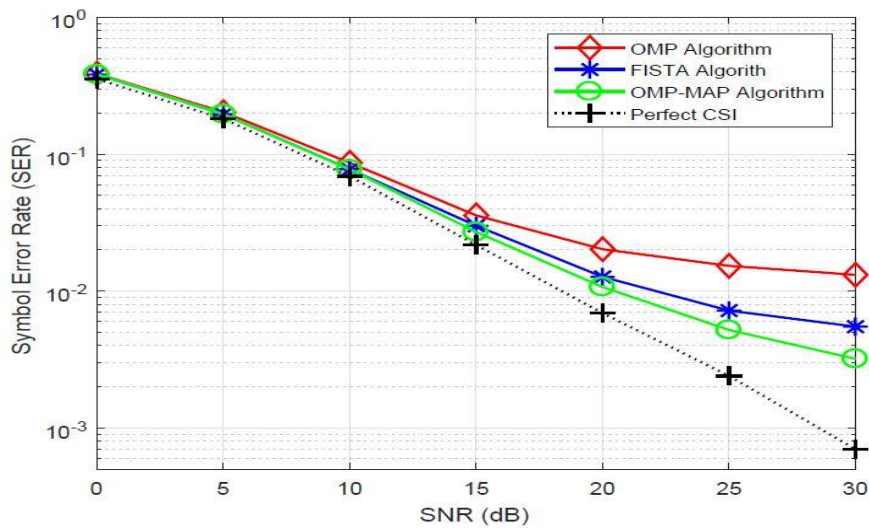


Figure 3.23 SER vs. SNR performances of the OMP-MAP, OMP and FISTA algorithms with QPSK signaling,  $\rho = 4$ ,  $b_{max} = 10^{-4}$ ,  $\Delta_p = 4$ .

### 3.7.3 Simulation Results for UWA Channel undergoing *log-normal and Nakagami-m* Fading with different non-uniform Doppler rates

In this subsection, an investigation on the MSE and SER performances of the proposed channel estimation algorithm by computer simulations in the presence of different fading

models such as log-Normal and Nakagami- $m$ , while retaining the same receiver side algorithm that is constructed based on a Rician/Rayleigh model.

The channel path coefficients of the Rician/Rayleigh fading are complex-valued Gaussian random variables with independent real and imaginary parts having mean and variance,  $\mu_\ell$  and  $\sigma_\ell^2$  for each path  $\ell = 0, 1, \dots, L - 1$ . That is, discarding the channel path indices  $\ell$  for notational simplicity,  $h_{Rician} = \Omega = 2\mu_\ell^2 + 2\sigma_\ell^2, E = \{|h_{Rician}|^2\} = \varkappa = 8\sigma_\ell^4 + 16\sigma_\ell^2\mu_\ell^2 + 4\mu_\ell^4$ .

Similarly, for log-normal fading the complex-valued fading coefficients are generated from  $h = \exp(X_R + jX_I)$ , where  $X_R$  and  $X_I$  are independent Gaussian random variables with mean  $M$  and variance  $S^2$ . Its second and fourth moments are given as

$$E = \{|h_{log-normal}|^2\} = \exp\left(M + \frac{S^2}{2}\right),$$

$$E = \{|h_{log-normal}|^4\} = \exp(2M + S^2).$$

Finally for Nakagami- $m$  fading, the complex-valued fading coefficients are generated from  $h = \sqrt{G} \exp(j\phi)$  where  $G$  is a Gamma distributed random variable with parameters  $m$  and  $\omega$  where  $m$  is the shape parameter and  $\omega$  is the spreading factor. Its second and fourth moments are given as

$$E = \{|h_{Nakagami}|^2\} = \frac{\Gamma(m+1)\omega}{\Gamma(m)m},$$

$$E = \{|h_{Nakagami}|^4\} = \frac{\Gamma(m+2)}{\Gamma(m)} \left(\frac{\omega}{m}\right)^2.$$

In the following computer simulations, for mismatch analysis, the parameters  $(M, S^2)$  and  $(m, \omega)$  of the log-normal and Nakagami probability density functions (pdfs), respectively, are determined in terms of the Rician parameters namely, the mean  $\mu$  and variance  $\sigma^2$  for each channel path. These parameters have been obtained to yield equivalent second and fourth moments of the underlying channel coefficients as suggested in (Radošević, Proakis, & Stojanović, Statistical characterization and capacity of shallow water acoustic channels, 2009), that is

$$E = \{|h_{Rician}|^2\} = E \{|h_{log-normal}|^2\} = E = \{|h_{Nakagami}|^2\} = \Omega,$$

$$E = \{|h_{Rician}|^4\} = E \{|h_{log-normal}|^4\} = E = \{|h_{Nakagami}|^4\} = \varkappa.$$

This normalization ensures that the mean value of the log-normal random variable is in the range of mean values of Rician and Nakagami fading channels. By solving the related equations above, it can be shown that these parameters can be obtained for the log-normal distribution as

$$M = \ln(\Omega) - \left(\frac{1}{4}\right) \ln(\kappa)$$

$$S^2 = \left(\frac{1}{4}\right) \ln(\kappa) - \left(\frac{1}{2}\right) \ln(\Omega)$$

and for the Nakagami- $m$  distribution as

$$m = \left(\frac{\Omega^2}{\kappa - \Omega^2}\right),$$

$$\omega = \Omega.$$

Consequently, as will be seen from the computer simulations shortly, if a different fading model other than Rician/Rayleigh, such as log-normal or Nakagami- $m$ , is simulated while retaining the same receiver side algorithm that is constructed based on the Rician fading, the MSE and SER performance is degraded mainly by two types of mismatch situations.

1) The real and imaginary parts of the fading coefficients of the log-normal and Nakagami random variables are no longer Gaussian. Hence, the Gaussian assumption on the prior distribution employed in the proposed algorithm is violated.

2) The mean and the variance of the log-normal and Nakagami distributions cannot be made equal to that of the Rician distribution because of the normalization process that is applied to those distributions, as described earlier, to make the second and fourth order moments equal to each other.

Figs. 3.24 and 3.25 present computer simulation results for the MSE and SER performances in such mismatched situation in the presence of log-normal and Nakagami fading when the Rician fading is the correct model. In these simulations, the residual Doppler is drawn uniformly from  $([-b_{max}, +b_{max}])$  and path delays are generated from a Poisson process within  $[0, L_{CP}]$ .

As can be seen from the MSE-SNR and SER-SNR curves shown in Figs. 3.24 and 3.25, the log-normal fading model was affected most when it is running over the channel

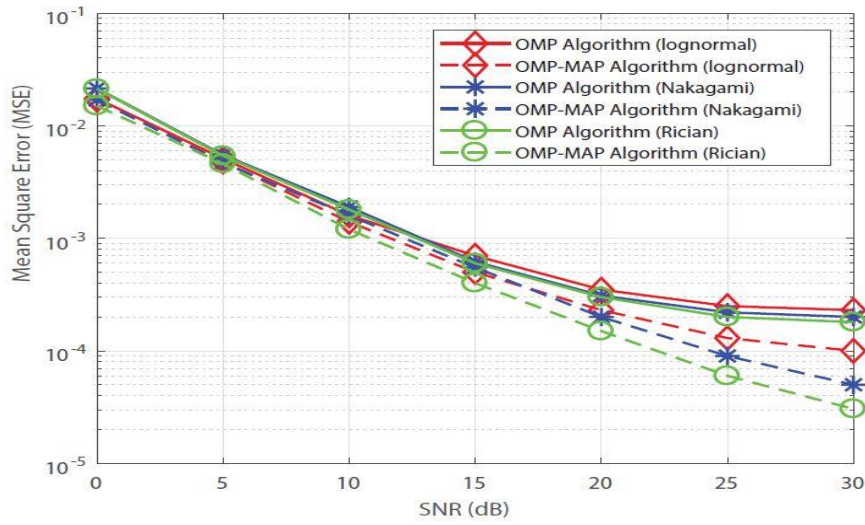


Figure 3.24 MSE vs. SNR comparisons of the OMP-MAP and OMP algorithms for different fading models with QPSK signaling,  $\rho = 4$ ,  $b_{max} = 10^{-4}$ ,  $\Delta_p = 4$  (random case channel).

estimation algorithm. Other than the non-Gaussian mismatch between the Rician and log-normal, it can be observed that there are substantial discrepancies between the mean and variance parameters of these two fading models. On the other hand, the Nakagami fading

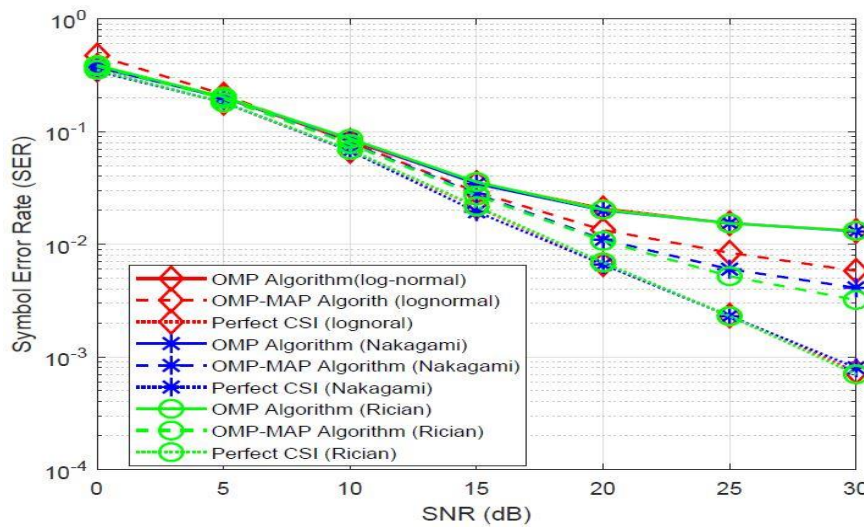


Figure 3.25 SER vs. SNR comparisons of the OMP-MAP and OMP algorithms for different fading models with QPSK signaling,  $\rho = 4$ ,  $b_{max} = 10^{-4}$ ,  $\Delta_p = 4$  (random case channel).

model seems to be less sensitive to the model mismatches, as can be seen also from the same plots. This would be due to the reasons that its mean and variance parameters are

fairly close to that of the Rician distribution and the pdf of the Nakagami distribution is more Gaussian in the vicinity of the mean value. From these curves it can be observed that the performances of Nakagami- $m$  and lognormal fading models employing the OMP algorithm are almost same as the one achieved by the Rician fading model.

### **3.7.4 Conclusion**

In this chapter, two low-complexity novel pilot assisted channel estimation and equalization algorithms for OFDM-based UWA systems are presented with uniform and non-uniform Doppler scaling. The proposed algorithms estimate the unknown parameters of the UWA channel such as sparse complex-valued channel gains and the channel delays are estimated by the MP-MAP and OMP-MAP algorithms, respectively. On the other hand, the means and variances of the prior distributions of the channel gains are obtained by ML estimation. The performance of the proposed algorithms has been assessed by detailed computer simulations on synthetic data based on real underwater channel environmental characteristics. These computer simulations show that the UWA channel is estimated very effectively and the proposed algorithms have excellent symbol error rate and channel estimation performance, and is robust to the effects of Doppler mismatch. In addition, the second approach is compared to FISTA algorithm (as a candidate of BP algorithms) with different random channel cases, where the second proposed approach showed a better estimation. Thus, the proposed approach and the resulting channel estimation algorithms are very promising for this kind of challenging and severe channel estimation scenarios.



## 4. SPARSE CHANNEL ESTIMATION FOR SPACE-TIME BLOCK CODED OFDM-BASED UNDERWATER ACOUSTIC CHANNELS

In this chapter, a Maximum a *posteriori* probability-Expectation Maximization-based channel estimation algorithm for OFDM-based underwater acoustic systems undergoing Rayleigh fading for a  $2 \times 1$  transmission diversity is derived and presented.

### 4.1 Introduction

Communication over acoustic signals, underwater results in multi-scale multi-lag channels due to multipath propagation. Hence, a robust channel estimation technique has to be present at the receiver. In this chapter, assuming underwater channels undergoing Rayleigh fading, a path-based channel model that characterizes each path of the time-varying sparse channel by a delay, a Doppler scale, and an attenuation factor is considered. Alamouti's space-time block transmit diversity scheme is used in the form of two-transmit antennas and one-receiver, hence, the proposed OFDM-based non-data-aided algorithm iteratively estimates the complex channel parameters of each subcarrier using the expectation maximization (EM) method, which in turn converges to a true maximum a posteriori probability (MAP) estimate of the unknown channel, where Karhunen-Loeve expansion is performed for complexity reduction. Finally, the novel channel estimation algorithm combines the aforementioned MAP-EM technique with ESPRIT algorithm to accommodate the delay estimation by reflecting the sparseness of the underwater acoustic channels. The performance of the proposed algorithm is then presented in terms of average mean square error (MSE) and symbol error rate (SER) for QPSK signalling with extreme Doppler spreads and different pilot spacings. The computer simulations presented show that excellent MSE & SER vs SNR performance is achieved even in the present of extreme Doppler shifts.

Channel estimation methods considering different diversity techniques have been introduced with orthogonal frequency division multiplexing (OFDM) for frequency selectivity compensation in different land-based telecommunication systems (Cirpan et al., 2006), and have attracted significant attention in underwater acoustic communications (UWACs) due to their robustness against large multipath spreads. Different studies have considered the least-mean-squares (LMS) algorithm in multiple input-multiple-output (MIMO) UWAC channel estimator design (Xi et al., 2017) (Yang and Zheng, 2014). In (Xi et al., 2017), the authors have combined turbo equalizers with fast self-optimized LMS, where the resulting channel estimator is found to yield a low bit error rate performance for a  $2 \times 4$  MIMO communication model. The proposed approach in (Yang and Zheng, 2014) iteratively estimates the channel using an improved version of the normalized-LMS with maximum a posteriori probability (MAP) with two transmitters and six receivers. (Biagi, 2014) and (Beaujean and Bernault, 2003) have adopted a single-input-multiple output (SIMO) type of diversity. The channel estimator in (Biagi, 2014) introduces pulse position modulation for power efficiency and positioning, while a Rake receiver is considered for diversity. The authors of (Beaujean and Bernault, 2003) have developed a design for  $1 \times 4$  MIMO considering long range communications in shallow water. On the other hand, channel estimation and equalization for amplify-and-forward cooperative relay based OFDM systems in UWAC channels was investigated in (Panayirci et al., 2016), assuming a Rayleigh fading channel model between source, relay and destination, an efficient algorithm is developed based on the space-alternating generalized expectation-maximization (SAGE) technique. Furthermore, numerous channel estimation techniques have been developed based on Alamouti's coding schemes (Alamouti, 1998). For instance, (Li et al., 2010) proposed a space-time coding OFDM-based algorithm for a  $2 \times 12$  UWA MIMO communication system. In (Eghbali et al., 2014), a differential space-frequency block coded (SFBC)-based MIMO OFDM UWAC system was presented with a channel estimator and a differential maximal ratio combiner for data symbol detection for a single-input single-output communication model, and by deploying two transmitters with various numbers of receivers. (Gwon et al., 2013) considered synthetic data for channel generation using the BELLHOP Acoustics Toolbox (Porter, last accessed, 2018). Assuming different diversity models, the approach utilizes

L1-norm minimization to detect channel taps with high power, and then estimates the channel using LMS.

In this chapter, assuming a sparse underwater channel undergoing Rayleigh fading with transmitter diversity in the form of multiple-input-single-output (MISO) with Alamouti's coding. Using the data in the pilot symbols of the OFDM system and the information carrying symbols on the optimization of the channel estimation, the proposed non-data-aided based algorithm iteratively estimates the channel according to the MAP criterion using the Expectation-Maximization (EM) algorithm. In addition, Karhunen-Loeve expansion and ESPRIT algorithms are presented for a lower computational load on the channel estimator, and delay estimation of the sparse channel, respectively.

The remainder of this chapter is organized as follows. Section 4.2 provides the Alamouti's transmit diversity scheme proposed for an OFDM system. In Section 4.3, the sparse-time-varying underwater channel model is presented. Section 4.4 presents the proposed EM-based MAP channel estimator. Section 4.5 includes synthetic data generation description for simulation of the underwater channel, and the computer simulation results are presented to assess the performance of the proposed approach. Finally, section 4.6 contains concluding remarks.

## 4.2 Alamouti's Transmit Diversity Scheme For OFDM Systems

In this section, a generalized Alamouti's (Alamouti, 1998) space-time block coded transmit diversity scheme for an OFDM-based UWAC system is used. Thus, second order diversity can be achieved assuming two-transmit antennas and one-receiver. During the  $n^{th}$  OFDM block (symbol) interval  $(nT, (n+1)T)$ , the data symbols  $d_k(n), k = 0, 1, \dots, N-1$ , modulated by the  $k^{th}$  subcarrier are simultaneously transmitted from the two antennas indexed by  $\mu = 1, 2$ . They are assumed to have unit variance and be independent for different  $k$ 's and  $n$ 's. For every  $k$ th subcarrier, the proposed Alamouti's encoding scheme maps every two consecutive symbols  $d_k(2n)$ , and  $d_k(2n+1)$ , to the following  $(2 \times 2)$  matrix:

$$\begin{array}{c} \text{time} \rightarrow \\ \text{space} \downarrow \end{array} \left[ \begin{array}{cc} d(2n, k) & d(2n+1, k) \\ -d^*(2n+1, k) & d^*(2n, k) \end{array} \right], \quad (4.1)$$

where (\*) stands for the complex conjugate operation. The rows of the matrix shown in (4.1) are transmitted with successive time intervals with the first and second symbol simultaneously through the first and second antenna, respectively. Defining  $\mathbf{D}(2n)$  and  $\mathbf{D}(2n+1)$  as an  $N \times N$  diagonal matrices with  $\mathbf{D}(2n)[k, k] = d_k(2n)$  and  $\mathbf{D}(2n+1)[k, k] = d_k(2n+1)$ . The received signal can be expressed in vectoral form as

$$\mathbf{Y}(2n) = \mathbf{D}(2n)\mathbf{H}_1(2n) + \mathbf{D}(2n+1)\mathbf{H}_1(2n+1) + \mathbf{V}(2n), \quad (4.2)$$

$$\begin{aligned} \mathbf{Y}(2n+1) = & -\mathbf{D}^\dagger(2n)\mathbf{H}_1(2n+1) + \mathbf{D}^\dagger(2n+1)\mathbf{H}_2(2n+1) \\ & + \mathbf{V}(2n+1), \end{aligned} \quad (4.3)$$

where  $\mathbf{H}_\mu(n) = [H_\mu(n, 0), H_\mu(n, 1), \dots, H_\mu(n, N-1)]^T$  denotes the channel transfer function for the  $N$  subcarriers between the  $\mu^{\text{th}}$  transmitter and the receiver,  $\mathbf{V}(2n)$  and  $\mathbf{V}(2n+1)$  are  $N \times 1$  vectors of zero-mean Gaussian additive noise samples, and  $(\dagger)$  denotes the conjugate transpose. However, the complex channel gains between adjacent OFDM blocks are assumed to be approximately equal, then the received signal,  $\mathbf{Y} = [\mathbf{Y}^T(2n), \mathbf{Y}^T(2n+1)]^T$ , can be expressed

$$\mathbf{Y} = \mathbf{D}\mathbf{H} + \mathbf{V}, \quad (4.4)$$

where  $\mathbf{H}_\mu(n) = [\mathbf{H}_{\mu,0}(n), \mathbf{H}_{\mu,1}(n), \dots, \mathbf{H}_{\mu,N-1}(n)]^T$  denotes the channel transfer function for the  $N$  subcarriers between the  $\mu^{\text{th}}$  transmitter and the receiver,  $[\mathbf{H}_1^T(2n), \mathbf{H}_2^T(2n)]^T$ ,  $\mathbf{V} = [\mathbf{V}_1^T(2n), \mathbf{V}_2^T(2n)]^T$ , and

$$\mathbf{D} = \begin{bmatrix} \mathbf{D}(2n) & \mathbf{D}(2n+1) \\ -\mathbf{D}^\dagger(2n+1) & \mathbf{D}^\dagger(2n) \end{bmatrix}$$

### 4.3 Representation of The Discrete UWA Channel

The time-varying UWA channel impulse responses (CIRs) from the  $\mu^{\text{th}}$  transmit antenna to the receiver are sparse and, in the  $n^{\text{th}}$  OFDM block (interval  $\in (nT, (n+1)T)$ ), it is characterized by

$$h_\mu(n, t) = \sum_{\ell=0}^{L-1} A_\ell^\mu(n) \delta(t - \tau_\ell^\mu(n)), \quad (4.5)$$

where  $L$ ,  $A_\ell^\mu(n)$  and  $\tau_\ell^\mu(n)$  denote the number of nonzero paths, the real channel path amplitudes and the time-varying path delays, respectively. The path gains are assumed to be constant over a duration of one OFDM symbol. That is  $A_\ell^\mu(2n) \approx A_\ell^\mu(2n+1)$ . The

path delays,  $\tau_\ell^\mu(n)$ , are caused by the motion of the transmitter/receiver pair as well as the scattering of the moving sea surface or reflection due to sound speed variations (Berger et al., 2010). For the duration of an OFDM symbol, the time variations of the path delays can be approximated well by a Doppler rate as,  $\tau_\ell^\mu(n) = \tau_\ell^\mu - \gamma_\ell^\mu n$  where  $\gamma_\ell^\mu$  is the Doppler scaling factor. In addition, it is assumed that all paths have a similar Doppler scaling factor  $\gamma_\ell^\mu(n) \approx \gamma_\ell$ , where  $\gamma^\mu = v^\mu/c$ ,  $v^\mu$  being the velocity of the  $\mu^{th}$  transmitter and  $c$  is the speed of the acoustic signal ( $\sim 1500$  m/s). Note that, in general the Doppler scaling factor can be different for each path (Mason et al., 2008). However, it was stated in (Hu et al., 2015) that, as long as the dominant Doppler shift is directly caused by the transmitter/receiver pair motion, this assumption can be justified. Moreover, in order to mitigate the frequency-dependent channel Doppler shifts due to fast-varying UWAs, first the received passband signal is resampled with a resampling factor  $\hat{\gamma}^\mu$  that corresponds to a rough Doppler estimate. Then, a fine Doppler shift compensation is applied on the received baseband signal. Assuming that the Doppler shift is estimated and compensated perfectly at the receiver and that all paths have similar Doppler scales, it has been shown that the discrete channel matrix of the UWA channels between the  $\mu^{th}$  transmitter and the receive antennas are close to diagonal (Hu et al., 2015). Taking these assumptions and approximations into account, the frequency response of the time-varying multipath UWA channel can be obtained from (5) as

$$\mathbf{H}_\mu(n, k) = \sum_{\ell=0}^{L-1} h_\mu(n, \ell) e^{\left(\frac{-j2\pi\tilde{\tau}_\ell^\mu(n)}{N}\right)}, \quad (4.6)$$

where  $N = T/T_s$ , and  $\tilde{\tau}_\ell^\mu(n) = \tau_\ell^\mu/T_s$  is the  $\ell^{th}$  normalized path delay.  $h_\mu(n)$  represents fading coefficients defined as  $h_\mu(n, \ell) = A_\ell^\mu(n) \exp\left(\frac{-j2\pi\tilde{\tau}_\ell^\mu(n)}{N}\right)$ .

In real underwater environment, diffuse multipath components are diffracted or scattered by the rough sea and bottom surface. The multipath components  $A_{\ell,i}^\mu$  and  $\tilde{\tau}_{\ell,i}^\mu$  are treated as random to describe the random movements of the scattering points in the underwater acoustic field (Qarabaqi and Stojanovic, 2013). Assuming the components in the summation above are independent and identically distributed, by the central limit theorem, that the channel coefficients  $h_\ell^\mu(n)$  in (6) are assumed to be complex Gaussian random variables with power delay profile  $P(\tau_\ell^\mu)$ , where  $\tilde{\tau}_\ell^\mu = \tilde{\tau}_{\ell,i}^\mu(n)$  for every OFDM block index  $n$ . It has been experimentally verified that an exponential decay is a valid

model for the power delay profile  $P(\tau_\ell^\mu) = C \exp\left(\frac{-\tau_\ell^\mu}{\tau_{rms}}\right)$  of UWA channels (Jensrud and Ivansson, 2015) and delays,  $\{\tau_\ell^\mu\}$ , are independent and uniformly distributed over the length of the cyclic prefix.  $C$  is a normalizing constant, chosen to satisfy  $C \sum_{\ell=0}^{L-1} e^{\left(\frac{-\tau_\ell^\mu}{L}\right)} = 1$ .

Depending on the sea conditions, each channel gain  $|h_\ell^\mu(n)|^2$  can be assumed to have a different distribution. With increasing the distance between the transmitter and the receiver, large sea dynamics prevent direct path contributions and mostly the diffuse multipaths dominate, resulting in channel gains having Rayleigh distribution. In this work, it is assumed *a priori* that the channel path gains obey a Rayleigh distribution. Normalized to unity, the discrete channel autocorrelation coefficients in frequency-domain for different OFDM blocks,  $n$ , defined as  $r_f(m) = \{H^\mu(n, k) H^{\mu\dagger}(n, k + m)\}$  can be found as (Hu et al., 2015)

$$r_f(m) = \frac{1 - e^{-L\left(\frac{1}{\tau_{rms}} + \frac{j2\pi m}{N}\right)}}{\tau_{rms} \left(1 - e^{\frac{-L}{\tau_{rms}}}\right) \left(\frac{1}{\tau_{rms}} + \frac{j2\pi m}{N}\right)}, \quad (4.7)$$

where  $m = 0, 1, \dots, N - 1$ .

#### 4.4 EM-Based Map Sparse Channel Estimation

In this section, a novel non-data-aided channel estimation algorithm is presented by representing the discrete multipath sparse channel based on the Karhunen-Loeve orthogonal representation and make use of the maximum a posterior Expectation Maximization technique (MAP-EM). Only few pilot symbols are used for initialization of the EM algorithm. By using the singular value decomposition (SVD),  $N \times N$  frequency-domain channel autocorrelation matrix,  $\mathbf{R}_f = [k, k + m] = r_f(m)$ , can be expressed as  $\mathbf{R}_f = \mathbf{U}\mathbf{\Lambda}\mathbf{U}^\dagger$ , where  $\mathbf{\Lambda}$  is a  $N \times N$  diagonal matrix with elements  $\lambda_0 > \lambda_1 > \dots > \lambda_{N-1}$  representing the eigenvalues and  $\mathbf{U} = [u_0, u_1, \dots, u_{N-1}]$ , where  $u_\ell \in \mathcal{C}^{N \times 1}$  are the corresponding eigenvectors of  $\mathbf{R}_f$ .

Rotating the channel vector,  $\mathbf{H}_\mu = |H_{k,\mu}(n)|$  in (4.6) representing the channel transfer function, by the linear transformation  $\mathbf{H}_\mu = \mathbf{U}\mathbf{G}_\mu$ . All components of  $\mathbf{G}_\mu \in \mathcal{C}^{N \times 1}$  become

independent, zero-mean Gaussian random variables  $\{\lambda_n\}_{n=0}^{N-1}$ . Hence, define  $\tilde{\Lambda} = \text{diag}(\Lambda, \Lambda)$ , then the prior pdf of  $\mathbf{G} = [\mathbf{G}_1^T, \mathbf{G}_2^T]^T$  can be expressed as

$$p(\mathbf{G}) \sim e^{-\mathbf{G}^\dagger \tilde{\Lambda}^{-1} \mathbf{G}}, \quad (4.8)$$

Given the transmitted data symbols,  $\mathbf{D}$ , coded according to Alamouti's scheme and the discrete channel representation  $\mathbf{G}$  and taking into account the independence of the noise components, the conditional probability density function of the received signal  $\mathbf{Y}$  can be expressed as,

$$p(\mathbf{Y}|\mathbf{D}, \mathbf{G}) \sim e^{-\frac{1}{\sigma^2} (\mathbf{Y} - \mathbf{D}\tilde{\mathbf{U}}\mathbf{G})^\dagger (\mathbf{Y} - \mathbf{D}\tilde{\mathbf{U}}\mathbf{G})}, \quad (4.9)$$

where  $\tilde{\mathbf{U}} = \text{diag}(\mathbf{U}, \mathbf{U}) \in \mathbb{C}^{2N \times 2N}$ .

In non-data-aided MAP channel estimation approach,  $\hat{\mathbf{G}}_{MAP}$  is chosen to maximize the posterior probability density function as,

$$\hat{\mathbf{G}}_{MAP} = \arg \max_{\mathbf{G}} p(\mathbf{G}|\mathbf{Y}), \quad (4.10)$$

A direct solution of this equation is mathematically intractable. Consequently, employing an iterative EM algorithm can simplify the problem, where the algorithm will inductively re-estimate the  $\mathbf{G}$ , so that a monotonic increase in the *a posteriori* conditional pdf in (10) is guaranteed. The monotonic increase is realized via the maximization of the auxiliary function

$$Q(\mathbf{G}|\mathbf{G}^{(q)}) = \sum_{\mathbf{D}} p(\mathbf{Y}, \mathbf{D}, \mathbf{G}) \log p(\mathbf{Y}, \mathbf{D}, \mathbf{G}^{(q)}), \quad (4.11)$$

where the summation is taken over all possible transmitted data coded signals and  $\mathbf{G}^{(q)}$  is the estimation of  $\mathbf{G}$  at the  $q^{th}$  iteration. Note that, the approximation  $p(\mathbf{Y}, \mathbf{D}, \mathbf{G}) \sim p(\mathbf{Y}, \mathbf{D}, \mathbf{G}^{(q)}) p(\mathbf{G})$  can be justified since the data symbols  $\mathbf{D} = \{\mathbf{D}^\mu(n, k)\}$  are assumed to be transmitted independently of each other and identically distributed and the fact that  $\mathbf{D}$  is independent of  $\mathbf{G}$ . Consequently,  $p(\mathbf{Y}, \mathbf{D}, \mathbf{G}^{(q)}) \sim p(\mathbf{Y}, \mathbf{D}, \mathbf{G}^{(q)}) p(\mathbf{G})$ .

Hence (4.11) can be evaluated by means of the expressions (4.8) and (4.9). Given the received signal,  $\mathbf{Y}$ , the EM algorithm starts with an initial value  $\mathbf{G}^{(0)}$  of the unknown channel parameters  $\mathbf{G}$ . The  $(q + 1)^{th}$  estimate of  $\mathbf{G}$  is obtained by the maximization step described by

$$\mathbf{G}^{(q+1)} = \arg \max_{\mathbf{G}} Q(\mathbf{G}|\mathbf{G}^{(q)}), \quad (4.12)$$

After a long algebraic manipulations, the expression of the re-estimate  $G_\mu^{(q+1)}$  ( $\mu = 1, 2$ ) can be obtained as follows:

$$G_1^{(q+1)} = (I + \sigma^2 \mathbf{\Lambda}^{-1})^{-1} \mathbf{U}^\dagger \left( \mathbf{\Gamma}_1^{\dagger(q)} \mathbf{Y}(2n) - \mathbf{\Gamma}_2^{\dagger(q)} \mathbf{Y}(2n+1) \right), \quad (4.13.1)$$

$$G_2^{(q+1)} = (I + \sigma^2 \mathbf{\Lambda}^{-1})^{-1} \mathbf{U}^\dagger \left( \mathbf{\Gamma}_2^{\dagger(q)} \mathbf{Y}(2n) + \mathbf{\Gamma}_1^{\dagger(q)} \mathbf{Y}(2n+1) \right), \quad (4.13.2)$$

where it can be easily seen that,  $(I + \sigma^2 \mathbf{\Lambda}^{-1})^{-1} = \text{diag}[(I + \sigma^2/\lambda_0)^{-1}, (I + \sigma^2/\lambda_1)^{-1}, \dots, (I + \sigma^2/\lambda_{N-1})^{-1}]$ , and  $\mathbf{\Gamma}_\mu^q$  in (13) is an  $N \times N$  dimensional diagonal matrix that represents the a *posteriori* probabilities of data symbols at the  $q^{\text{th}}$  iteration step whose  $k^{\text{th}}$  diagonal component is defined as

$$\begin{aligned} \Gamma_\mu^q(k, k) &= \sum_{a_1 \in \mathcal{A}_k} \sum_{a_2 \in \mathcal{A}_k} a_\mu p(d(2n, k) = a_1, d(2n+1, k) \\ &= a_2 | \mathbf{Y}, \mathbf{G}^{(q)}), \end{aligned} \quad (4.14)$$

and  $\mathcal{A}_k$  denotes the alphabet set taken by the  $k^{\text{th}}$  OFDM symbol. Note that, the optimal rank- $r$  estimator of  $\mathbf{G}_\mu$ , say  $\mathbf{G}_{\mu,r}$ , can be easily obtained by replacing  $\mathbf{\Lambda}_r = \text{diag} \{ \lambda_0, \lambda_1, \dots, \lambda_{r-1}, 0, 0, \dots, 0 \}$  with  $\mathbf{\Lambda}$  in (4.13). When the EM algorithm converges, the MAP estimate of  $\mathbf{H}_\mu$  can be determined as

$$\mathbf{H}_{\mu, \text{MAP}} = \mathbf{U} \mathbf{G}_{\mu, \text{MAP}}, \quad \text{for } \mu = 1, 2. \quad (4.15)$$

where,  $\mathbf{G}_{\mu, \text{MAP}}$  is the EM-converged value of  $\mathbf{G}_\mu^{(q)}$  in (4.13) after some number of iterations.

#### 4.4.1 initialization

The initial values for the unknown channel parameters are chosen to ensure a fast start up in the equalization/detection process following the channel estimation process.  $2P$  pilot symbols  $\{d(2n)\}$  and  $\{d(2n+1)\} \in \mathcal{A}_p$  are modulated by the  $i_p^{\text{th}}$  subcarrier transmitted at time slots  $\{(n, n+1)\}$  for  $p = 1, 2, \dots, P$ ,  $i_p \in \{0, 1, \dots, N-1\}$ , are used.

In order to interpolate the channel estimates, initially, there exist a minimum subcarrier spacing,  $\Delta_{sc}$ , between pilots given by  $\Delta_{sc} < 1/\tau_{max}$ , where  $\tau_{max}$  is the maximum delay spread of the channel in the frequency domain. For a constant envelope signal constellation, i.e., for phase shift keying (PSK) modulated alphabet set, the initial value of the channel parameters  $\mathbf{H}_\mu^{(0)}$ ,  $\mu = 1, 2$ , can then be determined as follows. The received



signal in (4.4), containing only the pilots in two successive OFDM blocks can be expressed as

$$\mathbf{Y}_p = \mathbf{D}_p \mathbf{H}_p + \mathbf{V}_p, \quad (4.16)$$

where  $\mathbf{Y}_p, \mathbf{H}_p, \mathbf{V}_p \in \mathcal{C}^{2P \times 1}$  and  $\mathbf{D}_p \in \mathcal{C}^{2P \times 2P}$  are obtained from  $\mathbf{Y}, \mathbf{H}, \mathbf{V} \in \mathcal{C}^{2N \times 1}$  and  $\mathbf{D} \in \mathcal{C}^{2N \times 2N}$  respectively by taking only the components at the pilot subcarriers  $i_p \in P = \{i_1, i_2, \dots, i_P\}$ . Hence, if the Alamouti assumption holds, the least squares (LS) estimation of the channel is obtained directly from (4.16) as

$$\tilde{\mathbf{H}}_{1,i_p}^{(0)}(2n) = \frac{1}{2} (\mathbf{D}_p^\dagger(2n) \mathbf{Y}_p(2n) - \mathbf{D}_p(2n+1) \mathbf{Y}_p(2n+1)) \in \mathcal{C}^{P \times 1}, \quad (4.17.1)$$

$$\tilde{\mathbf{H}}_{2,i_p}^{(0)}(2n) = \frac{1}{2} (\mathbf{D}_p^\dagger(2n+1) \mathbf{Y}_p(2n) + \mathbf{D}_p(2n) \mathbf{Y}_p(2n+1)) \in \mathcal{C}^{P \times 1}, \quad (4.17.2)$$

where  $\tilde{\mathbf{H}}_{i_p}^{(0)} \triangleq [\tilde{\mathbf{H}}_{1,i_p}^{(0)T}(2n), \tilde{\mathbf{H}}_{2,i_p}^{(0)T}(2n)]^T \in \mathcal{C}^{2P \times 1}$ .

Finally, from the  $P$  LS channel estimates,  $\tilde{\mathbf{H}}_{\mu,i_p}^{(0)}(2n), i_p \in P$ , the complete initial channel estimates in the frequency-domain,  $\tilde{\mathbf{H}}_{\mu,i_p}^{(0)}(2n), k = 0, 1, \dots, N-1$ , can be easily determined by using an interpolation technique, i.e., Lagrange interpolation algorithm. Initial values,  $\mathbf{G}_\mu^{(0)}$ , can then be determined by using the relation,  $\mathbf{G}_\mu^{(0)}(2n) = \mathbf{U}^\dagger \mathbf{H}_\mu(2n)$  for  $\mu = 1, 2$ .

Taking the pilot symbols into account, the soft data decisions  $\Gamma_\mu^{(q)}$  in (4.13) are updated with  $\check{\Gamma}_\mu^{(q)} = \text{diag} [\gamma_\mu^{(q)}(0), \gamma_\mu^{(q)}(1), \dots, \gamma_\mu^{(q)}(N-1)]$  and  $\check{\Gamma}_\mu^{(q)}(k)$ , is given as

$$\Gamma_\mu^{(q)}(k) = \begin{cases} d_k(2n) & \text{if } k \in \mathcal{P} \\ \check{\Gamma}_\mu^{(q)}(k, k) & \text{if } k \in \bar{\mathcal{P}} \end{cases}$$

Note that, the implementation complexity of the EM algorithm, presented above, can be reduced substantially due to the fact that the magnitude of the eigenvalues  $\lambda_k, k = 0, 1, \dots, N-1$  of the channel correlation matrix in (4.7) becomes negligible for  $k > 2BT + 1$ , where  $B$  is the one-sided bandwidth and  $T$  is the length of the channel impulse response. As pointed out in (Edfors et al., 1998), for an OFDM system  $2BT = L$ , where  $L$  is number of symbols in the cyclic prefix since  $T = LT_s$ , and  $2B = 1/T_s$ . Since  $L$  is much smaller than  $N$ , the total number of subcarriers, the complexity of the MAP estimation algorithm based on the Karhunen-Loeve expansion proposed in this work will be low while it is being optimal.

#### 4.4.2 Computation of $\Gamma_\mu^{(q)}$ for QPSK Signalling

Let  $a = (\pm 1 \pm j)$  represents an independent identically distributed data sequence using QPSK modulation technique. Since the data sequence  $a_\mu(k)$  is independent for  $\mu = 1, 2$  and  $k = 0, 1, \dots, N - 1$ , then  $\Gamma_m(k)$  in (4.14) can be computed as follows:

$$\Gamma_\mu^{(q)}(k) = \frac{\sum_{a_1 \in \mathcal{A}_k} \sum_{a_2 \in \mathcal{A}_k} a_\mu^* e^{\frac{2}{\sigma^2} \text{Re}[a_\mu^* Z^{\mu(q)}(n,k)]}}{\sum_{a_1 \in \mathcal{A}_k} \sum_{a_2 \in \mathcal{A}_k} e^{\frac{2}{\sigma^2} \text{Re}[a_\mu^* Z^{\mu(q)}(n,k)]}}, \quad (4.18)$$

where, for every pair of discrete time instances  $(2n, 2n+1)$  with  $y_k(1) \equiv y_k(2n)$  and  $y_k(2) \equiv y_k(2n+1)$ ,

$$Z_1^{(q)}(k) = \frac{1}{2} y_k(1) \sum_m G_1^{(q)*}(m) U_m^*(k) + y_k(2) \sum_m G_2^{(q)*}(m) U_m(k), \quad (4.19.1)$$

$$Z_2^{(q)}(k) = \frac{1}{2} y_k(1) \sum_m G_2^{(q)*}(m) U_m^*(k) - y_k^*(2) \sum_m G_1^{(q)*}(m) U_m(k), \quad (4.19.2)$$

By taking the summations then in the numerator and the denominator of (4.18) over the values of QPSK symbols  $a_1, a_2$ , for  $\mu = 1, 2$  and  $k = 0, 1, \dots, N - 1$ , the final result can be obtained as follows:

$$\Gamma_\mu^{(q)}(k) = \tanh\left[\frac{2}{\sigma^2} \text{Re}(Z^{\mu(q)}(k))\right] + j \tanh\left[\frac{2}{\sigma^2} \text{Im}(Z^{\mu(q)}(k))\right]. \quad (4.20)$$

#### 4.4.3 Final Sparse Channel Estimation

The estimates of the transfer function coefficients,  $\mathbf{H}_{\mu,MAP}$ , obtained above do not take into account the sparseness of the channel impulse response. In order to improve the channel estimation performance further, a sparse solution for the UWA channel impulse response  $\hat{\mathbf{h}}^\mu$  that best matches the model  $\mathbf{H}_{\mu,MAP} = \mathbf{F}_L \mathbf{h}^\mu$  is provided for the given  $\mathbf{H}_{\mu,MAP}$  and a desired degree of sparseness, where  $\mathbf{F}_L$  is an  $N \times L$  discrete Fourier transform (DFT) matrix.

In order to exploit the sparseness of the channel, a well known signal processing algorithm, called ESPRIT (Roy and Kailath, 1989) is adopted to estimate the channel path delays from the correlation matrix,  $\mathbf{R}_f$ . In general,  $\mathbf{R}_f$  is unknown to the receiver but can be estimated first through spatial smoothing and then through time-averaging over each consecutive time instants,  $n = 0, 1, \dots$  as

$$\bar{\mathbf{R}}_f = \hat{\mathbf{H}}_\mu(2n) \hat{\mathbf{H}}_\mu^\dagger(2n), \quad (4.21)$$

Once the channel gains,  $\hat{h}_\mu(\ell)$ , and the normalized delays,  $\hat{\tau}_\ell$ , of the sparse channel impulse response, are obtained, the transfer function coefficients of all subcarriers are estimated as

$$\hat{H}_{k,\mu}(n) = \sum_{\ell=0}^{L-1} \hat{a}_\mu(\ell) e^{\left(\frac{-j2\pi \hat{\tau}_\ell^\mu(n)}{N}\right)}, \quad (4.22)$$

ESPRIT algorithm is given in the following steps:

1. Perform an eigenvalue decomposition on  $\bar{\mathbf{R}}_f$  in (4.21)

$$\bar{\mathbf{R}}_f = \mathbf{U} \mathbf{\Sigma} \mathbf{U}^\dagger$$

where  $\mathbf{U} = [\mathbf{U}_s, \mathbf{U}_w]$  are the eigenvector matrices corresponding to the signal subspace and noise subspaces, and  $\mathbf{\Sigma}_s, \mathbf{\Sigma}_w$  in

$$\mathbf{\Sigma} = \begin{bmatrix} \mathbf{\Sigma}_s & 0 \\ 0 & \mathbf{\Sigma}_w \end{bmatrix}$$

are the eigenvalue matrices corresponding to the signal and noise subspaces, respectively.

2. Determine the  $L \times L$  matrix  $\Phi$  by solving the (usually overdetermined) system of equations

$$\mathbf{U}_2 = \mathbf{U}_1 \Phi,$$

where the  $(N-1) \times L$  matrices  $\mathbf{U}_2$  and  $\mathbf{U}_1$ , are constructed by the first  $N-1$  and last  $N-1$  rows of  $\mathbf{U}_s$ , respectively. The solution for  $\Phi$  can be obtained from  $\mathbf{U}_2$  as

$$\hat{\Phi} = (\mathbf{U}_1^\dagger \mathbf{U}_1)^{-1} (\mathbf{U}_1^\dagger \mathbf{U}_2)$$

3. Find an Eigen-decomposition of the matrix  $\hat{\Phi}$ . It can be shown that  $\hat{\lambda}_\ell = e^{-j2\pi \hat{\tau}_\ell / N}$ ,  $\ell = 0, 1, \dots, L-1$ , where  $\lambda_\ell$  is the  $\ell^{th}$  eigen value of  $\hat{\Phi}$ .
4. Determine the channel path delays as

$$\hat{\tau}_\ell = \frac{-N}{2\pi} \arg(\hat{\lambda}_\ell), \ell = 0, 1, \dots, L-1$$

The UWA channel transfer function coefficients are then used for data detection, as explained the following section.

## 4.5 Simulation Results

This section presents the computer simulation results of the proposed channel estimator assuming an OFDM-based UWAC system in the form of two-transmit antennas and one-receiver. In order to simulate an underwater channel, BELLHOP-MATLAB wrapper acoustic toolbox is considered (Porter, last accessed, 2018). The proposed underwater region is Sapanca Lake in Turkey, located at a latitude and longitude of 40.7163 and 30.2628, respectively. The lake has fresh water, the morphology of its bottom is near to flat, with a dimensions of approx. 16 km long, 5 km wide, and the deepest point of the lake is about 53 m. Considering a salinity of 0.5 ppt (parts per thousand), and 16 degrees as the averaged water temperature of Sapanca Lake (Akcaakan et al., 2014), the sound speed profile (SSP) is then obtained using Medwin formula (Bahrami et al., 2016). Finally, the SSP successfully entered into BELLHOP's environmental profile. The simulation parameters consider a range of communication of 5 km, and the base stations are placed at a depth of 20 m, and a flat bottom, where the UWA OFDM specifications can be found in table 3.2. However, BELLHOP outputs the channel impulse responses that contains both zero and nonzero paths. Consequently, a clustering process is performed over each two consecutive paths by summing up their powers if the difference of their corresponding delays is smaller than  $(1/B)$ , resulting into  $\mathcal{L}$  clusters. Then, a thresholding process is performed over the resulting clusters to project the sparsity of the underwater channel, and only paths with powers that satisfy  $(0.1 \sum_{e=0}^{\mathcal{L}-1} |h_e|)$  can successfully enter the simulation part.

The performance of the proposed algorithm is evaluated by means of the mean square error (MSE) and symbol error rate (SER) as a function of signal-to-noise-ratio (SNR). The data detection is performed using minimum mean-square error (MMSE) equalizer. given by

$$\tilde{\mathbf{D}}_D = \hat{\mathbf{H}}_{\mu,MAP}^\dagger (\hat{\mathbf{H}}_{\mu,MAP} \hat{\mathbf{H}}_{\mu,MAP}^\dagger + \gamma^{-1} \mathbf{I}_K)^{-1} \mathbf{Y}_D$$

where  $\gamma$  is the SNR and  $\mathbf{Y}_D$  is the received signal at the data subcarriers. Finally, using the estimated channel vector  $G_\mu^{(q+1)}$  in (4.13), (4.13) can be expressed in a vector form as

$$\hat{\mathbf{H}}_{\mu,MAP}^{(n)}(n) = \hat{\mathbf{Y}}_\mu h_\mu(n) + \mathbf{N}_\mu$$

where the noise term  $\mathbf{N}_\mu$  includes the additive Gaussian noise and the estimation errors and  $\hat{\mathbf{Y}}_\mu$  is a  $N \times L$  matrix whose  $(k, \ell)^{th}$  element for  $k = 0, 1, \dots, N - 1, \ell =$

$0, 1, \dots, L - 1$ , is  $\hat{\mathbf{Y}}_{\mu} [k, \ell] = e^{-j\frac{2\pi}{N}k\tilde{\tau}_{\ell}^{\mu}(n)}$ . Accordingly, the least-square estimation of  $\hat{\mathbf{H}}_{\mu,MAP}^{(n)}$  at discrete time instant  $n$  can be obtained as,

$$\hat{\mathbf{h}}_{LS}^{\mu}(n) = (\hat{\mathbf{Y}}_{\mu}^{\dagger} \hat{\mathbf{Y}}_{\mu})^{-1} \hat{\mathbf{Y}}_{\mu}^{\dagger} \hat{\mathbf{H}}_{\mu,MAP}^{(n)}$$

The performance of the channel estimator is compared with the Alamouti's approach (after performing a linear interpolation process over the channel obtained in (4.17) and by taking its inverse discrete Fourier transform (IDFT)), and with MAP-EM algorithm, which is similar to the proposed model, except that, it does not take into consideration the sparsity exploitation (the usage of ESPRIT algorithm), and thus, an IDFT operation is performed on the channel obtained in (4.13).

Assuming a Doppler shift compensation mechanism is applied at the input of the receiver, Figs. 4.1 and 4.2, respectively, show the average MSE and SER for different *residual* Doppler shift  $b$  values in the presence of a pilot spacing of order  $\Delta_{sc} = 4$ . It can be observed from these curves that the sparsity feature of the proposed channel estimator provides a robustness to Doppler shifts up to  $10^{-3}$  Hz, which is considered as a severe Doppler shift. In addition, the gap between the MAP-EM and the proposed approach seem to get narrower over the expense of higher signal-to-noise ratio, but in underwater acoustical communications, experiencing a higher SNR is not always valid. Finally, the

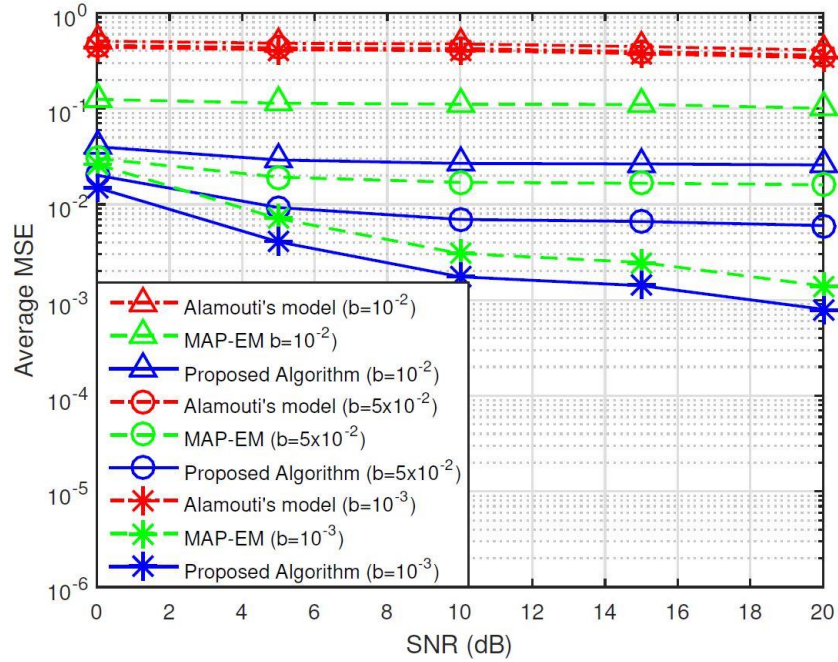


Figure 4.1 MSE vs. SNR performance of the MAP-EM-ESPRIT algorithm for different residual Doppler rates  $b = [10^{-3}, 5 \times 10^{-3}, 10^{-3}]$  with  $\Delta_{sc} = 4$ .

Alamouti's LS estimation presented in Fig. 4.1 does not seem to be promising, and its behavior towards different *residual* Doppler shifts is negligible. In Fig. 4.2, the SER curves of the proposed approach are promising. The gap between the MAP-EM and the proposed approach increases as the signal-to-noise ratio increases. In addition, in the presence of low SNR, the gap in the SER curves between the proposed approach and the perfect CSI case is very narrow, which is preferable in underwater acoustic communication, since achieving high SNR may not be applicable using such type of signals in such environment.

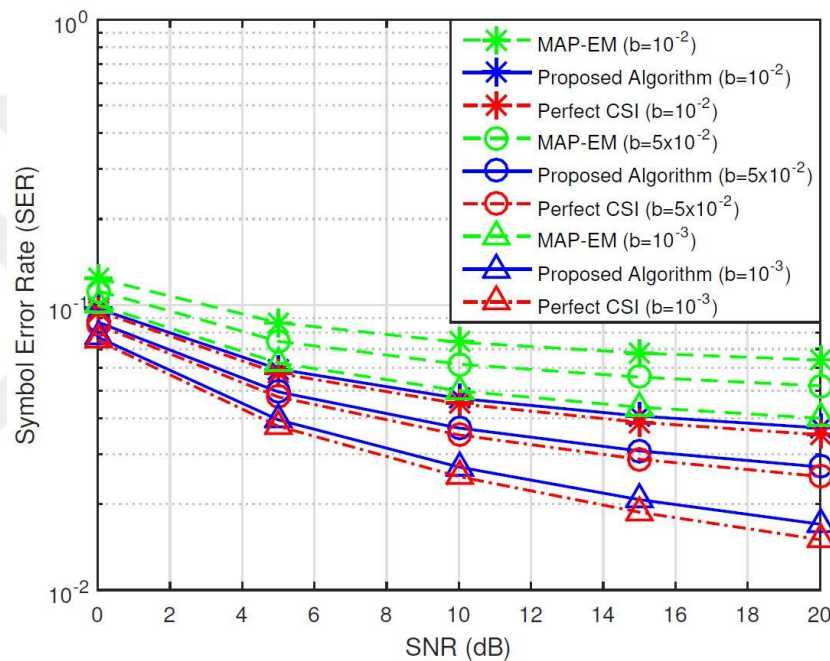


Figure 4.2 SER vs. SNR performance of the MAP-EM-ESPRIT algorithm for different residual Doppler rates  $b = [10^{-3}, 5 \times 10^{-3}, 10^{-2}]$  with  $\Delta_{sc} = 4$ .

Figs. 4.3 and 4.4, respectively, show the MSE and the SER performance of the proposed algorithm for the purpose of pilot design investigation. The parameters used consider different pilot spacings  $\Delta_{sc} = [2, 4, 8]$  in the presence of a *residual* Doppler shift of order  $10^{-3}$  Hz.

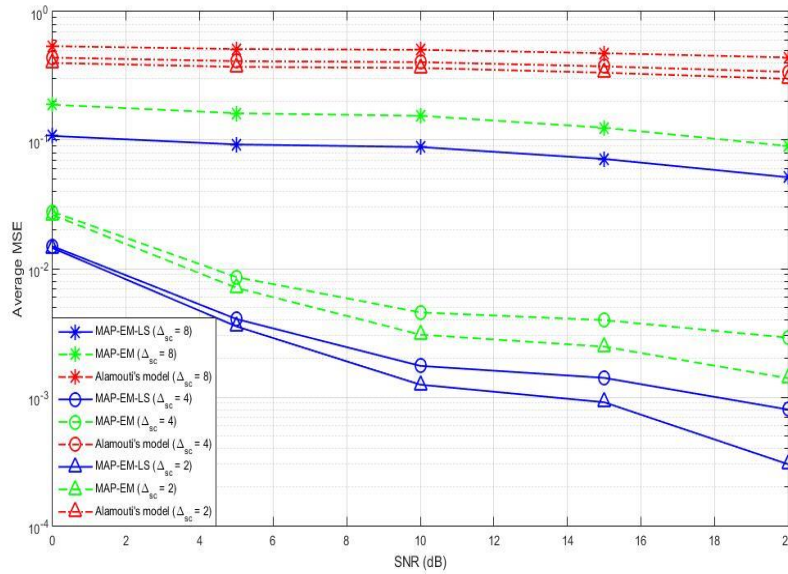


Figure 4.3 MSE vs. SNR performance of the MAP-EM-ESPRIT algorithm for different pilot spacings  $\Delta_{sc} = [2, 4, 8]$ , with  $b = 10^{-3}$  Hz.

Fig. 4.3 show the MSE performance for Alamouti's LS estimation, MAP-EM, and the proposed approach. As can be seen from the curves, the Alamouti's estimation is weak even when low pilot spacings is used. On the other hand, the curves of the proposed approach show a quite enhancement when compared with the MAP-EM. That is, the gap between the MAP-EM and the proposed approach is in the order of several dB, and shows a promising performance.

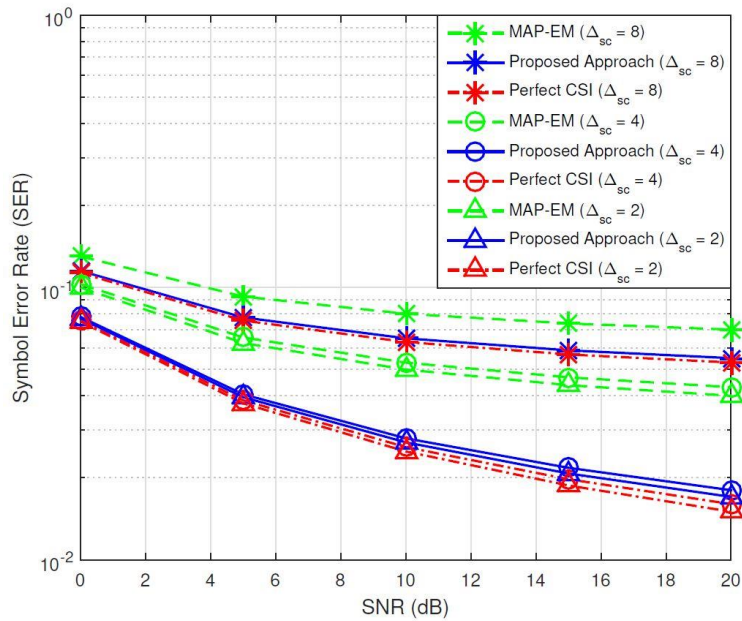


Figure 4.4 SER vs. SNR performance of the MAP-EM-ESPRIT algorithm for different pilot spacings  $\Delta_{sc} = [2, 4, 8]$ , with  $b = 10^{-3}$  Hz.

Finally, the SER presented in Fig. 4.4 show a large gap between the MAP-EM and the proposed approach. In addition, the proposed approach can sufficiently handle a pilot spacing of  $\Delta_{sc} = 4$ . The gap in the SER achieved in between  $\Delta_{sc} = 2$  and  $\Delta_{sc} = 4$  can be ignored for the purpose of spectrum saving. In addition, at low SNR values, the gap between the curves of the perfect CSI and the curves of the proposed approach is narrow for all pilot spacing values. These insightful curves show a promising SER performance in such SNR values, which are preferable since achieving high SNR is not always accomplishable

#### **4.6 Conclusion**

In this chapter, a channel estimation algorithm has been developed for OFDM-based UWAC that considers Alamouti's space-time block transmit diversity scheme with two-transmit antennas and one receiver. The non-data-aided proposed algorithm iteratively estimates the complex channel parameters of each subcarrier using the Expectation Maximization method, which in turn converges to a true maximum a *posteriori* probability estimate of the unknown channel. In addition, Karhunen-Loeve expansion has been applied to reduce the complexity of the channel estimator, while the ESPRIT algorithm has been used for the delay estimation of the taps with high powers to exploit the UWA channel sparsity. Considering QPSK signalling, the computer simulations presented show robustness in channel estimation in terms of mean square error and symbol error rate for extreme residual Doppler spreads and various pilot spacings.



## 5. CONCLUSIONS

In this work, three computational-friendly pilot-assisted OFDM-based channel estimation techniques for underwater acoustic communication systems were proposed. The first two approaches are designed for single-input single-output (SISO) communication system with channels that undergo Rician fading, where matching pursuit (MP) and orthogonal matching pursuit (OMP) algorithms for Doppler and delay estimation, respectively. Then maximum a *posteriori* probability is used to estimate the channel gains. Finally, these two approaches use maximum likelihood (ML) for the prior densities estimation. The system model of the MP-MAP algorithm considers a colored type of noise, where the channel paths experience the same Doppler factor, and hence there is no Doppler “spread” but just an uncompensated residual Doppler. While the OMP-MAP approach considers white noise with a non-uniform Doppler scales, and hence, each path has a different Doppler factor. The mean square error (MSE) and the symbol error rate (SER) performances of the MP-MAP and OMP-MAP shown in the computer simulations sections show robustness against high scale Doppler shifts in the presence of fair resolution factor of the dictionary matrix, and a promising performance for 16QAM signalling. In addition, the computer simulation results in the OMP-MAP section are compared to the fast iterative shrinkage-thresholding algorithm (FISTA) algorithm (as a candidate of the basis pursuit estimation), and with to two other channels that follow log-normal and Nakagami- $m$  fading in the presence of random channel case.

The third approach assumes multiple-input single-output (MISO) communication system that includes two-transmitters and one-receiver with channel that undergo Rayleigh fading with white noise and a uniform Doppler spread. The algorithm considers Alamouti’s coding for the diversity part. The proposed non-data-aided algorithm iteratively estimates the complex channel parameters of each subcarrier using the Expectation Maximization method, which in turn converges to a true maximum a

posteriori probability estimate of the unknown channel. Moreover, the Karhunen-Loeve expansion has been applied to this algorithm for complexity reduction of the channel estimator. Finally, ESPRIT algorithm was used for the delay estimation of the taps with high powers to exploit the underwater acoustic channel sparsity. The computer simulations presented show robustness in channel estimation in terms of MSE and SER for an extreme *residual* Doppler spread and various pilot spacing values (for underwater pilot design purposes). In addition, the channel sparseness presented by ESPRIT algorithm has shown the significance of the proposed approach with narrow gap in the SER between the proposed approach and the perfect channel state information curve, which lead to a better symbol error rate along the signal-to-noise values.

Different contributions can be made over the work presented in this thesis. Mainly, the OFDM-based channel estimation work presented can be mainly extended by means of:

1. Multiple-input multiple-output (MIMO) type of communication deployment, such that, the channel estimator can have a better experience of the fading channels.
2. Impulsive type of noise consideration, that can be generated by man-made instruments, snapping shrimp and other underwater acoustic phenomena.
3. Away from direct communication scenarios, a relay-assisted (cooperative) communication model, where a relay is placed between the transmitter and the receiver can increase the system's capacity, and a multi-hop relay-based system can overcome the fading channels, and power limitations.
4. Adaptive modulation techniques can also be deployed to improve the overall system's capacity.
5. The third proposed approach can be extended to different modulation techniques other than QPSK, for higher data rate.
6. An experimental type of channel is also essential to be applied in simulations to reflect a realistic behavior of the channel estimator.

## REFERENCES

- Adzhani, S. I., Mahmudah, h., & Santoso, T. B. (2016). Time-frequency analysis of underwater ambient noise of mangrove estuary. *2016 International Electronics Symposium (IES)*, (pp. 223-227). Denpasar.
- Ahmed, S. (2015). Estimation and compensation of Doppler scale in UAC OFDM systems. *OCEANS 2015 - MTS/IEEE Washington*, (pp. 1-12). Washington, DC.
- Akcaakan, R., Koker, L., Gurevin, C., & Albay, M. (2014). Planktothrix rubescens: a perennial presence and toxicity in Lake Sapanca. *Turk J Bot*, vol. 38, no. 4, 782-789.
- Alamouti, S. M. (1998). A simple transmit diversity technique for wireless communications. *IEEE J. Sel. Areas Commun.*, vol. 16, no. 8, 1451-1458.
- André, M., v der Schaar, M., Sánchez, A. M., Baudin, E., Folegot, T., Rousset, C., & Audoly, C. (2016). Underwater acoustic observatories to reduce ship noise footprint: A risk assessment model to mitigate the impact of shipping noise on marine fauna. *2016 Techno-Ocean (Techno-Ocean)*, (pp. 329-332).
- Bahrami, N., Khamis, N. H., & Baharom, A. B. (2016). Study of Underwater Channel Estimation Based on Different Node Placement in Shallow Water. *IEEE Sensors Journal*, vol. 16, no. 4, 1095-1102.
- Barbeau, M., Blouin, S., Cervera, G., Garcia-Alfaro, J., Hasannezhad, B., & Kranakis, E. (2015). Simulation of underwater communications with a colored noise approximation and mobility. *2015 IEEE 28th Canadian Conference on Electrical and Computer Engineering (CCECE)*, (pp. 1532-1537).
- Beaujean, P. J., & Bernault, E. P. (2003). A new multi-channel spatial diversity technique for long range acoustic communications in shallow water. *Oceans 2003. Celebrating the Past ... Teaming Toward the Future (IEEE Cat. No.03CH37492)*, (pp. 1533-1539). San Diego, CA, USA.
- Berger, C. R., Zhou, S., Preisig, J., & Willett, P. (2010). Sparse channel estimation for multicarrier underwater acoustic communication: From subspace methods to compressed sensing. *IEEE Trans. Signal Process.*, vol. 58, no. 3, 1708-1721.
- Bernard, E. N., & Meinig, C. (2011). History and future of deep-ocean tsunami measurements. *OCEANS'11 MTS/IEEE*, (pp. 1-7). KONA, Waikoloa, HI.
- Beygi, S., & Mitra, U. (2015). Multi-scale multi-lag channel estimation using low rank approximation for OFDM. *IEEE Trans. Signal Process.*, vol. 63, no. 18, 4744-4755.
- Biagi, M. (2014). Image-Processing-Based Transceiver Design for Acoustic PPM Underwater Links. *IEEE J. Ocean. Eng.*, vol. 39, no. 4, 592-606.
- Browning, D. G., Scheifele, P. M., & Mellen, R. H. (1988). Attenuation of low frequency sound in ocean surface ducts: implications for surface loss values. *OCEANS '88. A Partnership of Marine Interests. Proceedings*, (pp. 318-322). Baltimore, MD,.
- Chen, K., Ma, M., Cheng, E., Yuan, F., & Su, W. (2014). A survey on MAC protocols for underwater wireless sensor networks. *IEEE Commun. Surveys Tutor. Third Quarter*, vol. 16, no. 3, 1433-1447.
- Chen, P., Rong, Y., Nordholm, S., He, Z., & Duncan, A. J. (2017). Joint Channel Estimation and Impulsive Noise Mitigation in Underwater Acoustic OFDM

- Communication Systems. *IEEE Transactions on Wireless Communications*, vol. 16, no. 9, 6165-6178.
- Chitre, M. (2007). A high-frequency warm shallow water acoustic communications channel model and measurements. *J. Acoust. Soc. Amer.*, vol. 122, no. 5, 2580-2586.
- Chitre, M. A., Potter, J. R., & Ong, S. H. (2006). Optimal and Near-Optimal Signal Detection in Snapping Shrimp Dominated Ambient Noise. *IEEE J. Ocean. Eng.*, vol. 31, no. 2, 497-503.
- Choudhuri, C., & Mitra, U. (2009). Capacity bounds and power allocation for underwater acoustic relay channels with ISI. *ACM Int. Workshop on Underwater Networks*. Berkeley, CA, USA.
- Cirpan, H. A., Panayirci, E., & Dogan, H. (2006). Non-data-aided channel estimation for OFDM systems with space-frequency transmit diversity. *Trans. Veh. Technol.*, vol. 55, no. 2, 449-457.
- Cotter, S. F., & Rao, B. D. (2002). Sparse channel estimation via matching pursuit with application to equalization. *IEEE Trans. Commun.*, vol. 50, no. 3, 374-377.
- Edfors, O., Sandell, M., van de Beek, J. J., Wislon, S. K., & Borjesson, P. O. (1998). OFDM channel estimation by singular value decomposition. *IEEE Trans. Commun.*, vol. 46, no. 7, 931-939.
- Eghbali, H., Stojanovic, M., & Muhaidat, S. (2014). Differential decoding for SFBC OFDM systems in underwater MIMO channels. *IEEE International Conference on Acoustics, Speech and Signal Processing (ICASSP)*. Florence.
- Emre, Y., Kandasamy, V., Duman, T. M., Hursky, P., & Roy, S. (2008). Multi-input multi-output OFDM for shallow-water UWA communications. *Proc. Acoustics*, (pp. 13-17).
- Falahati, A., Woodward, B., & Bateman, S. C. (1991). Underwater acoustic channel models for 4800 b/s QPSK signals. *IEEE J. Ocean. Eng.*, vol. 16, no. 1, 12-20.
- Galvin, R., & Coats, R. E. (1996). A stochastic underwater acoustic channel model. *MTS/IEEE OCEANS Conf.*, (pp. 203-210).
- Guimarães, D. A., Chaves, L. S., & de Souza, R. A. (2014). Snapping shrimp noise reduction using convex optimization for underwater acoustic communication in warm shallow water. *2014 International Telecommunications Symposium (ITS)*, (pp. 1-5). Sao Paulo.
- Gwun, B. C., Han, J. W., Kim, K. M., & Jung, J. W. (2013). MIMO underwater communication with sparse channel estimation. *2013 Fifth International Conference on Ubiquitous and Future Networks (ICUFN)*, (pp. 32-36). Da Nang.
- Ha, D. V., Nguyen, V. D., & Nguyen, Q. K. (2017). Modeling of Doppler power spectrum for underwater acoustic channels. *Journal of Communications and Networks*, vol. 19, no. 3, 270-281.
- Hu, F., Wang, Y., & Jin, L. (2015). Robust MIMO-OFDM design for CM-MB systems based on LMMSE channel estimation. *2015 IEEE 5th International Conference on Electronics Information and Emergency Communication*, (pp. 59-62). Beijing.
- Huang, J., Zhou, S., Berger, C., & Willett, P. (2011). Progressive inter-carrier interference equalization for OFDM transmission over time-varying underwater acoustic channels. *IEEE J. Sel. Topics Signal Process.*, vol. 5, no. 8, 1524-1536.

- Iqbal, H. N., Shaheen, S., Qazi, H., & Iqbal, J. (2013). A deterministic simulation modeling & analysis for the improvement of signal-to-noise ratio (SNR) based on ambient noise sources in underwater acoustic communication channel. *10th International Bhurban Conference on Applied Sciences & Technology (IBCAST)*, (pp. 335-338). Islamabad.
- Jalil, A. M., & Ghayeb, A. (2014). Distributed channel coding for underwater acoustic cooperative networks. *IEEE Trans. Commun.*, vol. 62, no. 3, 848-856.
- Jenserud, T., & Ivansson, S. (2015). Measurements and modeling of effects of out-of-plane reverberation on the power delay profile for underwater acoustic channels. *IEEE J. Ocean. Eng.*, vol. 40, 807-821.
- Kuai, X., Sun, H., & Cheng, E. (2016). Impulsive noise mitigation in underwater acoustic OFDM systems. *IEEE Trans. Veh. Technol.*, vol. 65, no. 10, 8190-8202.
- Kumar, M. G., & Sarvaya, M. (2016). Review on enhanced data rate receiver design using efficient modulation techniques for underwater acoustic communication. *2016 International Conference on Advanced Communication Control and Computing Technologies*, (pp. 313-317).
- Leus, G., & Van Walree, P. A. (2008). Multiband OFDM for covert acoustic communications. *IEEE J. Sel. Areas Commun.*, vol. 26, no. 9, 1662-1673.
- Li, B., & Stojanovic, M. (2010). Alamouti space time coded OFDM for underwater acoustic channels. *OCEANS 2010 IEEE*, (pp. 1-3). Sydney.
- Li, B., Huang, J., Zhou, S., Ball, K., Stojanovic, M., Greitag, L., & Willett, P. (2009). MIMO-OFDM for high-rate underwater acoustic communications. *IEEE J. Ocean. Eng.*, vol. 34, no. 4, 634-644.
- Li, B., Zhou, S., Stojanovic, M., Feritag, L., & Willett, P. (2008). Multicarrier communication over underwater acoustic channels with non-uniform Doppler shifts. *IEEE J. Ocean. Eng.*, vol. 33, no. 2, 198-209.
- Li, W., & Preisig, J. C. (2007). Estimation of rapidly time-varying sparse channels. *IEEE J. Ocean. Eng.*, vol. 32, no. 4, 927-939.
- Liling, & Dupeng. (2017). Research on modeling and testing technique of underwater noise stimulated by airborne source. *International Conference on Signal Processing, Communications and Computing (ICSPCC)*, (pp. 1-5). Xiamen.
- Liu, L., Zhang, Y., Zhang, P., Zhou, L., Li, J., Jin, J., . . . Lv, Z. (2016). PN sequence based Doppler and channel estimation for underwater acoustic OFDM communication. *2016 IEEE International Conference on Signal Processing, Communications and Computing (ICSPCC)*, (pp. 1-6).
- Liu, L., Zhou, Z., & Cui, J. H. (2008). Prospects and problems of wireless communication for underwater sensor networks. *Wireless Commun. Mobile Comput.*, 977-994.
- Llor, J., & Malimbres, M. P. (2013). Statistical modeling of large-scale signal path loss in underwater acoustic networks. *Sensors (Basel)*, vol. 13, no. 2, 2279-2294.
- Ma, L., Zhou, S., Qiao, G., Liu, S., & Zhou, F. (2017). Superposition coding for downlink underwater acoustic OFDM. *IEEE J. Ocean. Eng.*, vol. 42, no. 1, 175-187.
- Mandalapa Bhoopathy, V., Haj Frej, B. M., Ebenezer Amalorpavaraj, S. R., & Shaik, I. (2016). Localization and mobility of underwater acoustic sensor nodes. *2016 Annual Connecticut Conference on Industrial Electronics, Technology & Automation (CT-IETA)*, (pp. 1-5). Bridgeport, CT, .

- Mason, S. F., Berger, C. R., Zhou, S., & Willett, P. (2008). Detection, Synchronization, and Doppler Scale Estimation with Multicarrier Waveforms in Underwater Acoustic Communication. *IEEE Journal on Selected Areas in Communications*, vol. 26, no. 9, 1638-1649.
- Nguyen, S. T., Vayirci, E., Yang, L., & Rong, C. (2009). A shadow zone aware routing protocol for acoustic underwater sensor networks. *IEEE Communications Letters*, vol. 13, no. 5, 366-368.
- Panayirci, E., Senol, H., Uysal, M., & Poor, H. V. (2016). Sparse Channel Estimation and Equalization for OFDM-Based Underwater Cooperative Systems With Amplify-and-Forward Relaying. *IEEE Transactions on Signal Processing*, vol. 64, no. 1, 214-228.
- Pelekanakis, K., & Baggeroer, A. B. (2011). Exploiting space-time-frequency diversity with MIMO-OFDM for underwater acoustic communications. *IEEE J. Ocean. Eng.*, vol. 36, no. 4, 502-511.
- Peng, B., Rossi, P. S., Dong, H., & Kananenn, K. (2015). Time-domain oversampled OFDM communication in doubly-selective underwater acoustic channels. *IEEE Commun. Lett.*, vol. 19, no. 6, 1081-1084.
- Pesavento, M., Gershman, A. B., & Haardt, M. (2000). Unitary root-MUSIC with a real-valued eigendecomposition: A theoretical and experimental performance study. *IEEE Trans. Signal Process.*, vol. 48, no. 5, 1306-1314.
- Porter, M. (last accessed, 2018). *Bellhop Gaussian beam/finite element beam code*. Retrieved from Acoustics Toolbox: <http://oalib.hlsresearch.com>
- Prince, Mehra, R., & Kumar, R. (2015). Improving the SNR of the underwater acoustic signal affected by wind driven ambient noise using RLS algorithm. *2015 International Conference on Soft Computing Techniques and Implementations (ICSCTI)*, (pp. 45-50). Faridabad.
- Qarabaqi, P., & Stojanovic, M. (2011). Modeling the large scale transmission loss in underwater acoustic channels. *49th Annu. Allerton Conf. Commun. Control Comput.*, (pp. 445-452).
- Qarabaqi, P., & Stojanovic, M. (2013). Statistical Characterization and Computationally Efficient Modeling of a Class of Underwater Acoustic Communication Channels. *IEEE J. Ocean. Eng.*, vol. 38, no. 4, 701-717.
- Qarabaqi, P., Stojanovic, M., & . (2009). Statistical modeling of a shallow water acoustic communication channel. *Underwater Acoust. Meas. Conf.*, (pp. 1341-1350). Nafplion, Greece.
- Qi, C., Wang, X., & Wu, L. (2011). Underwater acoustic channel estimation based on sparse recovery algorithms. *IET Signal Processing*, vol. 5, no. 8, 739-747.
- Qu, F., & Yang, L. (2008). Basis expansion model for underwater acoustic channels? *MTS/IEEE OCEANS Conf.* Quebec City, PQ, Canada, .
- Radosevic, A., Duman, T., Proakis, J., & Stojanovic, M. (2011). Selective decision directed channel estimation for UWA OFDM systems. *IEEE Allerton Conf. Commun. Control Comput.*, (pp. 647-653). Monticello, IL, USA.
- Radosevic, A., Proakis, J., & Stojanovic, M. (2009). Statistical characterization and capacity of shallow water acoustic channels. *IEEE OCEANS Eur. Conf.*
- Roy, R., & Kailath, T. (1989). ESPRIT-estimation of signal parameters via rotational invariance techniques. *IEEE Trans. Acoust., Speech, Signal Process.*, vol. 37, no. 7, 984-995.

- Rugini, L., Banelli, P., & Leus, G. (2005). Simple equalization of time-varying channels for OFDM. *IEEE Commun. Lett.*, vol. 9, no. 7, 619-621.
- Ruiz-Vega, F., Clemente, M. C., Otero, P., & Paris, J. F. (2012). Rician shadowed statistical characterization of shallow water acoustic channels. *Underwater Commun., Channel Model. Validation*. Sestri-Levante, Italy.
- Santoso, T. B., Widjiati, E., Wirawan, & Hendratoro, G. (2015). Ambient noise measurement and characterization of underwater acoustic channel in Surabaya bay. *2015 IEEE Asia Pacific Conference on Wireless and Mobile (APWiMob)*, (pp. 58-61). Bandung.
- Shi, X., & yang, Y. (2016). Adaptive sparse channel estimation based on RLS for underwater acoustic OFDM systems. *Sixth International Conference on Instrumentation and Measurement, Computer, Communication and Control*, (pp. 266-269).
- Socheleau, F., Passerieux, J., & Laut, C. (2009). Characterisation of timevarying underwater acoustic communication channel with application to channel capacity. *Underwater Acoust.Meas. Conf.* Nafplion, Greece.
- Stojanovic, M. (2008). OFDM for underwater acoustic communications: Adaptive. *2008 IEEE International Conference on Acoustics, Speech and Signal Processing*, (pp. 5288-5291). Las Vegas, NV,.
- Stojanovic, M. (2008). Underwater acoustic communications: Design considerations on the physical layer. *IEEE/IFIP Fifth Annual Conference on Wireless On demand Network Systems and Services (WONS 2008)*. Garmisch-Partenkirchen, Germany,.
- Stojanovic, M. (2009). MIMO OFDM over underwater acoustic channels. *2009 Conference Record of the Forty-Third Asilomar Conference on Signals, Systems and Computers*, (pp. 605-609). Pacific Grove, CA, USA.
- Telichko, A., Sorokin, B., & Kvashnin, G. (2015). UHF acoustic attenuation and quality parameter limits in the diamond based HBAR. *2015 Joint Conference of the IEEE International Frequency Control Symposium & the European Frequency and Time Forum*, (pp. 94-99). Denver, CO.
- Tomasi, B., Casari, P., Badia, L., & Zorzo, M. (2010). A study of incremental redundancy hybrid ARQ over Markov channel models derived from experimental data. *5th ACM Int. Workshop UnderWater Netw.* Woods Hole, MA, USA.
- Tu, K., Fertonani, D., Duman, T. M., Stojanovic, M., Proakis, J. G., & Hursky, P. (2011). Mitigation of intercarrier interference for OFDM for timevarying underwater acoustic channels. *IEEE J. Ocean. Eng.*, vol. 36, no. 2, 156-171.
- Vaccaro, R. J. (1998). The past, present, and the future of underwater acoustic signal processing. *IEEE Signal Processing Magazine*, vol. 15, no. 4, 21-51.
- Vajapeyam, M., Vedantam, S., Mitra, U., Preisig, J. C., & Stojanovic, M. (2008). Distributed space-time cooperative schemes for underwater acoustic communications. *IEEE J. Ocean. Eng.*, vol. 33, no. 4, 489-501.
- van Moll, C. A., Ainslie, M. A., & van Vossen, R. (2009). A Simple and Accurate Formula for the Absorption of Sound in Seawater. *IEEE J. Ocean. Eng.*, vol. 34, no. 4, 610-616.
- Van Trees, H. (2002). *Optimum Array Processing, Detection, Estimation, and Modulation Theory (Part IV)*, 1st ed. New York: Wiley.

- Wang, C., & Wang, Z. (2016). Signal Alignment for Secure Underwater Coordinated Multipoint Transmissions. *IEEE Transactions on Signal Processing*, vol. 64, no. 23, 6360-6374.
- Webster, R., Munasinghe, A., & Jamalipour, A. (2017). Narrow-beam optical communications in underwater wireless network with passive node mobility. *2017 IEEE International Conference on Communications (ICC)*, (pp. 1-6). Paris, France.
- Xi, J., Yan, S., Yu, L., & Tian, J. (2017). Soft direct-adaptation based bidirectional turbo equalization for MIMO underwater acoustic communications. *China Communications*, vol. 14, no. 7, 1-12.
- Yang, W. B., & Yang, T. C. (2006). High-frequency channel characterization for M-ary frequency-shift-keying underwater acoustic communications. *J. Acoust. Soc. Amer.*, vol. 120, no. 5, 2615-2626.
- Yang, Z., & Zheng, Y. R. (2014). Robust adaptive channel estimation in MIMO underwater acoustic communications. *OCEANS 2014*, (pp. 1-6). 2014.
- Yu, F., Li, D., Guo, Q., Wang, Z., & Xiang, W. (2015). Block-FFT based OMP for compressed channel estimation in underwater acoustic communications. *IEEE Commun. Lett.*, vol. 19, no. 1, 1937-1940.
- Yuan, Z., Yan, S., Qin, Y., & Xu, L. (2016). An experiment-based time-varying underwater acoustic communication channel model regarding bottom scattering. *2016 IEEE International Conference on Signal Processing, Communications and Computing (ICSPCC)*, (pp. 1-5). Hong Kong.
- Yuta, T., Kazuhiko, F., Yuyuan, C., & Hiroshi, S. (2015). Iterative Reception Employing Sparse Channel Estimation for OFDM Systems. *IEEE 82nd Vehicular Technology Conference (VTC2015-Fall)*, (pp. 1-5). Boston.
- Zhang, J., Cross, J., & Zheng, Y. R. (2010). Statistical channel modeling of wireless shallow water acoustic communications from experiment data. *Military Commun. Conf.*, (pp. 2412-2416).
- Zhang, L., Han, J., Huang, J., & Nramdt-Pearce, M. (2014). OFDM transmission over time-varying channel with self interference cancellation. *2014 IEEE International Conference on Signal Processing, Communications and Computing (ICSPCC)*, (pp. 743-746). Guilin, China, .
- Zhang, L., Han, J., Huang, J., & Nramdt-Pearce, M. (2014). OFDM transmission over time-varying channel with self interference cancellation. *2014 IEEE International Conference on Signal Processing, Communications and Computing (ICSPCC)*, (pp. 743-746). Guilin, China, .
- Zhou, S., & Wang, S. (2014). *Introduction, in OFDM for Underwater Acoustic Communications*. Chichester, UK: John Wiley & Sons, Ltd.



## CURRICULUM VITAE



### Personal Information

**Name Surname**

**Place and Date of Birth**

**Address**

**e-mail address**

**Awards**

**Publications**

*Journal papers*

*Conference papers*

Mhd Tahssin Altabbaa

Damascus, Syria, 14/08/1986.

Silahtarağa Mah, Hazan Sok, 13/1, Eyüpsultan, İstanbul.

[tahsin@ieee.org](mailto:tahsin@ieee.org)

outstanding achievement PhD scholarship

- E. Panayirci, **M. T. Altabbaa**, M. Uysal, V. Poor, "Sparse channel estimation for OFDM-based underwater acoustic systems in rician fading with a new OMP-MAP algorithm," *IEEE Trans. Signal Process.*, **accepted with Minor Revisions**
- **M. T. Altabbaa**, T. Arsan, E. Panayirci, "Subchannel admission and power control for uplink femtocell networks with imperfect channel estimation," *Wireless Personal Communication Journal.*, Awaiting AE decision.
- **M. T. Altabbaa**, E. Panayirci, "Channel estimation and equalization algorithm for OFDM-based underwater acoustic communications systems," *The Thirteenth International Conference on Wireless and Mobile Communications*, Nice, France, July, 2017. (one of the best conference papers).
- **M. T. Altabbaa**, A. S. Ogrenci, E. Panayirci, H. V. Poor, "Sparse Channel Estimation for Space-Time Block Coded OFDM-Based Underwater Acoustic Channels," **accepted** by IEEE Globecom 2018,.
- **M. T. Altabbaa**, T. Ayabakan, S. Ogrenci, "Fuzzy logic for decision extraction from product reviews," *International Conference on Energy, Communication, Data Analytics and Soft Computing (ICECDS)*, SKR Engineering College, Poonamallee, Tamil Nadu, India, Aug, 2017.
- **M. T. Altabbaa**, T. Arsan and E. Panayirci, "Power control and resource allocation in TDD-OFDM based femtocell networks with interference," *IEEE International Black Sea Conference on Communications and Networking (BlackSeaCom)*, Istanbul, Turkey, 2017, pp. 1-5.

## Education

Undergraduate Education : Arab International University, 2012  
Graduate Education, MSc : Kadir Has University. 2015  
Graduate Education, PhD : Kadir Has University. 2018  
Foreign Language Skills : Arabic (MT), English (99/120 TOEFL, 2015),  
Turkish (C2 certificate, 2012), German (ZD, 2009).

## Work Experience

Name of Employer and Dates of Employment:

Prof. Dr. Erdal Panayircı

Feb, 2014 – Dec, 2018.

Contact:

Telephone : +90 (212) 533 57 53 / 1404

E-mail Address : [eepanay@khas.edu.tr](mailto:eepanay@khas.edu.tr)

## Publications derived from the thesis:

### *Journal papers:*

- E. Panayircı, **M. T. Altabbaa**, M. Uysal ,V. Poor, “Sparse channel estimation for OFDM-based underwater acoustic systems in rician fading with a new OMP-MAP algorithm,” *IEEE Trans. Signal Process.*, **accepted with Mandatory Revisions**

### *Conference papers:*

- **M. T. Altabbaa**, E. Panayircı, “Channel estimation and equalization algorithm for OFDM-based underwater acoustic communications systems,” *The Thirteenth International Conference on Wireless and Mobile Communications*, Nice, France, July, 2017. (one of the best conference papers).
- **M. T. Altabbaa**, A. S. Ogrenci, E. Panayircı, H. V. Poor, “Sparse Channel Estimation for Space-Time Block Coded OFDM-Based Underwater Acoustic Channels,” **accepted** by IEEE Globecom 2018.